

**Lehrstuhl für Fluidmechanik und Prozessautomation
der Technischen Universität München**

**Visualization of Temperature and Velocity Fields During
Phase Change of Water under High Hydrostatic Pressure**

Özlem Özmutlu

Vollständiger Abdruck der von der Fakultät Wissenschaftszentrum Weihenstephan für Ernährung, Landnutzung und Umwelt der Technischen Universität München zur Erlangung des akademischen Grades eines

Doktor-Ingenieurs (Dr.-Ing.)

genehmigten Dissertation.

Vorsitzender: Univ.-Prof. Dr.-Ing. Horst Chr. Langowski

Prüfer der Dissertation:

1. Univ.-Prof. Dr.-Ing. habil. Antonio Delgado
2. Univ.-Prof. Dr.-Ing. habil. Günter H. Schnerr
3. Prof. Dr.-Ing. Christoph Hartmann,
The German University in Cairo / Ägypten
(schriftliche Beurteilung)

Die Dissertation wurde am 10.03.2005 bei der Technischen Universität München eingereicht und durch die Fakultät Wissenschaftszentrum Weihenstephan für Ernährung, Landnutzung und Umwelt am 17.05.2005 angenommen.

.....dedicated to Deniz, Christoph and Yahya

..... without whom I could not succeed

PUBLICATIONS

- Esterl, S., Özmutlu, Ö., Hartmann, C., Delgado, A. “A three dimensional numerical approach to investigate the substrate transport and conversion in an immobilized enzyme reactor” *Biotechnology and Bioengineering*, (83), 780-789 (2003).
- Hartmann, C., Özmutlu, Ö., Petermeier, P., Fried, J., Delgado, A. „Analysis of the Flow Field Induced by the Sessile Peritrich Ciliate *Opercularia asymmetrica*” *Journal of Biomechanics*, submitted (2004)

POSTERS AND PROCEEDINGS

- Özmutlu, Ö., Hartmann, C., Delgado, A. „Numerical Simulation of Fluid Flow and Enzyme Catalysed Substrate Conversion in a Packed-bed Enzyme Reactor”, *PAMM 3, Issue 1, Section 13*, 398-399 (December 2003)
- Özmutlu Ö., Hartmann, C., Delgado, A. “Visualization of Temperature and Velocity Fields during Phase Change of Water under High Hydrostatic Pressure” *GALA 2003-Laser Methods in Fluid Mechanics*, September 2003, Braunschweig, Germany

ORAL PRESENTATIONS

- Özmutlu Ö., Hartmann, C., Delgado, A. “Numerical Simulation of Fluid Flow and Enzyme Catalysed Substrate Conversion in a Packed-bed Enzyme Reactor” *GAMM 2003*, 24-28 March 2003 , Abano Terme, Padua, Italy.
- Özmutlu Ö., Hartmann, C., Delgado, A. “Numerical Simulation of Fluid Flow and Enzyme Catalysed Substrate Conversion in a Packed-bed Enzyme Reactor” *VDI-GVC – Fachausschüsse* 31 March- 2 April 2003, Berlin, Germany.
- Özmutlu Ö., Hartmann, C., Delgado, A. “Visualization of Temperature and Velocity Fields during Phase Change of Water under High Hydrostatic Pressure” *GVC-Fachausschusssitzung "Lebensmittelverfahrenstechnik"*, 22-24 March 2004, Baden-Baden, Germany.
- Özmutlu Ö., Hartmann, C., Baars A., Delgado A. “Momentum and Energy Transfer during Phase Change of Water under High Hydrostatic Pressure” *High Pressure Bioscience and Bioengineering , 3rd International Conference*, 27-30 September 2004, Rio de Janeiro, Brazil.

CONTENTS

KURZFASSUNG	VI
ABSTRACT	VII
LIST OF NOTATIONS	VIII
1 INTRODUCTION	1
1.1 High Pressure Processing Applications	1
1.2 High Pressure Phase Change	4
1.3 Applications of Phase Change Processes under High Pressure.....	8
1.3.1 HHP Freezing	8
1.3.2 HHP Thawing	11
1.4 HHP Visualization and Modelling	13
1.5 Objectives	17
2 MATERIALS AND METHODS	19
2.1 High Pressure Unit	19
2.2 Experimental Methods.....	21
2.2.1 Thermochromic Liquid Crystals.....	22
2.2.2 Temperature Field Analysis.....	23
2.2.3 Convective Fields Analysis by HP-DPIV	25
3 THEORETICAL CONSIDERATIONS	27
3.1 Basic Equations of High Pressure Processing	27
3.1.1 Conservation of Mass	27
3.1.2 Conservation of Momentum.....	27
3.1.3 Conservation of Energy	30
3.2 Adaptation of High Pressure Phase Change	31
3.3 Dimensional Analysis of the Process	32
3.3.1 Dimensional Analysis for Pressure Induced Phase Change	33
3.3.1.1 Dimensional Analysis of Conservation of Mass	33

3.3.1.2 Dimensional Analysis of Momentum Equation	33
3.3.1.3 Dimensional Analysis of Energy Equation	35
3.3.2 Dimensional Analysis of Temperature Induced Phase Change.....	36
3.3.2.1 Dimensional Analysis of Momentum Equation	37
3.3.2.2 Dimensional Analysis of Energy Equation	38
4 RESULTS AND DISCUSSION.....	39
4.1 Calibration of Liquid Crystals	39
4.2 Dimensional Analysis.....	42
4.3 Results of Phase Change Experiments	45
4.3.1 Pressure Assisted Thawing of Ice I	46
4.3.2 Pressure Shift Thawing of Ice I.....	58
4.3.3 Pressure Shift Freezing to Ice I.....	69
4.3.4 Pressure Assisted Thawing of Ice III.....	77
4.3.5 Phase Change Processes of Ice V	81
4.4 Discussion.....	86
5 CONCLUSION AND FUTURE ASPECTS.....	91
6 APPENDICES.....	95
APPENDIX A	95
APPENDIX B.....	97
APPENDIX C.....	99
APPENDIX D	101
7 REFERENCES	103

KURZFASSUNG

Der unter Hochdruck (HD) induzierte Phasenübergang besitzt ein enormes Potential zur Anwendung in der Lebensmittelindustrie. Dichteunterschiede der verschiedenen Eistypen in Kombination mit Unterkühlung und schneller Eiskeimbildung beim HD-Prozess verringern beim Einfrieren den zellulären Schaden an Lebensmitteln im Vergleich zu Gefrierprozessen unter atmosphärischen Druck. Dadurch kann eine bessere Produktqualität erzielt werden. Diese Arbeit untersucht den Prozess des Phasenüberganges von Wasser unter HD mit Hilfe einer in-situ Visualisierungstechnik. Dabei werden erstmals Thermoflüssigkristalle zur Beschreibung dieses Prozesses unter HD verwendet. Diese Methode erlaubt, die Temperatur- und Strömungsfelder während des Überganges von Wasser in die verschiedenen Eistypen und umgekehrt unter Hochdruck zu analysieren. Aus den Geschwindigkeitsdaten werden zusätzlich Scher- und Dehneffekte, die Wirbelstärke und die Dissipation ermittelt. Dabei wird das System mathematisch mit den Masse-, Impuls- und Energie-Erhaltungssätzen beschrieben. Die Dimensionsanalyse und die Bestimmung der dimensionslosen Kennzahlen ermöglichen eine verallgemeinerte Aussage über den Gefrier- und Auftauprozess unter HD.

Die aufgenommenen Temperatur- und Bewegungsfelder zeigen charakteristische Unterschiede zwischen den verschiedenen Verfahren, wie zum Beispiel dem Hochdruckunterstützten Auftauen (PAT) und dem Hochdruckinduzierten Auftauen/ -Gefrieren (PST/PSF). Indes besteht eine starke Interaktion zwischen der Bewegung des Festkörpers und der flüssigen Phase. Beim Auftauen durch eine Druckerhöhung (PST) entstehen höhere lokale Geschwindigkeiten für beide Phasen verglichen mit dem PAT-Verfahren. Während der Prozesse PAT und PST können auch verschiedene lokale Strömungscharakteristiken beobachtet werden. Dabei kommt es örtlich zu Staupunktströmungen oder Dehnströmungen, überdies erzeugt PST zusätzliche Wirbel. Die unterschiedlichen Strömungsverhalten besitzen ebenfalls Einfluss auf die Temperaturverteilung. Das PST verursacht räumliche Inhomogenitäten während des Prozesses in der HD-Zelle, während beim PAT eine fast homogene Temperaturverteilung existiert. Dieses Phänomen beeinflusst das Konzept der homogenen Hochdruckbehandlung. Außerdem ist beim Auftauen von Eistypen, deren Dichte die von Wasser übersteigt (Eis III und V), eine umgekehrte Bewegung der festen Phase verglichen zu Eis I, festzustellen. Daraus resultieren unterschiedliche Strömungscharakteristiken.

Die Verwendung dimensionsloser Gruppen (Ec/Re , Ec/Fr , Ec/Ste), zeigt, dass konvektive Terme bei geringen Strömungsgeschwindigkeiten keinen signifikanten Beitrag zum System liefern. Dagegen nehmen Beiträge von der Wärmeleitung sowie des Gravitationseinflusses in der Bilanzgleichung größere Werte als die von Reibungskräften an.

Die bedeutendste Erkenntnis dieser Arbeit ist die Beschreibung der Interaktion zwischen zwei Phasen und den dabei auftretenden Inhomogenitäten während eines HD-Prozesses. Hiermit werden erstmalig experimentell bestimmte Temperatur- und Strömungsfelder während des Phasenüberganges unter HD in der Literatur präsentiert. In Bezug auf die kritischen Prozessparameter besitzen die hier analysierten und gefundenen Parameter keinen mechanischen Einfluss auf biologische Strukturen. Die Arbeit dokumentiert aber auch eindrucksvoll, dass die Verwendung der Hochdrucktechnologie und im besonderen der durch HD-induzierte Phasenübergang ein enormes Potential für die Lebensmitteltechnologie bereitstellt.

ABSTRACT

Among new treatments in high pressure (HP) technology, phase change is one of the processes attributed with high potential of application in the food industry. Density differences of ices formed under HP and supercooling as well as the rapid ice nucleation are reported to reduce cellular damage of the food and enhance the final product quality. This work is, therefore, aimed at investigating phase change processes of water under high pressure by help of an in-situ visualization technique. Thermo liquid crystal technology is applied to a HP phase change process which has not been previously accustomed. Through this method, thermal and convective fields during different phase change processes with different ice types are analysed. Two-dimensional velocity data are further handled to generate some fluid-mechanical parameters such as shear rate, strain rate, vorticity and dissipation. Additionally, the system is represented mathematically by continuity equations for mass, momentum and energy to render a global interpretation and proficiency in analysing process mechanisms possible. Dimensionless numbers are utilized to decide the remarkable terms effecting the process.

Convective and temperature field results demonstrate the differences between applied processes, such as Pressure Assisted Thawing (PAT) and Pressure Shift Thawing/Freezing (PST/PSF). A strong interaction is found between solid body motion and liquid phase. For PST process, where the thawing is taking place during pressure increase, enhanced local velocity values are obtained for both phases, in comparison with PAT. During both PAT and PST, different local flow characteristics are observed, such as stagnation or extensional flow regions. For PST vortex formation is also observed for the process. This different flow behaviour is found to be effective on temperature profile as well. PST process demonstrates inhomogeneities during phase change, whereas PAT has almost a homogeneous temperature distribution. This phenomena is prominent regarding the homogeneity concept for high pressure processing. Moreover, ice types which have higher densities than that of water (ice III and V) are distinguished with an opposite direction of motion of the solid body, regarding ice I. Thus, they demonstrate different flow characteristics.

Concerning dimensional analysis, dimensionless groups (Ec/Re , Ec/Fr , Ec/Ste) show that the contribution of convective terms to the system does not become significant at the low fluid velocities. Therefore thermal conduction and gravitational contribution are found to be more significant in comparison to frictional stresses.

As most prominent findings, the importance of interaction between phases and inhomogeneity during investigated processes have been presented in this contribution. Experimental determination of convective and temperature fields during high pressure phase change is achieved. The effect of the fluid-mechanical parameters on biological tissues has been found to be not crucial compared to critical parameters for biological processes. Nevertheless, HP technology and HP phase change processes should be further investigated as they possess an important potential in food industry, regarding their advantages reported in literature. This study, specifically, is attempted to be one of the essential contributions in this manner.

LIST OF NOTATIONS

Symbols

c_p	specific thermal capacity at constant pressure	J/kg K
f	weight percent	
g	gravitational acceleration	m/s ²
h	heat transfer coefficient	W/m ² K
\hat{H}	specific Total enthalpy	J
\tilde{H}	crystallization enthalpy	J
L	characteristic Length	m
L_f	latent Enthalpy	J/kg
m	mass	kg
P	pressure	MPa
q	heat flux	W
T	temperature	°C
\hat{T}	stress tensor	
ΔT	temperature difference	°C
t	time	s
V	volume	m ³
\vec{U}	velocity vector	m/s
U_0	inlet velocity	m/s
∇	del (nabla) operator	-
ρ	density	kg/m ³
μ	dynamic viscosity	kg/m.s
α	thermal expansion coefficient	1/K
δ	unit tensor	-
β	isothermal compressibility	1/Pa
λ	thermal conductivity	W/m K
τ	friction stress tensor	
γ	shear rate	1/s
ϵ	strain rate	1/s
ξ	volume percent	-
κ	volume (bulk) viscosity	
\vec{n}	normal vector	-

Φ	dissipation function	$1/s^2$
\dot{m}	mass rate of ice changes into water per second	kg/s

Dimensionless Numbers

Ar	Archimedes number
Ec	Eckert number
Fr	Froude number
Ga	Galileo number
Gr	Grashof number
Nu	Nusselt number
Pe	Peclet number
Pr	Prandtl number
Ra	Rayleigh number
Re	Reynolds number
Ste	Stephan number

Abbreviations

HHP	high hydrostatic pressure
PAT	pressure assisted thawing
PIF	pressure induced freezing
PSF	pressure shift freezing
PST	pressure shift thawing
TLC	thermochromic liquid crystal
DPIV	digital particle image velocimetry

Sub/superscripts

l, s	liquid, solid
0	reference property
*	dimensionless property
x, y, z	Cartesian coordinates

1 INTRODUCTION

High Hydrostatic Pressure (HHP) is gaining popularity in food industry because of its capacity to inactivate pathogenic microorganisms with minimal heat treatment, resulting in the almost complete retention of nutritional and sensory characteristics of fresh food without sacrificing shelf-life. Other advantages of HHP processing over traditional thermal processing include

- minimal thermal damage problems, retention of freshness, flavor, texture and color,
- no vitamin C loss,
- no undesirable changes in food during pressure-shift freezing due to reduced crystal size and multiple ice-phase forms, and
- minimal undesirable functionality alterations.

Changes that may be made improve functional properties of food constituents resulting in value-added products. Minimization of damage during pressure-shift freezing and thawing using HHP, non-thermally-induced enzyme inactivation, and desirable changes in starch-gelatinisation properties are some other examples of potential benefits of HHP. This study is aimed to make a contribution in HHP processing research by focusing on thermo- and fluid dynamical aspects of high pressure phase change transitions of water as being the most important constituent of all foods.

1.1 High Pressure Processing Applications

High hydrostatic pressure was adopted and adapted by the food industry from the isostatic pressing process used from a long time ago in the ceramics industry. Variations of the process depend on specific products, temperature, and pressure transmitting fluid (San Martin *et al.*, 2002, Otero & Sanz, 2003). Since then, high pressure technology has been effectively used, as it has the advantages of enhancement in the quality of final food product.

The first studies in high pressure date back to 1895 when it was realized by Royer that hydrostatic high pressure treatment kills bacteria. In 1899, Hite *et al.* reported the effect of high pressure on milk preservation, and in 1914 (Bridgman) the coagulation of egg white was

observed as a result of high pressure treatment. Since its rediscovery about 15 years ago, it has been at the centre of food research and development activities. Considerable advances in the utilization of high pressure in food science and technology have been made, especially in the last decade of the twentieth century. A major breakthrough occurred in Japan where high pressure processed jams prepared by unheated food processing appeared on the market in 1992 (Hayashi, 2002).

Initial emphasis was directed towards food preservation with the goal of extending product shelf life with minimum impact on product quality. Subsequently, the great potential of food and food constituents for physical modification of structure and function as well as the possibility for new process development (i.e. pressure assisted freezing or thawing) has been recognized. Meanwhile, commercial products have already been introduced into the markets of Japan, France, Spain and USA, although the diversity of products is still limited (Butz & Tausher, 2002). In 1992, high pressure processed apple, strawberry, and pineapple jams appeared in the Japanese market as the first commercialized high pressure processed foods in the world. A list of companies having products produced by HHP can be seen in Table A1, in Appendix A. The commercialization of high pressure processed orange and grapefruit juices was not successful due to the small market available for these products. Since 1995, high pressure processed grain products such as rice cake, hypoallergic rice and single-portioned cooked rice appeared in the market place with steady increase in production volume. At present, a high pressure research group, consisting of about 60 food companies, is conducting research on high pressure processed foods following the development of the true commercial scale high pressure machine with a capacity of 240 L (Suzuki, 2003). Another proof of this new interest was seen in 2002 in Australia with the establishment of a company to promote an innovative high-pressure food preservation technology throughout the Australian food industry (CSIRO, 1999).

Principally, the pressurization of the sample is carried out for the duration of a treatment in a pressure vessel containing a fluid (usually water) that acts as pressure transmitting medium. Pressure is applied isostatically, in other words, it is equally applied in all directions, which provides the homogeneous effect of high pressure. The pressure is held for the desired treatment time and then released. The generation of pressure inside the vessel may be achieved by three different ways. In direct compression, the volume of the treatment chamber is reduced by the action of a hydraulic pressure applied over a piston. For indirect

compression, an intensifier or a high-pressure pump is used to pump the pressurizing medium directly into the vessel to reach a given pressure. This is the method used for the HHP application in food processes. These systems also use a piston to increase the pressure, as in direct compression, but the displacement of the piston is achieved by pumping water with a high pressure pump into the vessel. The third pressurization method which is not used in the food industry so far, involves the heating of the pressure transmitting medium inside the vessel to cause expansion by increase in temperature.

Food treated with HHP has been shown to keep its original freshness, colour, flavour and taste (e.g. Krebbers *et al.*, 2002; Matser *et al.*, 2004; Butz *et al.*, 1997). Besides destruction of microorganisms, there are further influences of pressure on food materials like protein denaturation or modification, enzyme activation or inactivation, changes in enzyme substrate interactions and changes in the properties of polymer carbohydrates and fats (Butz & Tausher, 2002). Pressure induced inactivation of microorganisms is still under investigation. It is known that many microorganisms are lethally damaged by applications of pressures up to 500 MPa. Studies involving the mechanism of cell lysis show that pressure affects microorganisms in different ways. High pressure can cause an inactivation in membrane transport systems that results in a sublethal injury, or it can affect metabolic activity and damage the cell membrane (Hartmann & Delgado, 2003). When microbial cells and animal and plant tissues are pressurized at 100-400 MPa, cellular components such as metals, amino acids, and proteins become solubilized and extracellular compounds are permeated into cells and tissues (Hayashi, 2002). HHP also acts as a mechanical load on biological structures. Especially, when material composition of a biological structure (microorganism, tissue etc.) is heterogeneous, a deviation from hydrostatic stress case has to be expected. Although the outer load on the structure is hydrostatic pressure, internal stresses may exhibit shear stress (Hartmann & Delgado, 2003).

Researches carried out on high pressure processing agree that it is an instantaneous and homogeneous process. Because of this assumption of homogeneity, physico-chemical and biological processes are handled as a pure function of time. In a recent study Delgado and Hartmann (2002) have investigated and combined theoretical and experimental findings and concluded that the pressure effect can be considered as an instantaneous but not homogeneous in processing of fluid food. A flow field consisting of overlapping natural and forced convection directly influences heat and mass transfer during compression. Additionally, all

parameters of the processes such as biochemical and microbiological reactions can be interpreted correctly if and only if they are treated as fields but not just pure functions of time.

1.2 High Pressure Phase Change

The importance of phase transitions in food systems prompted some researchers to analyse those systems in detail. A phase is defined as a homogeneous portion of a material or system having a physically distinct bounding surface. Food materials may be single or multiphase and can be characterised based on the phases present (Rahman, 1995). Food systems are generally unstable due to chemical and physical reactions. Food components (proteins, carbohydrates, lipids, water,...) might undergo phase transitions due to a pressure or temperature change. Therefore, temperature and pressure are the two main state variables governing phase transitions in any system. As water constitutes 60 to over 90% of fresh foods, water content or water holding capacity is an important parameter that interacts with the value of a food. Other liquids like lipids or solid foods might also undergo phase transition in foods (LeBail *et al.*, 2002).

There are two main types of phase transitions that can be defined for food systems: first and second order. At first order transition the physical state of the material changes isothermally from one state to another by a release or absorbing of latent heat, such as ice-water transitions, melting of lipids, crystallization, condensation, evaporation, starch gelatinization and protein denaturation. Second-order transition occurs without a release or absorbing of latent heat because one phase evolves into the other as the temperature changes, so two phases never coexist. The glass transition is in the nature of a second order transition, which is generally characterized by a discontinuity in the physical, mechanical, electrical, thermal, and other properties of food materials (Rahman, 1995; LeBail *et al.*, 2002).

Effects of high pressure on the melting behaviour of lipids have also been investigated. Edible fats and oils represent mixtures of triglyceride species that exhibit phase transitions and show polymorphic crystal forms. Edible fats like milkfat, cocoa butter, etc., food emulsifiers like acetic esters of monoglycerides and model lipids like stearic acid, oleic acid, tristearin, triolein are used as samples. It is observed that the melting profile of investigated samples shifts during pressure changes in the system (Buchheim *et al.*, 1999). Therefore, oils which are liquid under normal conditions can become solid at elevated pressures (Kapranov *et al.*,

2003; Pehl, 2004). Optimization of the pressure-induced crystallization of edible fats can be important in modifying crystal size and shape in fat products like shortenings.

One of the frequently addressed phase changes has introduced an important application in food industry: low temperature processing. It is a well established technology for preserving foods. It prevents the activities of spoilage microorganisms, decreases the water content and activity in the food sample, reduces or stops the enzymatic and oxidative activity and finally provides an excellent overall safety and quality for the product. Therefore phase change and especially phase change of water as a main constituent of food has become an important application in food preservation.

During the freezing process the first thermal event involves cooling the sample below freezing point. A non-equilibrium, metastable state occurs before the induction of crystallization. Water can be undercooled by several degrees before nucleation begins. Once the critical mass of nuclei is reached, the system nucleates and releases its latent heat faster than heat is being removed from the system. The temperature then increases instantly to the initial freezing temperature. In aqueous solutions, the added solute will promote heterogeneous nucleation, thereby accelerating the nucleation process. During this period, crystal growth starts and fast freezing rates promote the formation of many small ice crystals. The partially frozen mixture will not cool until all of the "freezable" water has crystallized; hence, crystallization occurs at nearly constant temperature. It should be emphasized that due to the natural physics of nucleation, it is not possible to obtain a homogeneous nucleation also under high pressure conditions. High pressure helps to obtain more uniform ice nucleation during freezing. The freezing time is usually defined as the time from the onset of nucleation to the end of the crystal growth phase. After crystallization is completed, the temperature drops down as sensible heat is released.

The effects of high pressure on the solid-liquid phase diagram of water were studied first in 1900 by Tammann and further developed by Bridgman in 1912, but little attention has been paid to the potential food applications until recent years. Phase change diagram of water under high pressure and different ice types can be seen in Figure 1. ABCD and AEFG lines represent Pressure Assisted Freezing/Thawing and Pressure Shift Freezing/Thawing for ice I, respectively. During pressure assisted thawing/freezing the solidification line is crossed at constant pressure. Whereas in case of pressure shift freezing and thawing, phase change occurs during the pressure change in the system. With the same principle, line AEFJ stands

for pressure assisted thawing/freezing of ice III. In the ice V region, AHI is the process of pressure assisted freezing/thawing and IF line is the process of pressure shift freezing/thawing. Different classifications and terminology can also be found in literature for these processes (Urritia Benet *et al.*, 2004).

The different ice phases have been named in the order in which they were experimentally produced, from I to XII (all of them are not given in Figure), in a temperature range from -34.7 °C to 81.6 °C and pressures to 10⁶ GPa. All phases except IV and XII are stable over a certain change of temperature and pressure. As pressure increases, the ice phases become denser. They achieve this by initially bending bonds, forming tighter ring or helical networks, and finally including greater amounts of network inter-penetration (Chaplin, 2004).

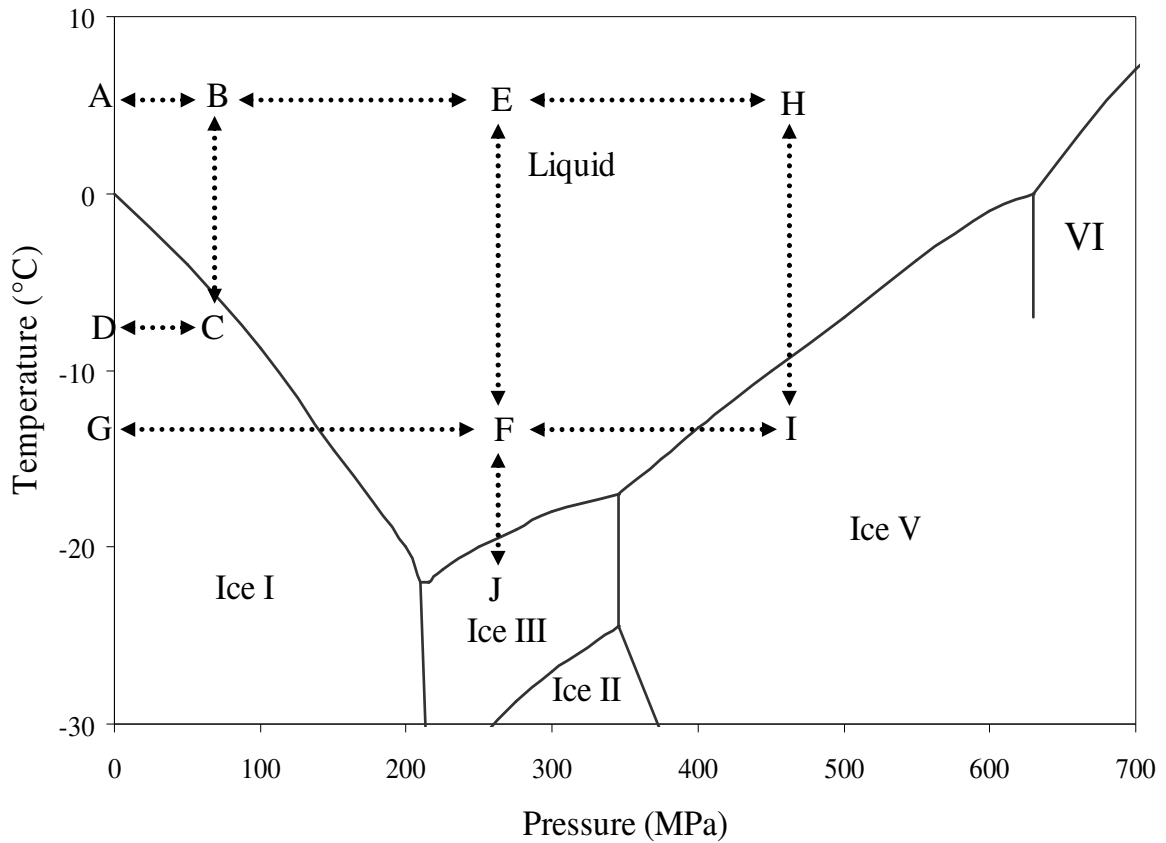


Figure 1: Phase change diagram of water under high pressure.

The application of high pressure reduces the freezing and melting points of water to a minimum of -22 °C at 207.5 MPa, as pressure opposes the volume increase occurring during the formation of normal ice crystals. This depression in freezing point and reduced enthalpy

of crystallization accelerate the phase change process. Within different polymorphs, ice I is unique in having a lower density than liquid water, resulting in a volume increase and may cause significant tissue or textural damage. The other ice polymorphs generally involve a decrease in volume relative to liquid state, which may result in reduced tissue damage compared with ice I. Even for type ice VI, it can be possible to obtain solid state at room temperatures (Kalichevsky *et al.*, 1995). The main advantage of high pressure is that it facilitates supercooling and promotes rapid and uniform ice nucleation and growth throughout the sample. Application of slow freezing generally results in larger ice crystals causing extensive mechanical damage. The other ice types that are not given in this study belong to pressures which are not considered in the frame of high pressure food processing.

The properties of water under high pressure are partly known since Bridgman has made possible the construction of data tables with great accuracy. The most recent formulations used to calculate thermodynamic properties of water have been released by the International Association for the Properties of Water and Steam (IAPWS) in 1995. Related properties of water are available in the pressure range of 0.1 to 400 MPa and temperatures as low as -22 °C. According to this release, especially along the phase change line, the thermal conductivity (λ) does not follow a simple function. Below 200 MPa and subzero temperatures, λ increases with pressure and temperature. The specific heat capacity (c_p) decreases with increasing temperature but increases with increasing temperature. It is reported that the viscosity does not show any significant change until pressures of up to 400 MPa are applied (Wagner *et al.*, 2000). In the region of subzero temperatures, a sharp increase has been observed in the viscosity, e.g. at a certain pressure of 100 MPa, a temperature decrease from 0 °C to -10 °C and -20 °C causes increases of 25 % and 33 % in viscosity, respectively. This behaviour of viscosity of water is also shown by Först *et al.* (2000). The density values increase with increasing pressure and decreasing temperature. Some other properties of water, like compressibility, expansivity, and specific heat have been studied at pressures up to 500 MPa, in a wide range of temperatures including the supercooled region (Ter Minassian and Pruzan, 1981). Thermodynamical properties of different phase transitions can be seen in Appendix A, Table A2.

1.3 Applications of Phase Change Processes under High Pressure

High pressure is still a relatively new technology in food science and applications of pressure assisted freezing/thawing are still under development. The earliest studies in this area concerned medical applications of high pressure, particularly for preservation of cell cultures and plant tissues. In recent years, the importance of these applications in the food industry has been realized and has been applied to a variety of products. Several contributions have reported on variations in temperature of different types of foods and fluids and the mechanisms, in response to both high pressure compression and expansion. The value and the sign of these temperature increments are dependent on conditions such as pressure and temperature at which they take place, the pressure increase rate, the food and pressurizing fluid. The observed change in temperature is the result of a process of heat transfer inside the high pressure vessel, which dissipates the heat liberated or to be absorbed in expansion or compression. The macroscopic effect in temperature depends on the thermophysical properties of food and fluid, those of the walls, convection and mobility in the vessel, and the heating or cooling supplied (Otero and Sanz, 2000). The temperature distribution in high pressure devices is said to be important in application of material properties and geometry in designing high pressure processing. A study deals with the numerical simulation of the temperature distribution on the walls during high pressure processing (Hartmann *et al.*, 2004). The preliminary results show that the thermal insulation in the container improves the homogeneity of the treatment as wall thickness decreases, and it also leads to a recognizably higher level of the treatment temperatures.

1.3.1 HHP Freezing

Freezing under HHP can be processed as either pressure shift or pressure assisted freezing (PSF and PAF). PSF is achieved by depressurizing the sample in the liquid region under HHP. While PAF is basically the normal freezing process occurring under a constant pressure. During freezing of foods, it is aimed to create a homogeneous matrix of small ice crystals. This state can be reached by rapid nucleation caused by supercooling, which can be defined as the reduction of the temperature of any liquid below the melting point of that substance's solid phase. When a product is initially kept in the liquid state at subzero temperatures combined with high pressure, a sudden pressure release allows a high degree of supercooling (~15 °C)

to be obtained, which also promotes rapid ice nucleation (Denys *et al.*, 1997). As in conventional methods, slow freezing may cause problems owing to structural damage, accelerated enzyme and microbiological activities, as well as potentially increased oxidation rates resulting from increased substrate concentration and the insolubility of oxygen in ice. Increased solute concentration can help to solve these problems by reducing diffusion rates. Moreover, rapid freezing processes induce cracking because of initial volume decrease (due to cooling) and the subsequent volume increase (due to freezing) as the sample cools and freezes from the outside in (Kalichevsky *et al.*, 1995). This increase in volume is contributed to ice I formed, which uniquely has a lower density than that of liquid water at 0 °C, and results in a volume increase of 9% on freezing at 0°C, and about 13% at -20 °C, which may cause significant tissue or textural damage. However, under high pressure, several kinds of ices (ice II-IX) are formed whose densities are greater than that of water and cause a lesser extent of tissue damage (Li & Sun, 2002). Regarding application of the process, the large latent enthalpy (ΔH) of ice formation causes freezing to have a warming effect. Therefore an additional cooling of sample is required to enable complete freezing to occur. This sometimes may limit the sample size that can be successfully frozen since incomplete freezing could result in sample deterioration, arising from the growth of ice crystals and the melting of smaller ice crystals.

In a study conducted by Kanda and Aoki (1992), HHP freezing is applied to tofu, and results indicated that ice-crystals were uniform, granular, and very small in size. Tofu is subsequently thawed at room temperature and retains its original shape, structure, taste, and texture. A similar study conducted by Fuchigami *et al.* (1998) examined high pressure-freezing (100 to 700 MPa at -20 °C) effects on the textural quality and histological structures of Chinese cabbage. Freezing of samples at 100 MPa (ice I) and 700 MPa (ice VI) resulted in increased rupture strain, however, texture was comparatively intact at 200 MPa (liquid), 340 MPa (ice III), and 400 MPa (ice V). Also, pectin release and histological damage in samples frozen at 200 and 700 MPa were less than in those frozen at 100 and 340 MPa. They reported an increase in both textural and histological attributes of pressure-frozen samples as compared to results from traditional freezing.

Koch *et al.* (1996) observed that pressure-shift freezing of potato cubes resulted in less damage of the cell structure, less drip loss and less enzymatic browning than conventionally frozen cubes. The quality of pressure-frozen foods investigated and compared with that of

freeze-dried products. It is concluded that pressure-freezing followed by air-drying resulted in less textural damage, less shrivelling, more rapid dehydration and more uniform rehydration.

Deuchi and Hayashi (1992) examined the application of HHP at subzero temperatures to preservation, rapid freezing, and rapid thawing of foods. They stored non-cooked foods, microorganisms, and freeze-sensitive microorganisms at temperatures from -5 to 20 °C with pressure applied from 50 to 200 MPa for a few days or weeks. It is figured out that strawberries retained fresh flavor, color, and texture; raw pork had no drippings, and most microorganisms (coliforms, *Enterobacteriaceae*, enterococci, and LAB) are reduced in number. Thus, freeze-inactivation of enzymes is partially prevented. Storage of foods under moderate pressure at subzero temperatures preserved the natural characteristics of foods without microbial spoilage and damage. The rapid freezing of food using HHP is also studied by pressurization up to 200 MPa followed by cooling to -20 °C and rapid release of pressure and is found that the procedure is useful because of uniform formation of small ice-crystals throughout the food material, preserving the sensory characteristics of food.

On the other hand, Knorr *et al.* (1998) studied the effect of HHP on phase transitions of food, and performed a study of high pressure-freezing and thawing of potato. A high pressure vessel is designed which can withstand subzero temperatures, and results suggested that, due to the transient nature of heat transfer, fast removal of latent heat is a major engineering challenge during pressure-freezing and thawing.

One of the most recent studies concerning pressure freezing is performed by Molina-Garcia *et al.* (2004). They investigated structural changes in meat which is frozen to the ice VI region. The result of examining both water and meat ice VI nucleation behaviour and its effect on meat structural properties is promising for the future application of this process to preserve biological material and food under conditions not leading to ice damage, with little requirements for continuous cooling. The potential benefits of PSF are illustrated in an experimental study using gelatine gel model food (Zhu *et al.*, 2005). Cylindrical specimens of gelatine gel are frozen by PSF at 100, 150 and 200 MPa and -8.4, -14 and -20°C, respectively. Conventional air freezer and liquid immersion freezing are also performed at -20 °C. The conventional air freezer produced much larger ice crystals than liquid immersion freezing and PSF. Compared to conventional freezing at the same temperature, PSF produced smaller ice crystals. The effect of stress during high pressure processing is also investigated. For biological tissue, during freezing, a frozen layer appears at the surface of the product. At

the same time, the formation of ice at the core will result in an increase in pressure. Radial and tangential stresses develop during freezing (Shi *et al.*, 1999). On the other hand, a depression of the initial freezing point due to pressure increase will result in a partial thawing leading to a release of stresses (Otero & Sanz, 2000).

Ice microstructure during high pressure processes is also evaluated as an important subject by several researchers. They figured out the effect of supercooling obtained during rapid depressurization in different foods. Chevalier *et al.* (2000b) showed that in the case of turbot fish, a pressure below 140 MPa allows to minimize the negative effect of high pressure on texture due to protein denaturation. The size and location of ice crystals in large meat pieces as a result of PAF are compared with those obtained by air-blast and liquid N₂. Air-blast and cryogenic fluid freezing, which both have thermal gradients, showed non-uniform ice crystal distributions. PAF samples both at the surface and at the central zones, showed similar, small-sized ice crystals (Martino *et al.*, 1998).

1.3.2 HHP Thawing

Thawing processes under high pressure, as previously mentioned, can be carried out pressure assisted or pressure shift thawing (PAT and PST). A frozen product can be forced to the liquid region in the phase diagram by applying high pressure, thus allowing faster thawing. For example pressure treatments of 200 MPa for 30 min at 5°C were found to be sufficient to completely thaw ice prepared at temperatures in the range -10 to -30 °C (Deuchi and Hayashi, 1992).

High pressure thawing of frozen meat requires only one-third of the time necessary at atmospheric pressure but produced sensory qualities comparable to those of conventionally thawed products (Li & Sun, 2002). Effects of PST on meat products generally include a reduction of the time required to completely thaw the product and better retention of quality factors compared to conventional methods. The increase of thawing rate associated with PST is mainly attributed to the larger temperature gradient between the melting product and the ambient pressure transmitting medium resulting after compression. Negative effects are generally discoloration and whitening of meat, depending on the pressure applied.

High pressure thawing of two selected sea foods is evaluated in comparison with thawing in water at atmospheric pressure (Rouillé *et al.*, 2002). Results showed that for both products,

the thawing drip was significantly reduced when thawed under high pressure. Samples of Atlantic salmon were frozen by different applications and water immersion thawing and high pressure thawing were applied (Zhu *et al.*, 2004). High pressure caused a depression of the ice-melting temperature during thawing and accelerated the thawing process. Color changes in fillets treated by HP became significant when thawed at pressures above 150 MPa. Significant modification in texture appeared at 200 MPa. PST was desirable to minimize discoloration and toughness of samples at pressures below 150 MPa.

In one of the studies on rapid thawing of frozen foods, ice (at -10, -15, -20, and -30 °C) is pressurized from 50 to 200 MPa, and food samples are held at 5 °C for 30 min, and it is found that all ice was completely thawed. Thus, rapid thawing of foods is a possible way to avoid qualitative changes, provided that processing conditions like temperature, pressure and time are carefully selected (Deuchi & Hayashi, 1992).

Denys *et al.* (1997) also state that high pressure thawing involves forcing a frozen sample to the liquid area of the phase diagram, thus increasing the thawing rate, if the appropriate heat of fusion is provided. A comparison between the influence of pressure assisted thawing at 200 MPa and that of conventional thawing in 15 °C water at ambient pressure on the quality of thawed fish fillets has been carried out by Schubring *et al.* (2003). Data showed that pressure assisted thawed and water thawed fillets exhibit visual differences. Organoleptic characteristics of the high pressure treated fillets were better compared to the conventional water thawed samples before cooking. Further differences were observed in the total viable count of micro-organisms, pH value, water binding ability, instrumentally evaluated texture parameters and in thermo-analytical behaviour. Also, the effects of the selected treatments differed according to the fish species. Consequently, the specific properties of samples must be taken into consideration when designing pressure supported processes.

During PST, a temperature decrease is generally observed, which can be attributed to the absorption of latent heat required for the melting process, and the inability to simultaneously supply this amount of heat. Limitations on the application of high pressure thawing are mainly high cost, the same as high pressure freezing encounters, and pressure-induced protein denaturation and meat discoloration. However, these obstacles can be overcome by optimizing the thawing conditions used. A detailed examination of studies carried out with high pressure thawing, revealed a common conclusion that thawing generally occurs more slowly than freezing, which potentially allowing further damage to the sample. Faster thawing

reduces the loss of liquid retention properties and can improve colour and flavour preservation in fruit. The risk of detrimental phenomena such as recrystallization, solute concentration effects, and microbial growth is markedly reduced. It is likely that PAT will have many applications in food and medical fields, especially in cases where significant sample deterioration occurs during thawing. Apparently, Japanese R&D personnel are aiming to commercialize small high-pressure units for thawing fish in sushi bars, and also for other commercial applications where quality and freshness are of primary importance (Kalichevsky *et al.*, 1995). Therefore, studies on source data affecting high pressure thawing processes and its parameter study is important to its commercial application.

1.4 HHP Visualization and Modelling

The application of in-situ high pressure systems in food processing studies is a novel technique that has only recently become a source of interest. Several visualization techniques have been adopted for this aim. Diamond anvil cell is one of the methods applied in visualization experiments under high pressure, as diamond is the hardest and least compressible material, and has the important property of being transparent to most of the spectrum of electromagnetic radiation. In its configuration, very little force is required to create extremely large pressures in the sample chamber, and, because of the transparency of diamond, the sample may be examined in situ (while at elevated pressure) by optical microscope, spectroscope (Raman, infrared) and diffraction techniques (HPDO, 2003). For food research, one study used the diamond anvil cell to examine pressure-induced gelatinization of starch with Fourier transform infrared (Rubens *et al.*, 1999). The spectra of starch gelatinization, as well as in-situ observation of gelation are performed and the swelling of starch granules at pressures where gelation occurs is observed.

Only a few studies have discussed an optical in-situ observation of high pressure processing. A high pressure cell developed that can stand pressure of 300 MPa in combination with an inverse microscope (Bauer *et al.*, 2004). Starches from different sources are analysed and their granule structure during pressurization are observed and compared.

Another optical system for the measurement of pH value of foods during high pressure treatment up to 450 MPa is developed by Stippl *et al.* (2003). It is managed to have a satisfactory accuracy of 0,24 pH units in measuring pH of fluid foods. The first visualization

of temperature fields in liquids at high pressure is achieved by using thermochromic liquid crystals in 2000 (Pehl *et al.*, 2000 and 2002). This system and technique are further used for new applications in this study.

A modular optical system is also being developed by Lopez *et al.* (2004) for real time and in-situ studies. A modular optical rotation instrumentation is designed using a photoelastic modulator and a temperature controlled cell to simulate food processes. The prototype has been tested for in-situ optical polarization measurements (Torres and Velazquez, 2004).

In regard to the phase change phenomena and moving ice front during freezing, the only contribution that studied particle image velocimetry and thermometry for investigation of phase change of water under ambient pressure has been carried out by Kowalewski *et al.* (1998). Temperature and velocity fields are determined for natural convection in freezing water with two different arrangements - differentially heated cavity and lid cooled cavity. In the former, the competing effects of positive and negative buoyancy force result in a flow with two distinct circulations. In the latter, a complex spiralling structure is observed, which transports fluid up along the walls. The numerical simulation of the system is validated by those experimental results.

Modelling studies are helpful in understanding the thermodynamics of the system, and therefore some of the studies about HHP Modelling, especially about phase change processes, will be presented and discussed. One of the main difficulties when modelling heat transfer in high-pressure processes is the lack of appropriate thermophysical properties of the processed materials under pressure. The current literature available lacks enough thermophysical data for food and its components, even for the main one, water, to be used in modelling processes in the high pressure domains. The temperature range of interest for high pressure studies in food, considering the special needs of subzero temperature applications, can be stated from positive temperatures to -22 °C while the pressure range is over 500 MPa (Otero & Sanz, 2003).

Otero *et al.* (2002) investigate and review about some interrelated thermophysical properties of liquid water and ice I (like thermophysical expansion coefficient, isothermal compressibility coefficient, specific volume and specific isobaric thermal capacity) for the pressure and temperature range of interest under high pressure food processing (including supercooled water). That these properties are in reference to free water is an important point

to keep in mind. However, in a food matrix, water exists in various forms. This point should be taken into consideration using those parameters.

The most pronounced advantage of high pressure processing, as compared to thermal treatments, is probably that high pressure acts instantaneously throughout a mass of food. However pressurisation/depressurisation always induces a temperature increase/decrease due to the work of compression/expansion in both the food and the pressurising fluid. During modelling, this temperature variation produced by an adiabatic pressure change can be obtained by means of the well-known thermodynamic equation (e.g. Kalichevsky *et al.*, 1995), where p is pressure, T is temperature, v is volume, c_p is specific thermal capacity, and α is the thermal expansion coefficient:

$$\frac{dT}{dp} = \frac{T.v.\alpha}{c_p}$$

As can be seen, dT/dp depends on the sample composition and its physical state through these parameters, but these parameters also depend T and P , that makes its calculation complex (Otero & Sanz, 2000b). One of the other difficulties in modelling is the calculation of the adiabatic temperature increase/decrease after the pressure build up/release. Moreover, the convective heat transfer that takes place in the pressurising fluid between the inner wall of the vessel and the sample causes difficulties in calculation. Any model developed for a classical freezing process at atmospheric pressure would be used for high pressure process if appropriate thermophysical properties are considered. In the high pressure shift freezing process, the models have been developed have the difficulty to set parameters for the phenomenon of uniform nucleation induces by pressure release (Otero & Sanz, 2003).

Thermodynamic and fluid-dynamical effects of high pressure treatments of fluid food systems were numerically analyzed by Hartmann and Delgado (2002a) and also experimentally investigated (Pehl *et al.*, 2002). They prove that the uniformity of a high pressure effect can be disturbed by convective and conductive heat and mass transport conditions that are affected by parameters such as the compression rate, the size of the pressure chamber or the solvent viscosity. In another contribution by Hartmann and Delgado (2002b) the non-homogeneity of pressure treatment of food as well as some reasons for its generation in liquid food components are discussed.

Modelling involving a phase change at atmospheric pressure in foods is a difficult task because of its heterogeneous structure. For pressure assisted freezing where phase transition occurs under constant pressure, temperature is lowered to the corresponding freezing point. Substantial reductions in freezing times have been reported (Knorr *et al.*, 1998) in comparison with the times required to complete the process at atmospheric pressure. Reduction in time can be attributed to a decrease in the latent enthalpy values of water.

Sanz and Otero (2000a) present a comprehensive vision of the heat transfer process involved in high pressure shift freezing, taking into account the metastable conditions reached at atmospheric pressure after a fast expansion. They also produce a mathematical model to predict the freezing times for a finite cylindrical food model that allowed comparison of high pressure shift and atmospheric pressure freezing processes. Le Bail (1997) investigate the problem of determining the appropriate thermophysical properties of water under pressure, including phase change temperature and latent enthalpy. Numerical results fit well with the experimental data obtained under atmospheric pressure and high pressure in spite of the differences found at the beginning of the process. Difficulties in modelling arise because the phase change energy at the surface during compression is not taken into account. Moreover, the non-adiabatic nature of the pressurisation step may induce non-homogeneous thawing processes.

A numerical study about high pressure thawing presented by Denys *et al.* (1997), is a numerical solution for two-dimensional heat transfer to model heat conduction during high pressure freezing and thawing of tylose cylinder. An energy balance is applied to calculate the temperature in the sample after pressurisation, assuming that the sensible heat, lost during the observed temperature decrease is added to the enthalpy value of the frozen product. This model allows a non uniform initial temperature distribution in the sample before compression.

Recently, high pressure induced freezing and thawing processes are investigated by means of modelling and numerical simulation (Kowalczyk *et al.*, 2004). Those processes are investigated for both atmospheric and high pressure cases, and good agreement has been found with experimental data. For high pressure case, as already mentioned, supercooling has not yet been implemented in the simulation. Other than that, the deviations observed at the end of the solidification process are related to the use of pressure independent, rather than dependent latent heat. The influence of the non-homogeneous wall temperature conditions is another strong influence in this phase. It has been found that convective fluid motion under

high pressure has a different characteristics since the density anomaly of water disappears under high pressure. Thus, freezing/thawing processes where free convection plays a major role differ significantly from the atmospheric case when high pressure is applied.

1.5 Objectives

The main purpose of this study is to visualize and investigate the thermal and fluid dynamical behaviour of phase change processes under high pressure by implementation of an in-situ measuring technique. High Pressure Particle Image Velocimetry and Thermography techniques are used to analyse the velocity and temperature fields, respectively. The following questions and statements represent major achievements during the course of this study:

How is the flow field distribution during the formation or degradation of different ice types with different operations? Is it possible to analyse a solid-liquid flow with a classical PIV application at high pressure and subzero temperatures?

Are there any differences between phase change processes of different ice types concerning the fluid dynamical properties? If yes, which process parameters are the most dominant ones in creating these differences?

Is it possible to use temperature sensitive liquid crystals to investigate the phase change process by help of thermometry technique in a two phase system at high pressure and subzero temperatures?

What is the relationship between fluid motion and temperature distribution during phase change processes under high pressure?

Which dimensionless numbers can be used to characterize the phase change processes under high pressure? What is the relationship between convective and dissipative transport?

An additional goal is to analyze the fluid dynamical equations on the component basis to compare shear forces, strain rate and dissipation for different processes. Is it possible to conclude that those forces can be effective on the sensorial quality parameters of a biological tissue or a food subjected to a high pressure phase change operation?

In this work the most prominent contribution is the achievement of in-situ observation and fluid dynamical analysis of a phase change system under high pressure. Moreover, observed inhomogeneity during processing even in a relatively small volume reveals another angle in the discussion of homogeneity of high pressure processing.

2 MATERIALS AND METHODS

2.1 High Pressure Unit

The main experimental setup consists of a tempered high pressure optical cell (SITEC, Switzerland) which can be seen in Figure 2.1 (Pehl 2004). The cell body is embedded in a tempering bath which makes it possible to control the temperature in the range from $-30\text{ }^{\circ}\text{C}$ to $+120\text{ }^{\circ}\text{C}$. The maximum allowable temperature and pressure of the cell body are $120\text{ }^{\circ}\text{C}$ and 700 MPa , respectively.

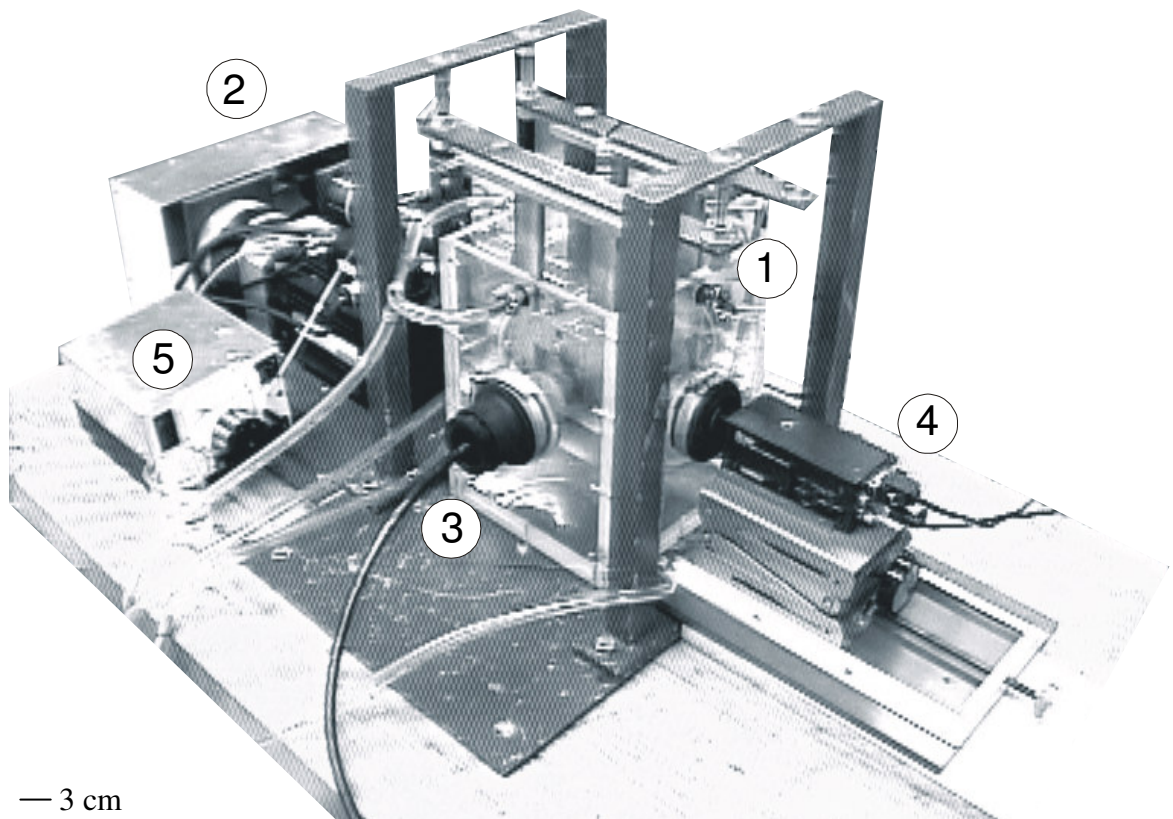


Figure 2.1: Experimental setup: (1) Temperature bath and high pressure cell (2) Pressure generator (3)light Source (4) RGB Camera (5) Filling Pump

The cell has a volume of 2 ml and the total liquid volume in the device is 8 ml. Synthetic sapphire (AlO_2) windows with a diameter of 6 mm are used to reach the system optically. One

of those windows is used to illuminate the cell. This is achieved by a sheet of white light from a xenon lamp. Light from the source is first subjected to a split having a 0,25 mm width, then to a convex lens to obtain a light sheet in the center of the cell cavity. The plane is observed by a 3-chip RGB (Red-Green-Blue) CCD camera which is placed at a right angle to the incident light sheet. The camera has a resolution of 752 x 582 (H x V) pixels. A classical analog SVHS video recorder is used to record the images. The acquired images are then digitalized with the help of a Frame Grabber.

High hydrostatic pressure (HHP) can be generated either by direct compression or by indirect compression. Direct compression is piston-type compression in which the pressure medium in the high pressure vessel is directly pressurised by a piston. In case of liquid food, the food itself acts as the pressurizing medium. The indirect compression method uses a high pressure intensifier which pumps the pressure medium from the reservoir into the closed and de-aerated high pressure vessel, until the desired pressure is reached. Most of the industrial cold, warm and hot isostatic pressing systems use the indirect pressurisation method (Mertens, 1994). There are two major types of high pressure processing of food products: the conventional and semi continuous systems. Batch systems can process both liquid and solid products, but these have to be pre-packed. Inline systems can be applied only to pumpable products like juices. The product is pumped into the pressure vessel and pressurised using a floating piston (Van den Berg *et al.*, 2002). In this study, pressure in the system is built up by direct compression with a high pressure piston pump driven by a step motor. Different pressure change rates can be adjusted by a variable motor speed, which can be given by control software. Pressure is measured by a sensor placed in the supply channel. Temperature inside the cell can be measured by means of a thermocouple (type J) located at the middle top of the pressure cell. This opening is also used as discharge channel with a suitable arrangement.

Geometrically, the high pressure cell is a perpendicular intersection region of two cylinders. Four windows are located at the flat surfaces of those cylinders. For a detailed information about dimensions a technical scheme of the system can be seen in Appendix B.

2.2 Experimental Methods

Experiments are carried out according to the phase change diagram of water (Figure 1) and, principally, using methods similar to the ones that are used by Pehl (2004). In all experiments, distilled water is used in which the liquid crystals are dispersed. Concentration of liquid crystals is determined by preliminary experiments. Excess amount of liquid crystals causes a cloudy formation which obstructs proper visualization. The liquid crystals are used at a concentration of 0.7 % (v/v).

For all experiments under subzero temperatures, it is necessary to increase the pressure in the cell at the beginning of the experiment, i.e. before cooling down the cell. This is due to the physical properties and the construction of the sapphire windows. For pressure shift thawing experiments of ice I (GF line in Figure 1), the cell is then cooled down to temperatures in the range of -10 °C to -20 °C. During cooling, phase change of water causes a pressure increase due to volume expansion. The required pressure for the experiment in the cell is set by increasing or decreasing the pressure by help of the pressure motor. After the phase change is completed and the pressure is equalized the pressure is increased with a rate of approximately 15 MPa/s (for water at 20 °C). The images are acquired during the phase change process. For pressure shift freezing experiments of ice I (FG line), the cell is pressurized up to pressures between 100-200 MPa and then is cooled down to temperatures at which water stays in the liquid phase. After reaching steady state, the cell is depressurized till the phase change line is crossed at a corresponding phase change temperature and pressure. The image sequence of the process is recorded. In all pressure shift processes, temperature is kept constant at start temperature.

For pressure assisted thawing of ice I (CB line) the temperature of the cell is cooled down to temperatures between -5 °C to -15 °C. After reaching stable conditions in the ice I region, temperature of the tempering bath is increased to 5 °C. The phase change process is recorded.

For ice V, the same experiments are carried out in the same temperature range like ice I but at pressures between 400-600 MPa. For ice III, because of the narrow range of pressure, it is only possible to observe pressure assisted thawing process (JF line) at temperatures of -21 to -22 °C and pressures between 250-300 MPa.

Cooling of the cell is achieved by using a conventional thermal bath from HAAKE, Germany. For ice III experiments, LAUDA Ultra-Cryomat (K50-L) is used because of its high performance at extreme temperatures.

All recorded images are digitalized and saved as single pictures by means of a frame grabber. The time interval between the pictures is selected as 1 sec for temperature visualization to make it possible to synchronise corresponding temperature and pressure data. For velocity field calculations this time interval is selected as 100 ms, details will be discussed in Convective Field Analysis part.

2.2.1 Thermochromic Liquid Crystals

Thermochromic liquid crystals (TLCs), as their name implies, react to changes in temperature by changing color. They have chiral (twisted) molecular structures and are optical-active mixtures of organic chemicals. Their use in technological devices and as measuring technique have been started some decades ago.

TLCs principally reflect incident white light selectively and display colours whose wavelength is a function of temperature. Liquid crystal change in appearance is concentrated over a range, typically few Kelvin degrees, and this field is called colour play interval and represents the temperature range within they can be used as temperature indicators. Liquid crystal imaging is ideal for producing a qualitative picture of a field (two or three dimensional) in which the temperature varies both spatially and temporally. Quantitative measurement systems, however, require that the temperature be associated with a measurable scalar that represents colour of the liquid crystal medium/surface at every pixel in an image field (Stasiek *et al.*, 1997).

The effect of pressure on TLCs has been studied since 1970s. All of those studies were focused on the investigations of liquid crystalline mesophases as function of temperature, pressure and the chemical composition. It was stated that pressure causes a red shift of the reflected light for most of different types of liquid crystals (Pollmann, 1987).

Pehl *et al.* (1999) studied applicability and suitability of TLCs to high pressure processing. In this study, it is shown that the wavelength of the reflected light show opposite changes when TLCs are subjected to temperature and pressure changes separately. The characteristic

temperature pressure relation for a TLC type should be analyzed for the system to which it is applied.

TLCs are characterized with their starting temperatures and bandwidths. The bandwidth is defined as the temperature difference between two end start temperatures. There are possible different start temperatures and bandwidths commercially available. The temperature range of the products changes between -30 to 120 °C with minimum bandwidth of 0.5 to a maximum of 30 °C. Stability arrangement of given bandwidth better for higher temperatures. As the start temperature decreases, the maximum bandwidth is increasing.

The specific TLC used in the experiments is BM/R-30C2W/S-40 from Hallcrest Inc., England. The abbreviation BM stands for microencapsulated TLC. Microencapsulation process is applying a polymer coating to each single liquid crystal and it provides stabilization and protection for TLC mixtures. R-30C defines a red start temperature of -30 °C. 2W is the bandwidth of the TLC (the calibration made by Hallcrest states additionally that specific bandwidth of the product is 1.92 °C). S-40 stands for an aqueous suspension of TLC from 10 to 15 µm in diameter (50 to 100 µm diameter is also available).

The thermal reaction time of TLC is analysed to see the effect of sudden pressure changes in the system. The response time is the time between two equilibrium phases of the reflected wavelength. According to the literature, response time of liquid crystals can range between a few milliseconds up to some seconds (Ferguson, 1968). For the specific TLC used, the response time is determined as 190 ms (Pehl, 2004).

2.2.2 Temperature Field Analysis

Quantitative analysis of images displayed by the liquid crystals requires that the temperature be associated with a measurable scalar that represents the colour of the liquid crystal medium at every pixel in an image field. Two different methods are reported in literature to reach this aim. One is using a spectral reflectance property of the liquid crystals. Afterwards, pixel by pixel spectral-analysis of displayed images and an application of multiple regression method give the final temperature information (Akino *et al.*, 1989). Second method is named as true-colour or colour image processing, which principally has been widely used in many studies (Ozawa *et al.* 1992; Kowalewski *et al.*, 1998; Stasiek *et al.*, 1997; Nozaki *et al.*, 1995; Hollingsworth & Hay, 1998; Pehl *et al.*, 2000). The image processing system includes a

video-camera to record the image, a frame grabber to digitise it and an appropriate software to convert the colour pattern into the temperature field. The last step can be performed by the conversion of the image, pixel by pixel, from the RGB (Red-Green-Blue) domain into the HSI (Hue-Saturation-Intensity) domain. Hue value is an angle defined in a polar chromaticity space determined by the intensities of the red, green and blue primaries recorded by the image acquisition equipment. It represents the dominant wavelength of the colour that depends directly on the TLCs temperature. HSI scale can be written in terms of RGB values according to the following relation

$$I = \frac{1}{3}(R + G + B)$$

$$S = 1 - \frac{3}{R + G + B} [\min(R, G, B)]$$

$$H = \arccos \left\{ \frac{1}{2} \frac{[(R - G) + (R - B)]}{[(R - G)^2 + (R - B)(G - B)]^{1/2}} \right\}$$

From those values only the hue value can be retained since it is related to temperature through a relationship that can be obtained by a calibration experiment. The hue value is calculated as a normalized value of the dominating colour. The hue-temperature relationship of a liquid crystal depends not only on the liquid crystal compound but also on the experimental conditions, like light intensity, angle of view, presence of glasses between the camera and the TLC medium. Therefore, calibration of a TLC is unique for the system that it is applied. Before the calibration experiments, the pressure temperature relationship of the TLC is determined by characterization experiments. For this aim TLCs, having a density of 1 g/ml, are dispersed in distilled water and the temperature is arranged to a selected temperature, which changes in the range from -10 °C to 25 °C with 5 °C increments. After reaching the required temperature, the cell is pressurized and at every 500 Bar it is waited till temperature equalization is reached. After temperature equalization the points are recorded where a colour response can be observed by eye. In the second run, pressure and temperature values determined at those points are selected as initial conditions. Pressure is held constant in the cell and temperature is increased to detect all colour responses. The resulting pressure-temperature relation of TLC shows the characteristics of the TLC (it will be discussed in detail in Section 4.1). Calibration experiments are carried out mainly with the same procedure

as the second part of characterization experiment. Five different pressure values are selected according to pressure-temperature conditions of the investigated region in the phase change diagram of water. The pressure is set to a required value and temperature of the cell is increased with ~ 0.2 °C increments. After reaching steady state conditions (waited about 30 minutes) in the cell the corresponding images are recorded starting from blue response. Consecutively green and red responses are also recorded.

Digitalization of acquired images is carried out by using Optimas as software program and PXC 2000 Precision Colour frame grabber. As image enhancement procedures, median filter and stop motion filter are used for removing bright or dark spikes and to reduce noise. Then a region of interest is selected which corresponds the diameter of the visual area in the cell. The processing band of the images is transformed from RGB band to HSI band and hue value of the images is obtained. For each hue value, 100 images are analysed and each experiment is repeated three times, to prevent the possible measurement errors. Hue property can have values between 0 - 255, and the blue colour corresponds the highest hue values and it is followed by green and red respectively.

The digitalized images obtained from phase change experiments are also subjected to the same image enhancement processes. Again, in HSI band, hue values are extracted pixel by pixel for the region of interest by help of a macro in Optimas. These position-hue value data of images are then further converted to position-temperature information by help of a Fortran program which calculates temperature at any given pressure value by evaluation of splines for the calibration curves. Data analysis program Tecplot is subsequently used to analyse the data.

2.2.3 Convective Fields Analysis by High Pressure Digital Particle Image Velocimetry

Evaluation of velocity fields is carried out by help of a classical Digital Particle Image Velocimetry (DPIV) application. It has been applied to high pressure processing and called by Pehl as High Pressure DPIV. Principally, PIV compares two images with known time spacing Δt to obtain velocity measurements. Seed particles should be dispersed within a 2-D slice of the flow area. In this system liquid crystals are used as seed particles and light sheet for 2-D slice. Acquired images are first masked by Optimas as it is explained in previous section. Then, each pair of images are analysed with a PIV algorithm. The fluid velocity is estimated by correlating the two image subsections from successive frames (Images 1-2, 3-4, 5-6,...). Clusters of seed particles in each sub-image will result in a peak of the cross-correlation to

produce displacements between frames. An inverse Fast Fourier transform is then performed on the convolution product with the correlation peak corresponding to the fluid displacement. This is repeated for each subsection of the images, producing vectors, which describe the flow field.

In the current work as DPIV application EDPIV is used, which is a program developed by Lichuan Gui (1997). Settling parameters and specific methods are determined with preliminary experiments. Those parameters should be chosen suitable for the current system characteristics, such as lighting, concentration of the particles, resolution of images, etc. As interrogation scheme the central difference image correction (CDIC) method is selected. In principle, CDIC method is combination of a modified image correction method with the FFT-based correlation algorithm. In this method, additional to classical algorithms, the evaluation error resulting from the image pattern distortion can be effectively reduced. CDIC enables a reliable and an accurate evaluation of digital PIV recordings (Wereley & Gui, 2003).

The analysed images have resolution of 768x576 pixels. Interrogation window size is chosen as 36x36 pixels, interrogation grid size is applied as 18x18 pixels and a searching radius of 12 pixels is selected after preparative experiments. A 4-point image correction method is used. Target vector function is also activated to apply a vector correction with the target vector method. Detailed explanation and discussion of these functions can be found in Wereley & Gui's (2003) study.

The smallest possible time interval between images is 0.04 seconds. The time interval between image pairs should be selected in such a way that displacement of particles can be detectable in the consecutive searching windows. The time interval between images is determined as 100 ms, which can be set as a control parameter during digitalization. The resulted velocity data is compatible for analysing further in Tecplot.

3 THEORETHICAL CONSIDERATIONS

3.1 Basic Equations of High Pressure Processing

Kowalczyk (2002, 2004) presents a mathematical model for phase change processes under high pressure, for the first time. Kowalczyk's model approaches the system as two homogeneous phases and reformulates enthalpy-porosity model (for detailed information see Voller *et al.*, 1989). A similar model is used to represent the system under investigation. Conservation equations for mass, energy and momentum are the basis for the mathematical model (e.g. Spurk, 1997). The equations for compressible media are presented in differential form and it is assumed that the water in the system is homogeneous in both phases, and chemically inert. For simplicity, Cartesian coordinates are used.

3.1.1 Conservation of Mass

Equation of Continuity is a general mass balance that holds in all systems with no net generation of mass and with no mass transfer (e.g. Brodkey, 1988):

$$\frac{\partial \rho}{\partial t} + \nabla \cdot (\rho \vec{U}) = 0. \quad (3.1)$$

In this equation, t is the time, ρ represents the density and \vec{U} is the velocity vector.

This equation represents that the change of mass in a volume element is the difference between the mass flows into the element and the mass flows out from this volume element.

3.1.2 Conservation of Momentum

For fluid phase the conservation of momentum equation states that a small volume element moving with the fluid is accelerated because of the forces acting upon it (Bird *et al.*, 1960). The equation can be expressed as follows (Kowalczyk, 2004):

$$\rho \left[\frac{\partial \vec{U}}{\partial t} + (\vec{U} \cdot \nabla) \vec{U} \right] = -\nabla p + \nabla \cdot \tau + \rho \vec{g}. \quad (3.2)$$

The first term represents the rate of change of momentum per unit volume; the second term is the rate of momentum gained by convection per unit volume. The first term on the right hand side is the divergence of the stress tensor, which is composed of pressure and frictional stresses on the element. The last one stands for the gravitational forces. The stress term can be decomposed as

$$\hat{T} = -p\delta + \tau, \quad (3.3)$$

where δ represents the unit tensor and τ is the term containing viscous stresses. In case of a newtonian fluid the viscous stresses are related to the velocity vector as follows

$$\tau = \left(\kappa - \frac{2}{3}\mu \right) (\nabla \cdot \vec{U}) \delta + \mu (\nabla \vec{U} + (\nabla \vec{U})^T) \quad (3.4)$$

Dynamic (μ) and bulk (κ) viscosities are related with the equation of

$$\kappa = \mu' + \frac{2}{3}\mu. \quad (3.5)$$

The Stokes' hypothesis postulates a vanishing bulk viscosity and thus the second viscosity coefficient can be expressed as

$$\mu' = -\frac{2}{3}\mu. \quad (3.6)$$

Here, the term $\nabla \vec{U}$ in equation (3.4) is represented in two dimensions for simplicity.

Shear rate and strain rate in the system can also be analysed with assistance of this equation as well as with available velocity data. Shear rate can be calculated by using these partial derivatives of velocity components with the equation

$$\dot{\gamma} = \frac{\partial U_x}{\partial y} + \frac{\partial U_y}{\partial x}, \quad (3.7)$$

and the strain rate can be written as

$$\dot{\epsilon} = \frac{\partial U_x}{\partial x} + \frac{\partial U_y}{\partial y}. \quad (3.8)$$

Moreover, vorticity can be calculated with the following equation

$$\omega = \frac{\partial U_y}{\partial x} - \frac{\partial U_x}{\partial y}. \quad (3.9)$$

For the solid phase, according to classical mechanics an integral momentum balance can be introduced. Starting from this axiom stating that the rate of change of momentum is equal to the sum of the external forces acting on the body (Spurk, 1997), the following equation can be written

$$\frac{dm_s}{dt} \vec{U}_s + m_s \frac{d\vec{U}_s}{dt} = m_s \vec{g} + \int_A \vec{\sigma} dA \quad (3.10)$$

The left hand side of the equation implies the rate of change of momentum due to change of mass and acceleration. The other side of the equation consists of the gravitational forces and surface stresses which result from the liquid motion surrounding it. $\vec{\sigma}$ is the surface stress vector and \vec{n} is the normal vector. Surface stress tensor is defined as

$$\vec{\sigma} = \vec{n} \cdot \hat{T}. \quad (3.11)$$

The detailed form of the stress tensor can be seen in equations (3.3) and (3.4). The matrix representation of stress tensor consists of normal stresses and the shearing stresses as well. Deformation of the solid body is assumed as negligible during the process.

The kinematic boundary condition should be defined in existence of an interface between two materials. The interface is a surface and the unit normal to the interface is \vec{n} . Kinematic boundary condition states that the motion of the interface between liquid and solid is simply the motion of these materials themselves. There is no motion of fluids through the phase change interface and this can be represented by

$$\vec{U}_l \cdot \vec{n} = \vec{U}_s \cdot \vec{n}. \quad (3.12)$$

Consistency of the tangential vectors on the phase change interface can be expressed like that

$$\vec{U}_l \cdot \vec{t}_{l,s} = \vec{U}_s \cdot \vec{t}_{l,s} \quad (3.13)$$

where $\vec{t}_{l,s}$ are the tangential vectors laying on the boundary perpendicular to each other.

3.1.3 Conservation of Energy

From the conservation equation of total energy one can deduce the transport of thermal energy, being the most relevant because of its direct relation to temperature (Kowalczyk, 2004).

$$c_p \rho \frac{DT}{Dt} = \alpha T \frac{Dp}{Dt} + \nabla \cdot (\lambda \nabla T) + \mu \Phi + \rho \vec{g} \cdot \vec{U} \quad (3.14)$$

The equation represents the balance of thermal energy with respect to compression, heat transfer, viscous dissipation and gravitational forces, respectively, on the right hand side.

The second term on the right hand side, heat flux can be written as follows according to Fourier's law of conduction, as λ is being the thermal conductivity

$$q = -\lambda \nabla T. \quad (3.15)$$

The third term stands for viscous dissipation, μ is dynamic viscosity and the term Φ is known as the dissipation function, and its form in rectangular two dimensional coordinates is

$$\Phi = 2 \left[\left(\frac{\partial U_x}{\partial x} \right)^2 + \left(\frac{\partial U_y}{\partial y} \right)^2 \right] + \left(\frac{\partial U_y}{\partial x} + \frac{\partial U_x}{\partial y} \right)^2 - \frac{2}{3} \left(\frac{\partial U_x}{\partial x} + \frac{\partial U_y}{\partial y} \right)^2, \quad (3.16)$$

and it represents the thermal energy generated by viscous heating. The last term in the equation (3.14) is the energy gained because of gravitational forces acting on the system.

3.2 Adaptation of High Pressure Phase Change

Representation of phase transition processes under high pressure should be performed concerning both phases in the system. The basic equations that are written so far will be rewritten concerning two phases. The subscripts l and s stand for the liquid and the solid phases, respectively. The sum of percent weight (f) and volume (ξ) are used to define some properties as can be seen in following equations. The total specific enthalpy of the system is indicated as \hat{H} , and the velocity as \vec{U} (Kowalczyk, 2004).

$$f_l + f_s = 1, \quad (3.17)$$

$$\xi_l + \xi_s = 1, \quad (3.18)$$

$$\rho = \xi_l \rho_l + \xi_s \rho_s, \quad (3.19)$$

$$\vec{U} = f_l \vec{U}_l + f_s \vec{U}_s, \quad (3.20)$$

Three different possibilities are mentioned in the model used by Kowalczyk (2004). In the first case, it is assumed that the solid and liquid phases have same velocities, $\vec{U}_l = \vec{U}_s$ during the phase change. In the second case the solid velocity is assumed to be different than zero and constant, $\vec{U}_s \neq 0$. In the last case the solid velocity is taken as zero, $\vec{U}_s = 0$. In Kowalczyk's study, the third case is chosen for simplicity. In the current study, solid phase is moving with a velocity that is different than zero therefore basic equations representing the system will be given according to the second case. This cited study is the first contribution to the literature on modelling of high pressure induced phase transitions of a liquid medium, especially with the investigation of spatial and temporal temperature and velocity distributions.

Conservation equation of mass can be applied to this case just by replacing density and velocity terms in equation (3.1) as given in equations (3.19) and (3.20).

Equation for conservation of momentum should be written for the solid phase and liquid phase separately. In the model that derived by Kowalczyk (2004), the phase change mechanism is modelled with the enthalpy porosity method with some arrangements and simplifications. In this model liquid and solid phase velocities are related with porosity model. In the current study, solid phase is distinct and separated from liquid phase. Therefore,

conservation of momentum equation has the form as in equation (3.2) for liquid phase and equation (3.10) for solid phase in the system.

Equation for conservation of energy should be represented as summation of two individual phases. Equation (3.14) should be written for liquid and for solid including the source term standing for phase change as follows.

$$c_p \rho \frac{DT}{Dt} = \alpha T \frac{Dp}{Dt} + \nabla \cdot (\lambda \nabla T) + \mu \Phi + \rho \bar{g} \cdot \bar{U} - \rho \tilde{H} \frac{Df_l}{Dt} \quad (3.21)$$

\bar{U} is represented in equation (3.18). The last term should be introduced to represent the release of crystallization enthalpy. The definition of crystallization enthalpy, \tilde{H} , assuming thermal equilibrium at the solid-liquid interface is (Voller *et al.*, 1989)

$$\tilde{H} = \int_0^T (c_{p_l} - c_{p_s}) dT + L_f \quad , \quad (3.22)$$

and L_f is the latent enthalpy. f_l is the percent weight of liquid in the system. When it is 1 the only phase in the system is liquid, and when it is 0 there is only solid phase.

3.3 Dimensional Analysis of the Process

High pressure processing is affected by various internal and external parameters. The dimensional analysis of the process gives the possibility of reducing the number of those parameters and understanding the system effectively. A detailed description of the analysis for a sample scientific problem can be found in literature (e.g. Stichtlmair, 1990) and especially for this system in Kowalczyk (2004).

The characteristics of the system should be defined as geometrical and physical parameters. The characteristic length of the system is taken as the inner diameter of the high pressure cell, which is 14 mm. Characteristic time is, t_0 , the time of the process (thawing or freezing).

There are different thermofluidodynamical processes occurring during distinct phase change processes (like PAT and PST). When the phase change is induced by pressure, the flow is strongly effected by the forced convection created by pressure, as it has been shown by Pehl (2000) and Hartmann and Delgado (2002). For this case, inlet velocity is taken as the fluid velocity entering to the cell. In the second case free convection is the main mechanism and the

characteristic velocity for pure convection is defined as $U_0 = \sqrt{g \alpha_0 \Delta T L_0}$ instead of inlet velocity of fluid where ΔT is the temperature difference between the medium and surrounding. Dimensionless form of equations for mass, momentum and energy are written by introducing dimensionless variables that can be seen in Appendix C. All terms in the equations with dimensionless numbers will be given in the following section.

3.3.1 Dimensional Analysis for Pressure Induced Phase Change

This process describes pressure shift freezing/ thawing where the phase change occurs by application of pressure. Therefore, forced convection is dominated in the system. For dimensional analysis, equations (3.1), (3.2), (3.10) and (3.21) are written in dimensionless form by using previously mentioned variables. Resulted equations are given in table form with dimensionless numbers and the terms.

3.3.1.1 Dimensional Analysis of Conservation of Mass

Conservation of mass equation (3.1) is given in its dimensionless form in Table 3.1.

Table 3.1: Dimensionless form of conservation of mass

Term	Physical explanation
$\frac{\partial \rho^*}{\partial t^*}$	Rate of mass change
$\nabla \cdot (\rho^* \vec{U}^*)$	Convective mass transport

3.3.1.2 Dimensional Analysis of Momentum Equation

For momentum equation (3.2) the Reynolds and Froude numbers are introduced. The first one can be written as follows

$$\text{Re} = \frac{\rho_0 U_0 L_0}{\mu_0},$$

which shows the relation between convective momentum transfer to molecular momentum transfer. The second number has the form

$$Fr = \frac{U_0^2}{L_0 g_0},$$

and it represents the relation between convective momentum transfer to gravitational momentum transfer.

After setting the dimensionless variables in equation (3.2), dimensionless form of the equation is given in Table 3.2. The resulted form of the momentum equation for solid phase (equation 3.10) can be seen in Table 3.3.

Table 3.2: Dimensionless form of momentum equation for fluid

Term	Physical explanation
$\frac{\partial(\rho^* U^*)}{\partial t^*}$	Rate of momentum change
$\rho^* (U^* \cdot \nabla) U^*$	Convective momentum transport
$-\nabla p^*$	Pressure
$\frac{1}{Re} (\nabla \cdot \tau^*)$	Frictional stresses
$\frac{1}{Fr} \rho^* g^*$	Gravitation

$$\begin{aligned} \tau^* = & 2 \frac{\partial}{\partial x^*} \left(\mu^* \frac{\partial U_x^*}{\partial x^*} \right) + \frac{\partial}{\partial y^*} \left(\mu^* \frac{\partial U_x^*}{\partial y^*} \right) + \frac{\partial}{\partial y^*} \left(\mu^* \frac{\partial U_y^*}{\partial x^*} \right) \\ & - \frac{2}{3} \frac{\partial}{\partial x^*} \left(\mu^* \frac{\partial U_x^*}{\partial x^*} \right) - \frac{2}{3} \frac{\partial}{\partial x^*} \left(\mu^* \frac{\partial U_y^*}{\partial y^*} \right) \end{aligned}$$

Table 3.3: Dimensionless form of momentum equation for solid phase

Term	Physical explanation
$\frac{dm_s^*}{dt^*} U_s^*$	Rate of momentum change
$m_s^* \frac{dU_s^*}{dt^*}$	Convective momentum transport
$-\int_A p^* \vec{n} dA^*$	Pressure
$\frac{1}{Re} \int_A (\nabla \cdot \boldsymbol{\tau}^*) \vec{n} dA^*$	Frictional stresses
$\frac{1}{Fr} \rho^* V^* \vec{g}^*$	Gravitation

3.3.1.3 Dimensional Analysis of Energy Equation

New dimensionless numbers that will be introduced for energy equation (3.14) are Eckert, Prandtl and Stephan numbers. Eckert number is

$$Ec = \frac{U_0^2}{c_{p0} T_0},$$

which represents the relation between kinetic energy to enthalpy.

$$Pr = \frac{c_{p0} \mu_0}{\lambda_0}$$

is the ratio of momentum to thermal diffusivity. Pr and Re numbers represent together Pe number

$$Pe = Re \cdot Pr$$

Stefan number interprets the ratio of thermal specific energy to latent heat of phase change, and is

$$Ste = \frac{c_{p0} \Delta T}{L_f}$$

The given dimensionless numbers and their corresponding terms in energy equation can be found in Table 3.4.

Table 3.4: Dimensionless numbers and related terms for energy equation

Term	Physical explanation
$c_p^* \rho^* \left(\frac{\partial T^*}{\partial t^*} \right)$	Rate of temperature change
$c_p^* \rho^* (U^* \bullet \nabla T^*)$	Convective temperature change
$\alpha_0 T_0 \alpha^* T^* \left(\frac{\partial p^*}{\partial t^*} + U^* \nabla p^* \right)$	Temperature change created by pressure
$\frac{1}{Re Pr} \nabla^* \bullet (\lambda^* \nabla T^*)$	Thermal conduction
$\frac{Ec}{Re} \left\{ 2\mu^* \left((\nabla^* U^*)^2 + ((\nabla^* U^*)^T)^2 \right) - \frac{2}{3} \mu^* (\nabla^* U^*) \right\}$	Change of kinetic energy to thermal energy
$\frac{Ec}{Fr} \rho^* g^* \bullet U^*$	Gravitation
$\frac{\Theta}{Ste} \frac{\partial}{\partial t^*} (\rho^* f_i^* \tilde{H}^*)$	Temperature change caused by crystallization enthalpy
$\frac{Ec \Theta}{Ste} [U^* \nabla (\rho^* f_i^* \tilde{H}^*)]$	Convective temperature change caused by crystallization enthalpy

3.3.2 Dimensional Analysis of Temperature Induced Phase Change

This process is the process named as pressure assisted freezing/ thawing where the phase change occurs under a constant pressure by change of temperature. In this case, the dominated mechanism is free convection. The flow is caused by the density difference of water and ice as well as gravity.

Dimensionless analysis of conservation of mass for this process has the same form like the previous case as it has been given in Table 3.1.

3.3.2.1 Dimensional Analysis of Momentum Equation

Equation (3.2) is written for the present case and converted to dimensionless form. One of the newly introduced dimensionless numbers for free convection is Galileo number representing the ratio of gravitational forces to viscous forces and it can be written as follows,

$$Ga = \frac{g_0 L_0^3}{\nu^2} = \frac{Re^2}{Fr}$$

Grashof number shows the relation between buoyancy forces and viscous forces,

$$Gr = \frac{\alpha \Delta T g_0 L_0^3}{\nu^2} = Ga \alpha \Delta T$$

Archimedes number is the ratio of gravitational forces to viscous forces and is normally defined in the following form

$$Ar = \frac{Gr}{Re^2}$$

All dimensionless numbers and terms for equation (3.2) can be seen in Table 3.5.

Table 3.5: Dimensionless numbers and terms for momentum equation for free convection

Term	Physical explanation
$\rho^* \frac{\partial U^*}{\partial t^*}$	Rate of momentum change
$\rho^* (U^* \bullet \nabla^* U^*)$	Convective momentum change
$-\nabla^* p^*$	Pressure
$\frac{1}{Re} (\nabla^* \bullet \tau^*)$	Frictional stresses
$\frac{g^*}{Re^2} Ga(\alpha_0 \Delta T + \beta_0 \Delta p)$	Driving force caused by temperature and pressure change

In the last term the change of density in terms of temperature and pressure can be seen according to Boussinesq approximation.

The conservation of momentum should again be represented for solid and liquid phases separately. For solid and for liquid phases the equation systems that are given in Table 3.2 and 3.3 are applicable also for free convection case. In this case, gravitational forces are represented with the dimensionless number Ga .

3.3.2.2 Dimensional Analysis of Energy Equation

Dimensionless form of the energy equation for free convection can also be written as in Table 3.4. The only different variable is the inlet velocity and this brings a difference in the fourth term. Dimensionless number Re should be replaced with the number Gr . A new dimensionless number should also be defined which is composed of Pr and Gr numbers

$$Ra = Gr Pr$$

Rayleigh number is a dimensionless number which helps to decide the dominated type of heat transfer in the fluid, whether it is convective or conductive.

4 RESULTS AND DISCUSSION

4.1 Calibration of Liquid Crystals

As a first step of calibration, thermochromic liquid crystals (TLC) are characterized at different pressure and temperature conditions. According to the method that was explained in section 2.2.1, the color response of TLC has been analyzed in a solution of TLC in water (~ 0.1 % v/v). Figure 4.1 shows the response of TLC named BM/R-30C2W/S-40, where the temperature is given as T in °C and pressure is in MPa.

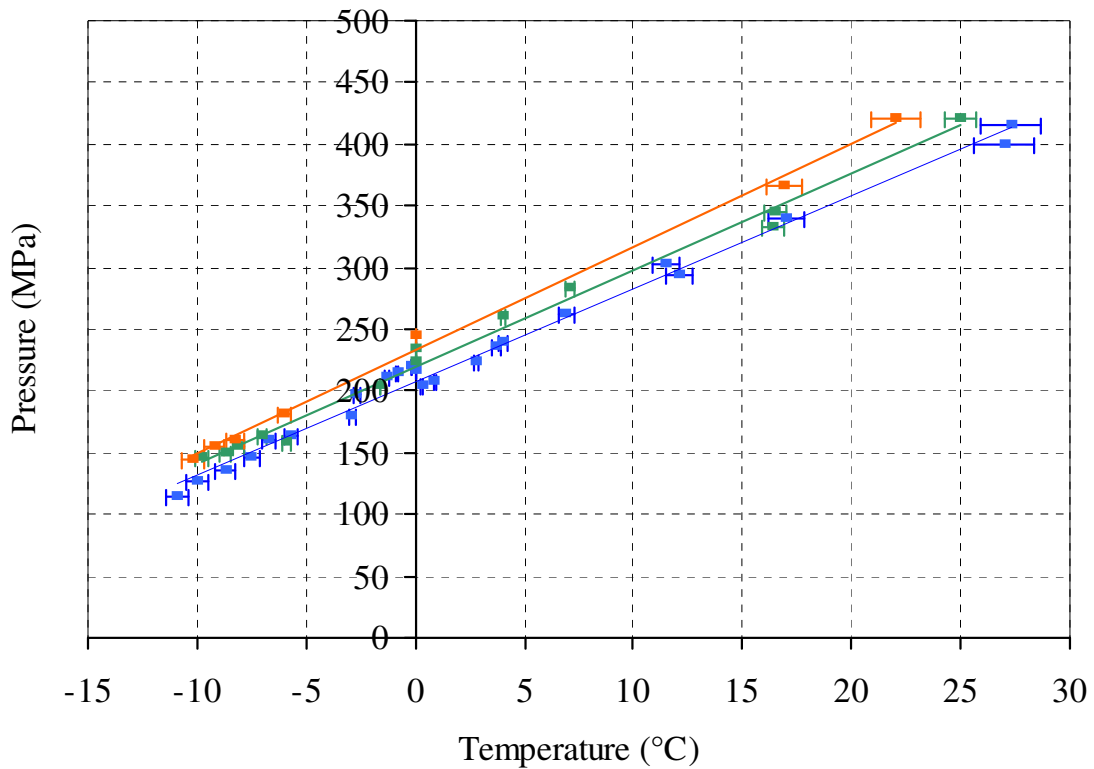


Figure 4.1: Temperature- Pressure Relation of TLC (BM/R-30C2W/S-40). R^2 values for linearity are 0.9828, 0.9675, and 0.9811 for blue, green and red, respectively.

Among the possible error sources for characterization experiments, location and sensitivity of thermocouple, local temperature deviations and uncertainties caused by eye observation should be considered. Therefore, percentage error for characterization experiments is

determined by calculating the average and standard deviation for replicated experiments, and it is represented as error bars in Figure 4.1.

The name BM/R-30C2W/S-40 contains coded information about the characteristic of the TLC, as given in section 2.2.1. It implies that this TLC has a red start temperature at $-30\text{ }^{\circ}\text{C}$ at atmospheric pressure. In the name, the bandwidth is given as $2\text{ }^{\circ}\text{C}$. This can change in practice even it is stated like that in the official name. Therefore some calibration tests are performed by the producer. Achievement of the chemical stability of TLC mixtures is extremely difficult at low temperatures. The producible bandwidth changes between $0.5\text{ }^{\circ}\text{C}$ to $1\text{ }^{\circ}\text{C}$, but it increases with decreasing start temperature. For a start temperature of $-30\text{ }^{\circ}\text{C}$, commercially available band width given as $2\text{ }^{\circ}\text{C}$ by the producer. Therefore, the required TLC is produced specifically for the requirements of the current application, with a narrower bandwidth. According to the tests done on the product, it is labeled as it has a red start temperature of $-30\text{ }^{\circ}\text{C}$, a green start temperature of $-29.53\text{ }^{\circ}\text{C}$ and a blue start temperature of $-28.72\text{ }^{\circ}\text{C}$. This red start temperature is the point where the p-T curve of TLC intersects with the x-axis at point zero.

The effect of pressure on the behavior of TLCs, as already mentioned, results in a shift of the reflected light. As can be seen in Figure 4.1, a pressure increase at a given temperature results in a red shift whereas a temperature increase at constant pressure results in a blue shift. Therefore, it can be seen that the wavelength of the reflected light show opponent changes when TLCs are subjected to temperature and pressure changes separately (Pehl *et al.*, 2000). Different types of TLCs are investigated by Pehl (2004) under high pressure. It is reported that the linear characteristics in the p-T plane can not be found for all types. In the cases of non-linearity, divergence is especially seen at high temperatures and pressures. Moreover, in linear cases, a 60% increase is observed in the band width with a pressure increase of 400 MPa. In the present study, bandwidth changes from about $2.5\text{ }^{\circ}\text{C}$ to $5\text{ }^{\circ}\text{C}$ when pressure changes from 150 MPa to 400 MPa, which correspond a change of 50%. According to Figure 4.1, it can be said that this liquid crystal is proper to use under high pressure, for the required temperature pressure range corresponding ice I-liquid phase change line of water (Figure 1).

The calibration of the TLC is performed as the next step. The pressure is kept constant and the temperature is increased with $\sim 0.2\text{ }^{\circ}\text{C}$ increments. Thermal equilibrium is waited after obtaining a homogeneous temperature field in the cell (about 30 minutes). Each obtained hue value represents a point for the specific pressure in the calibration curve, in Figure 4.2. In this

figure hue values corresponding to those homogeneous temperature fields can be seen for different pressures of 126, 135, 146, 155 and 161 MPa. Those pressures are selected according to phase change region of ice I. For temperature pressure regions of ice III and V, another TLC with different properties should be used.

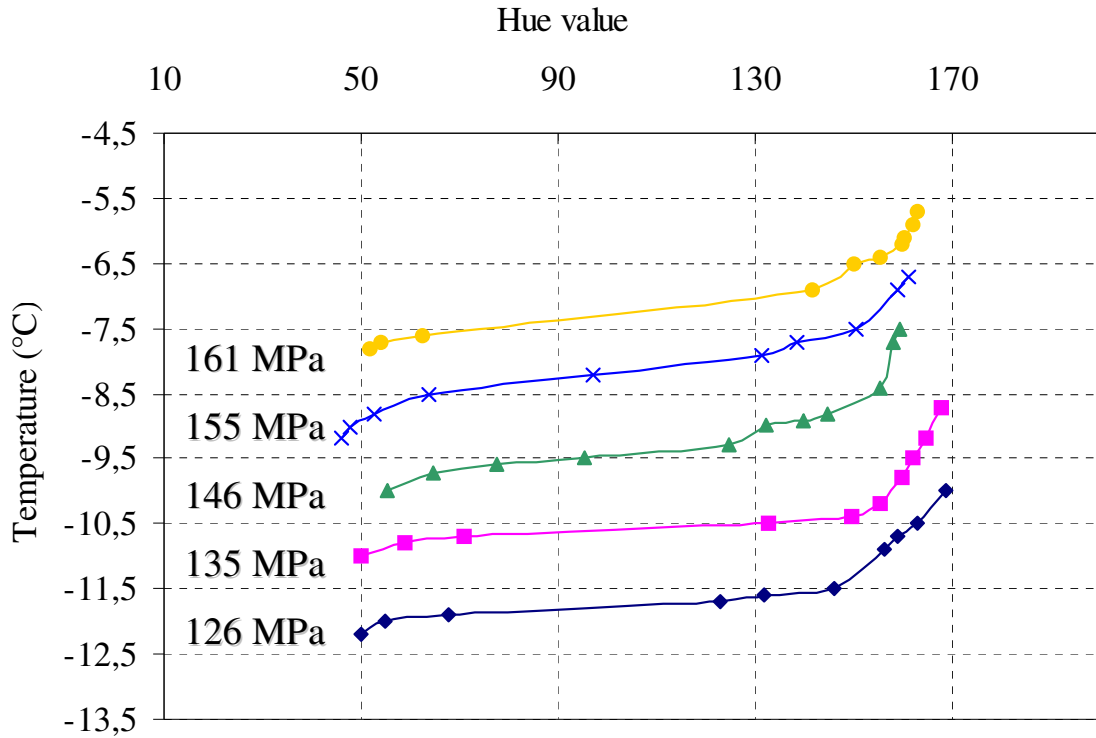


Figure 4.2: Calibration curves for BM/R-30C2W/S-40 at different pressures.

Applying quantitative liquid-crystal thermography imposes many difficulties in a specific measurement tasks. It is reported that the most important problem in this technique is its lack of reproducibility (Hollingsworth & Hay, 1998). Therefore, the authors investigate the stability of the calibration technique and state that the uncertainty in temperature depends on the quality of the liquid crystal surface, the details of the imaging equipment and the resolution of the reference temperature measurement. Concerning all these parameters, a standard estimate of error is proposed for the calibration method which uses polynomial curve fit of hue-temperature data. According to this, standard estimate of errors and percent errors can be calculated for calibration curves. In the current study splines are fitted to the original hue-temperature data and the hue-temperature curve for required pressures is created by extrapolation. The uncertainty expected for calculating T from a polynomial curve fit can be

determined by using the slope of the curve fit and standard estimate of error. A standard estimate of error is used as a descriptor of the scatter of the mean hue values about the curve fit. For the current study this uncertainty has been found having values between 3.2% and 7.3%. This means that the uncertainty has values from 3.2% to 7.3% of the temperature range for corresponding curves. It has been reported that during blue to green change ($140 < \text{hue} < 160$) there is a definite slope alteration, which is a common characteristic in all TLC applications and it can also be observed in Figure 4.2. In another study which uses TLC technique for temperature measurement reports an accuracy varying from 3% to 10% of the full color play change (Kowalewski *et al.*, 1998). Existence of pressure in the system plays an important role on properties of the system. For determination of hue and temperature values of an instantaneous temperature field, corresponding pressure value of the system is used. At every pixel of the image hue information is converted to temperature and local temperature values in an image can be determined. This TLC technology has not been utilized for the systems under high pressure yet, except the current study and Pehl *et al.*'s (1999) work where this method has been introduced first time in literature.

4.2 Dimensional Analysis

Dimensional analysis is used as a tool to simplify a problem by reducing the number of variables to its minimum number, i.e. to the number of essential parameters. Calculation of these dimensionless parameters provides a discussion about the importance of every term given in the conservation equations (see section 3.1). The estimated values for dimensionless numbers can be compared and the influence of every term can be predicted. Meaning of each dimensionless number depends on its magnitude and its algebraic linking in the corresponding term. It can be predicted that, which dimensionless number has stronger influence, or which one can even be neglected according to their order of magnitude. Parameters that are used in calculation of dimensionless parameters can be seen in Table 4.1. This reference temperature and pressure are not the initial conditions but the conditions that most often occurred for all processes. Within experimental parameters pressure is converted to nondimensional form by using those parameters and by using $\frac{P}{\rho_0 \cdot c_{p0} \cdot T_0}$. Dimensionless temperature is used as $\frac{T}{T_0}$.

Table 4.1: Physical properties of water at reference T and P (268 K, at 150 MPa)

$\rho_0 = 1066 \text{ kg/m}^3$	$\mu_0 = 0.0019 \text{ kg/m.s}$
$c_{p0} = 3780 \text{ kJ/kg.K}$	$\lambda_0 = 0.626 \text{ W/m.K}$
$L_0 = 0.014$	$\alpha_0 = 2.73 \times 10^{-4} \text{ 1/K}$

Dimensionless numbers and groups that are previously introduced in section 3.3 can be seen in Table 4.2. Comparing all values given in Table 4.2, it can be seen that the ratio of Ec to Re numbers has the smallest value having an order of magnitude of 10^{-13} . This term appears in energy equation (Table 3.4) and stands for the change of kinetic energy to thermal energy and can be neglected because of its order of magnitude compared to the other terms. The conversion of kinetic energy to thermal energy does not play an important role in energy balance of the system with low fluid velocities. The second group observed with an order of magnitude of 10^{-7} composes of Ec/Fr and 1/Ra. The Ec/Fr group stands together with the term responsible for gravitational forces (see section 3.3.1.3 and Table 3.4) and shows the ratio of energy originated from gravitational momentum to enthalpy as follows

$$\frac{Ec}{Fr} = \frac{U_0^2}{c_{p0} T_0} \frac{L_0 g_0}{U_0^2} = \frac{L_0 g_0}{c_{p0} T_0}.$$

The second factor, 1/Ra is seen with the thermal conduction term in energy equation for temperature induced phase change process (section 3.3.2.2). Ra number is the nondimensional ratio between the product of buoyancy forces and heat advection as well as the product of viscous forces and heat conduction in a fluid. Therefore it is a measure in deciding the existence of thermal convection and also a measure for thermal transport to friction effects. Ra decides the dominated type of heat transfer in the fluid and its order of magnitude shows that thermal conductivity does not have a significant importance compared to the other terms (having the order of magnitude of 10^{-3} and 10^3). A similar number is recalled for the forced convection as Pe number, which has here 10^3 as order of magnitude. In forced convection the term representing thermal conductivity (term with Pe number) has a higher order of magnitude than it has in natural convection case (term with Ra number).

Table 4.2: Estimated values for dimensionless numbers/ groups (see also section 3.3)

Dimensionless numbers/ groups	Order of Magnitude
$1/Re$	10^{-2}
$1/Fr$	10^3
$\alpha_0 T_0$	10^{-2}
$1/Pe$	10^{-3}
Ec/Re	10^{-13}
Ec/Fr	10^{-7}
Ec/ Ste	10^{-13}
Θ/ Ste	10^1
$1/Ra$	10^{-6}
$\frac{g^*}{Re^2} Ga(\alpha_0 \Delta T + \beta_0 \Delta p)$	10^1

The term $1/Re$ is in the order of 10^{-2} and is found with frictional stress terms. For both momentum and energy equation and for liquid as well as solid, frictional stresses have an important effect in the system.

The group $\alpha_0 T_0$ appears in the energy equation with the term that stands for the temperature change created by the pressurization. It has an order of magnitude of 10^{-2} which represents a significant importance in comparison with the other terms.

The terms including Stephan number (section 3.3.1.3, Table 3.4) emphasize the importance of the crystallization enthalpy. Θ/ Ste represents the direct contribution of crystallization enthalpy and has an order of magnitude of 10^1 which evidences its importance. The term with Ec/ Ste interprets the convective contribution of the same term and it can be seen that it is negligible because of its order of magnitude (10^{-13}).

The last term in Table 4.2 appears in the equation for natural convection and stands together with the term driving force caused by both temperature and pressure change. The terms α_0 and β_0 that arose from the Boussinesq approximation for density.

4.3 Results of Phase Change Experiments

In this section flow and temperature fields will be discussed during different phase change processes of ice I, ice III and ice V in the following order

- Pressure Assisted Thawing, Pressure Shift Thawing and Freezing of ice I
- Pressure Assisted Thawing of ice III
- Pressure Assisted Thawing and Pressure Shift Thawing of ice V

The process steps for the experiments can be seen once more in Figure 4.3. In this part, for experiments of ice I, liquid crystals are used as tracer particles as well as temperature indicators. Whereas for experiments concerning ice III and ice V liquid crystals can be used only as tracer particles because there is no suitable liquid crystal for the temperature pressure conditions of ice III and ice V. Therefore only flow field analyses are represented for these ice types.

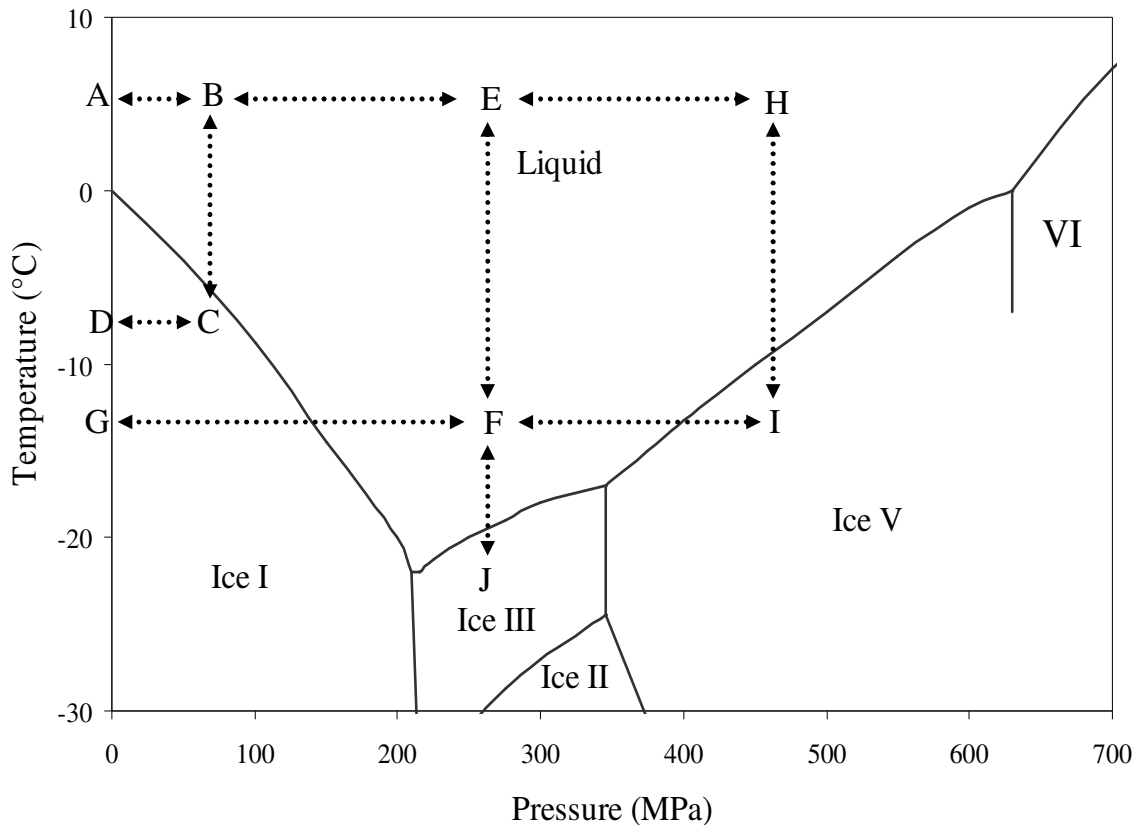


Figure 4.3: Different phase change processes under high pressure shown with phase change diagram of water.

All experiments are carried out according to the procedures explained in section 2 (Materials and Methods). There will be one sample sequence presented for processes of PAT and PST of ice I, ice III and ice V. These sample sequences are selected from the whole set of sequence results. All sequences are analyzed as performed for sample sequences. Statistical analysis of the results can be seen in Appendix D. The analyzed variables are the pressure-temperature measurement in the cell during the process and the maximum velocity values obtained from PIV calculations.

4.3.1 Pressure Assisted Thawing of Ice I

Pressure assisted thawing (PAT) experiments are performed as it is explained in Section 2.2. For the following sequence particularly, the cell is first cooled down to $-20\text{ }^{\circ}\text{C}$ ($T^* = 0.944$) and pressure is arranged to $\sim 150\text{ MPa}$ ($p^* = 0.139$). The temperature of the tempering bath is then set to $5\text{ }^{\circ}\text{C}$ and the pressure of the system is not externally controlled after temperature increase begins. When the corresponding phase change temperature is reached on the phase change diagram of water, phase change starts. In this case phase change temperature is $-13.7\text{ }^{\circ}\text{C}$ ($T^* = 0.968$) and pressure is 146 MPa ($p^* = 0.135$). The change of pressure and temperature of the cell during phase change can be seen in Figure 4.4. Here as well as in the entire work, pressure is the value measured from the pressure sensor, and the temperature is the one measured with the thermocouple inside the cell. The time zero is the point when the temperature of the cell starts to increase. Temperature of the thermal bath can serve at a rate of between $0.5\text{ }^{\circ}\text{C}/\text{min}$ to $3\text{ }^{\circ}\text{C}/\text{min}$ depending on the temperature and respectively viscosity of the cooling medium. The characteristic time of the process, $t^* = 1.00$ corresponds to 300 seconds. Temperature of the cell increases with the surrounding temperature and at 196 seconds ($t^* = 0.65$) it reaches the phase change temperature. At the same time ($t^* = 0.65$) a decrease in pressure starts as shown in Figure 4.4 (a). The latent enthalpy required for phase change is supplied by the increasing surrounding temperature. As thawing occurs, pressure in the system decreases about 25 MPa ($p^* = 0.046$) due to the higher density of the liquid state as compared to ice I. Thawing takes place under pressure in a similar way as at atmospheric pressure, i.e. ruled by thermal gradients between the sample and the surrounding fluid. But phase transition does not occur under constant pressure, a pressure decrease is observed due to volume decrease associated with liquid transition to ice I. This pressure decrease is given as 50 MPa for 590 ml Tylose sample (Denys, 2000). In literature, for cylindrical potato samples

in a high pressure chamber, it was reported that thawing process is accompanied by a pressure decrease of about 30 MPa (Schlüter, 2004).

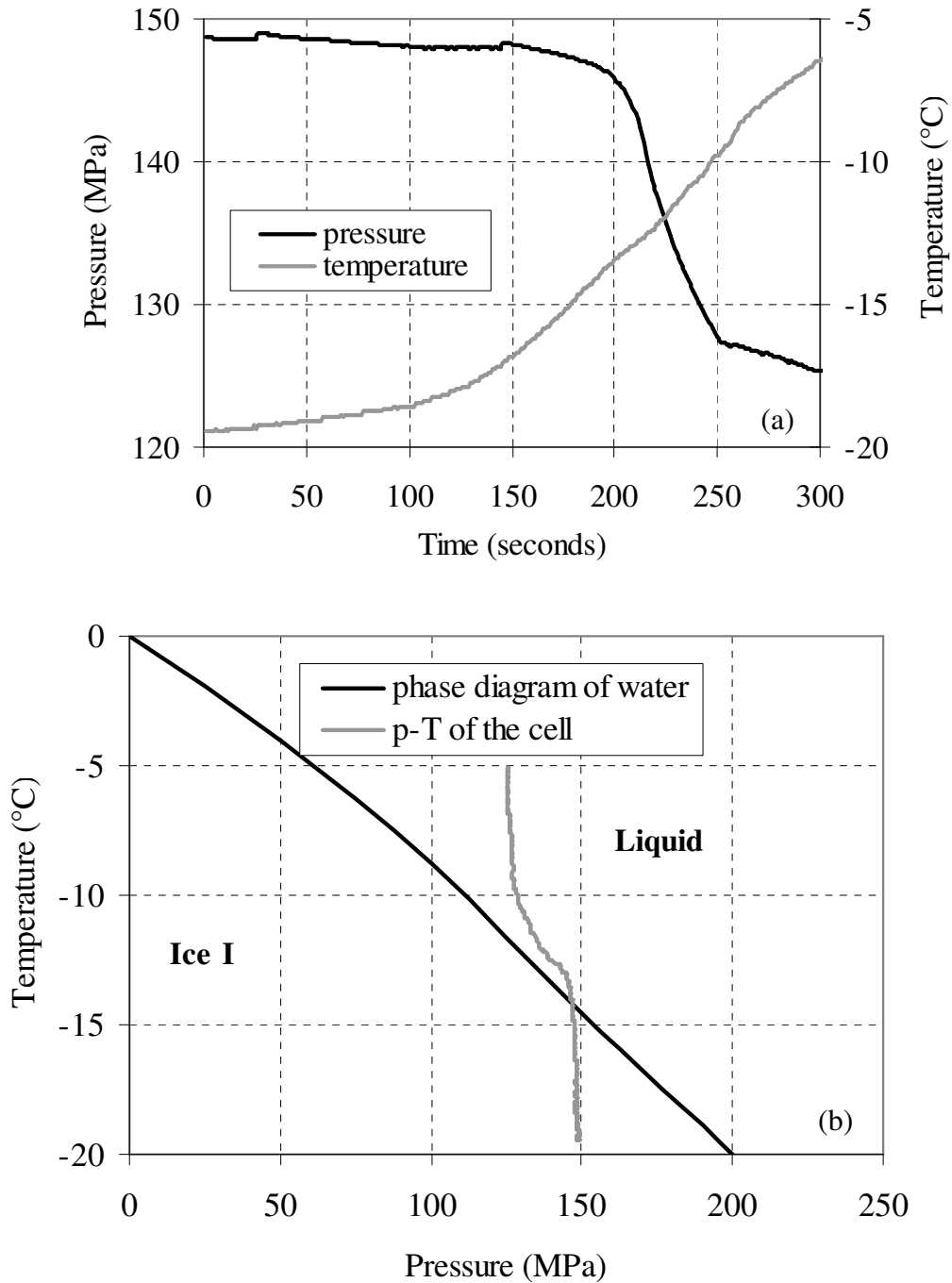


Figure 4.4: Pressure-temperature change measured in the cell during PAT of ice I (a) given respect to time (b) given with the phase change diagram of water.

For high pressure thawing of foods with high water content, the reduction of the thawing time is mainly related to the reduction of the phase change temperature which allows a high heat flux rate during phase change. In addition, the reduction of the latent heat of water with increasing pressure reduces the energy involved in the phase change during thawing under high pressure (Chevalier *et al.*, 1999).

Temperature-pressure relation of the system is given during the physically observed phase change in the cell, which begins with the observation of the ice motion in the cell and ends with the conversion of the whole volume of ice into water.

In the following paragraphs, the instantaneous velocity and temperature profiles are discussed. In Figure 4.5 images corresponding to the mentioned phase change process can be found. Images are presented with their time in the whole sequence of analyzed images. The time of the first image in Figure 4.5 is around at 210 seconds ($t^* = 0.70$) in Figure 4.4 (a). The whole phase change takes place about 300 seconds and the analyzed images, where the motion of ice is observed, belong to last 110 seconds of the sequence.

In these figures, solid phase can be differentiated from the liquid phase on the upper half of the cell. The upward motion of the ice can be observed through the images. Since the temperature on the walls is higher than the measured temperature in the cell, thawing starts from the walls. Ice body detaches itself from the bottom and the window of the cell and moves up since it has a lower density than water. From the curvature analysis it is measured that the moving solid body has a curvature radius of 5.5 mm, while the visible part of the window in figures has 3 mm radius. It is known from the geometry of the cell that the inner cell wall has a curvature of radius of 7 mm. Therefore, it can be stated that the ice disassociates from the lower surface of the cell.

All images belonging to the sequence are analyzed by using PIV after image enhancement methods that are explained in section 2.2.2 and the results can be found in Figure 4.6. PIV analysis is carried out for consecutive images for the entire sequence. Here, only the corresponding figures for Figure 4.5 are presented.

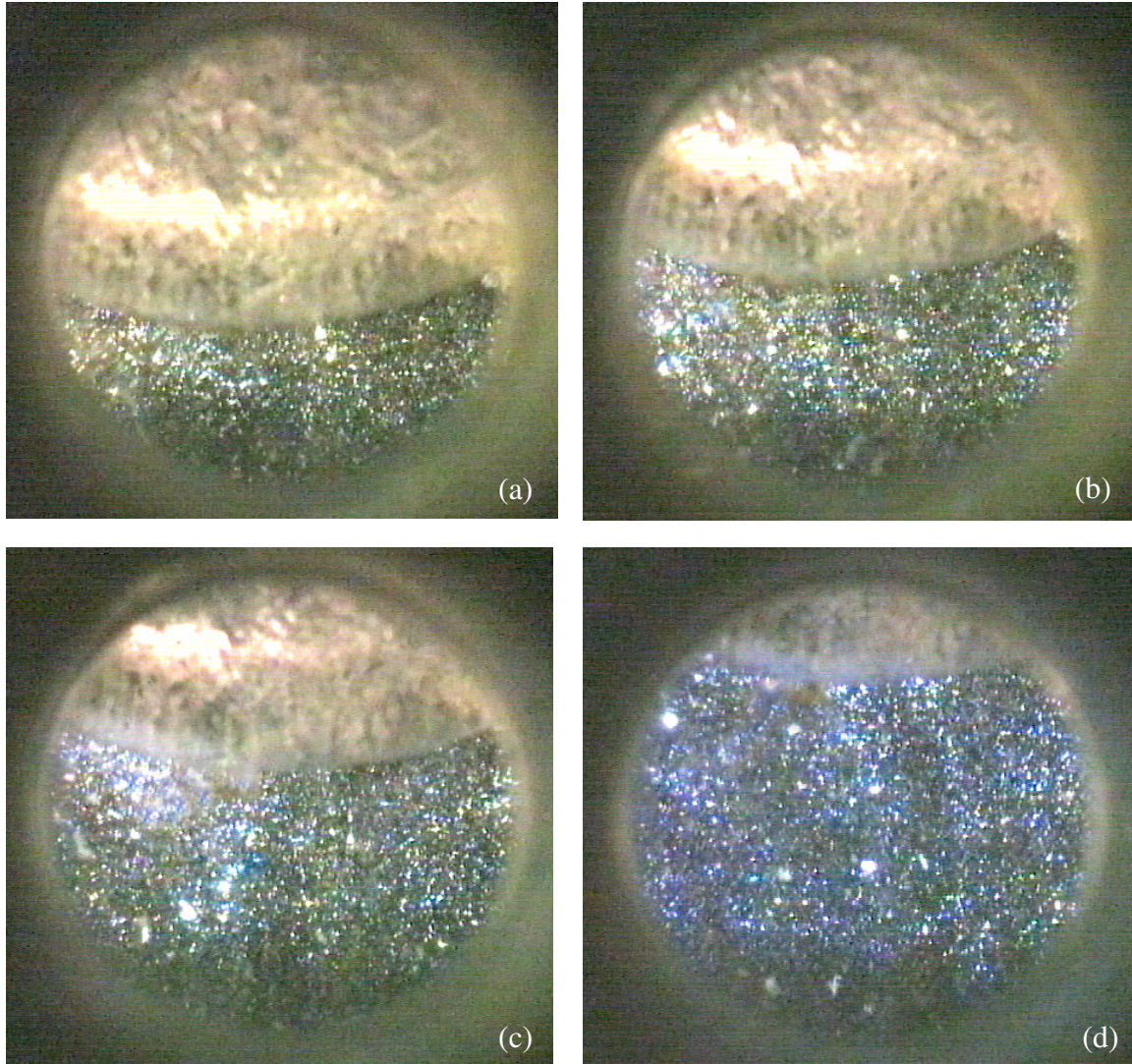


Figure 4.5: Instantaneous images from PAT of ice I at different times (a) $t^* = 0.70$, (b) $t^* = 0.73$, (c) $t^* = 0.78$, and (d) $t^* = 0.85$.

In Figure 4.6 the solid part is depicted with the gray half circle and the motion of ice can be differentiated also from the distribution of the velocity vectors. The velocity vectors outside of the observation area (on the corners) are erroneous vectors resulted from PIV (for all velocity fields represented in this work). Ice moves as solid body with a spatially constant velocity of 0.40 mm/s ($v^* = 0.07$) where the characteristic velocity for PAT is calculated as 6.12 mm/s ($v^* = 1.00$). The motion of ice is firstly caused by the pressure difference introduced to cell with beginning of thawing because of the density difference between water and ice I. Secondly, the water formed in the cell locates itself at the bottom because of its higher density. On the solid-liquid interface (the lower line of the gray area) solid creates such

a boundary condition that the flow is here separated and fluid flows along this interface and y component of fluid velocity takes almost zero value. The motion of ice starts to form vortex as can be seen in Figure 4.6 (a), in the region depicted with 2. In this region, the fluid velocity reaches a maximum of 1 mm/s ($v^* = 0.16$). Point 1 can be differentiated with its low velocity compared to the whole fluid region, having a 90% reduced velocity value compared to near surrounding area. If the motion of point 1 is observed in all images in Figure 4.6, it can be said that there is a stagnation point flow dominated around this point.

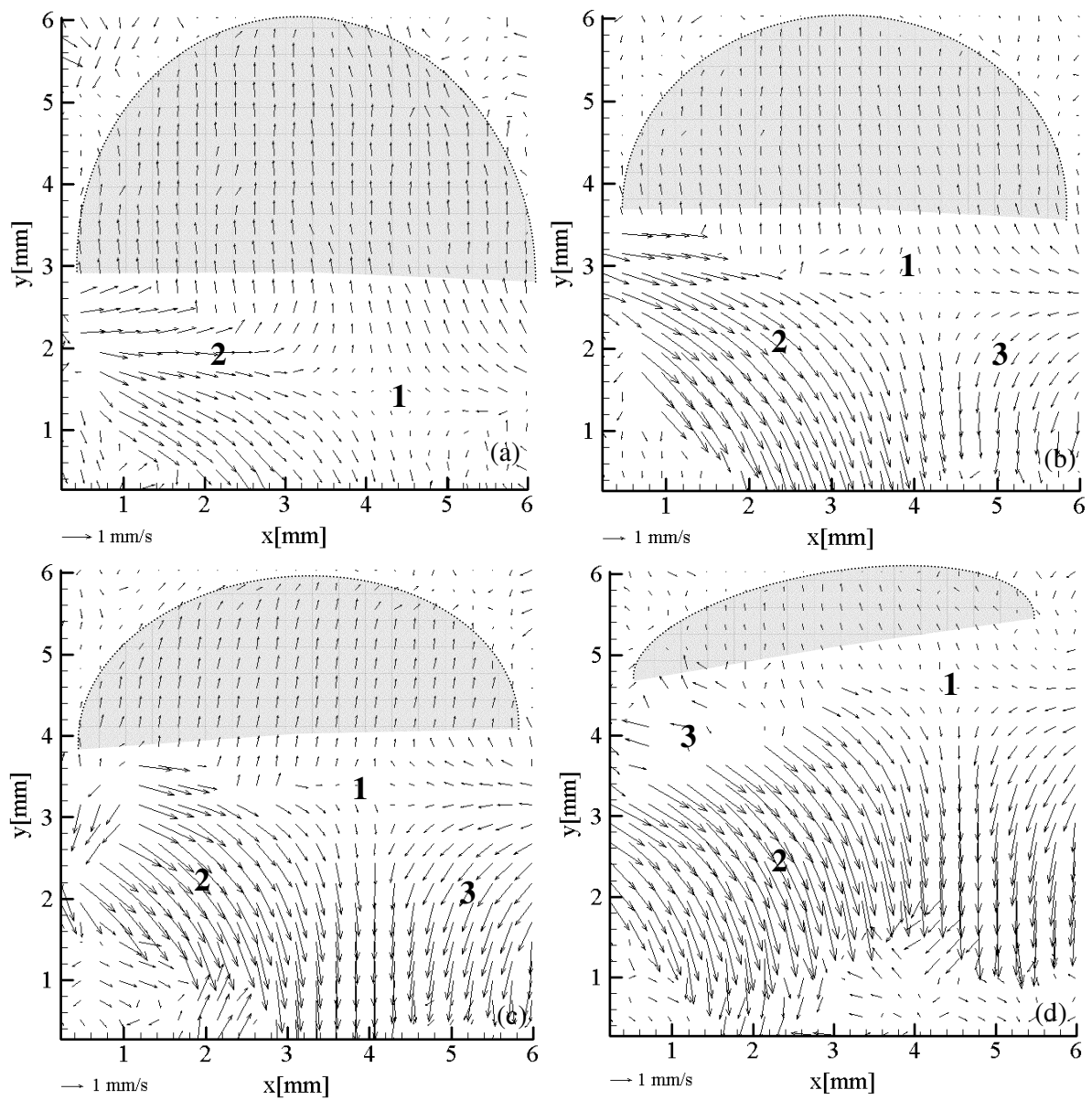


Figure 4.6: PIV results of images during PAT of ice I (corresponding to Figure 4.5)

In Figure 4.6 (b) more developed vortex can be seen. At point 1 velocity is again 10% of the surrounding fluid velocity. The flow in the cell is not symmetrical because of the geometry of the cell. As can be seen in Appendix B from the cell construction, the fluid inlet is located at the bottom on the right side of the cell. Thawing of ice results in a volume as well as a pressure decrease in the cell. The volume change in this inlet is occupied with the coming water which has been just thawed. And this induces the asymmetrical direction of the flow. In the regions 2 and 3 in Figure 4.6 (b), the fluid velocity has a maximum value of 2 mm/s ($v^* = 0.33$) and 1 mm/s ($v^* = 0.16$), respectively.

In Figure 4.6 (c) similar flow characteristics can be observed. Increasing fluid volume in the cell accelerates the flow in the liquid region. Ice velocity changes slightly and becomes 0.5 mm/s ($v^* = 0.08$). The average velocity of the fluid takes a maximum of 2.2 mm/s ($v^* = 0.36$) in region 2. Relatively high values are observed in near wall area of region 2. As long as ice thaws and turns into water, liquid phase moves along the cell wall because of its density difference and this amount of water may cause the fluid to accelerate in near wall region. In the upper left of region 2 a disturbance can be visualized in the velocity field where possibly velocity values are significantly higher. The same effect can also be seen in the lower part of region 2.

In Figure 4.6 (d) the disturbed velocity field is observed in the upper part of region 3 and the bottom of the cell. In regions 2 and 3 maximum fluid velocities have values of 2.3 mm/s ($v^* = 0.38$). At point 1 a velocity of 0.15 mm/s ($v^* = 0.02$) is observed where the surrounding fluid has 1 mm/s ($v^* = 0.16$) velocity on average. On the interface of vortices a layer can be noticed with an extensional flow characteristic (right side of point 2).

Although phase change of water is subject of many studies, there is no experimental study concerning spatial velocity and temperature distributions of the process under high pressure. The only contribution is Kowalczyk *et al.* (2004)'s study that concerns about the numerical simulation of phase change processes under high pressure. In one of the recent studies PIV is used to measure laminar natural convection resulting from buoyancy attendant on the freezing of water in small rectangular cavity under normal conditions (Seybert, 2005). The measured velocities have the value of 1 mm/s for the study and velocity values of the current work have also the same order of magnitude. Another study uses also PIV and thermometry for two-phase flow problems, where the phases are ice and water, under atmospheric pressure

(Kowalewski, 1998), in this study the velocity values change between 0.4 to 4 mm/s, during freezing of water.

Accuracy of the PIV method is improved by use of additional filters and error correction vectors as explained in section 2.2.3. For the PIV program that is used in this study after application of CDIC method with image and error correction, the maximum error is reported as 5% in Wereley & Gui's study (2003) for the particle size of 1.5 pixels which is also the case in the current study.

Instantaneous digitalized temperature fields of the given sequence can be seen in Figure 4.7. Digitalization is performed as it is explained in section 2.2.2. For each instantaneous image, the corresponding pressure value is used to calculate the temperature value from the hue information of every pixel. In Figure 4.7 for different moments the ice motion can be observed with the white area in the upper half of the cell. Other white areas and points caused by the pixels that have extreme hue values. Those regions may be caused by the liquid crystals that are still orienting their layers and those regions are observed as bright spots on the images in Figure 4.5. Hue values of these spots do not lay in the range of calibrated hue values therefore these points can not be calculated.

Figure 4.7 (a) corresponds to the 210th second ($t^* = 0.70$) of the process which is given in Figure 4.4 (a). The thermocouple which is located at the top lid of the cell shows a temperature of $-12.87\text{ }^{\circ}\text{C}$ ($T^* = 0.971$) at this moment. Location of the thermocouple prevents measuring local temperature values in the cell. The temperature information from liquid crystals shows that temperature in the cell for Figure 4.7 (a) changes between $-11.9\text{ }^{\circ}\text{C}$ ($T^* = 0.974$) to $-13\text{ }^{\circ}\text{C}$ ($T^* = 0.970$), having also some positions with temperatures of $-11.3\text{ }^{\circ}\text{C}$ ($T^* = 0.976$). As thawing proceeds and ice melts in the cell, temperature starts to increase and takes values between $-11.2\text{ }^{\circ}\text{C}$ ($T^* = 0.977$) to $-12.5\text{ }^{\circ}\text{C}$ ($T^* = 0.972$) as can be seen in Figure 4.7 (b). 15 seconds later, in Figure 4.7 (c) temperature range stays almost unchanged but the area of warmer regions ($-10.8\text{ }^{\circ}\text{C}$ to $-11.6\text{ }^{\circ}\text{C}$) ($T^* 0.978$ to 0.975) comparatively increases. In the last figure, at around $t^* = 0.85$, temperature of the cell changes mainly between $-10.2\text{ }^{\circ}\text{C}$ ($T^* = 0.981$) and $-11.1\text{ }^{\circ}\text{C}$ ($T^* = 0.977$). In the whole sequence local temperature differences reach to approximately $1\text{ }^{\circ}\text{C}$ ($T^* = 1.022$).

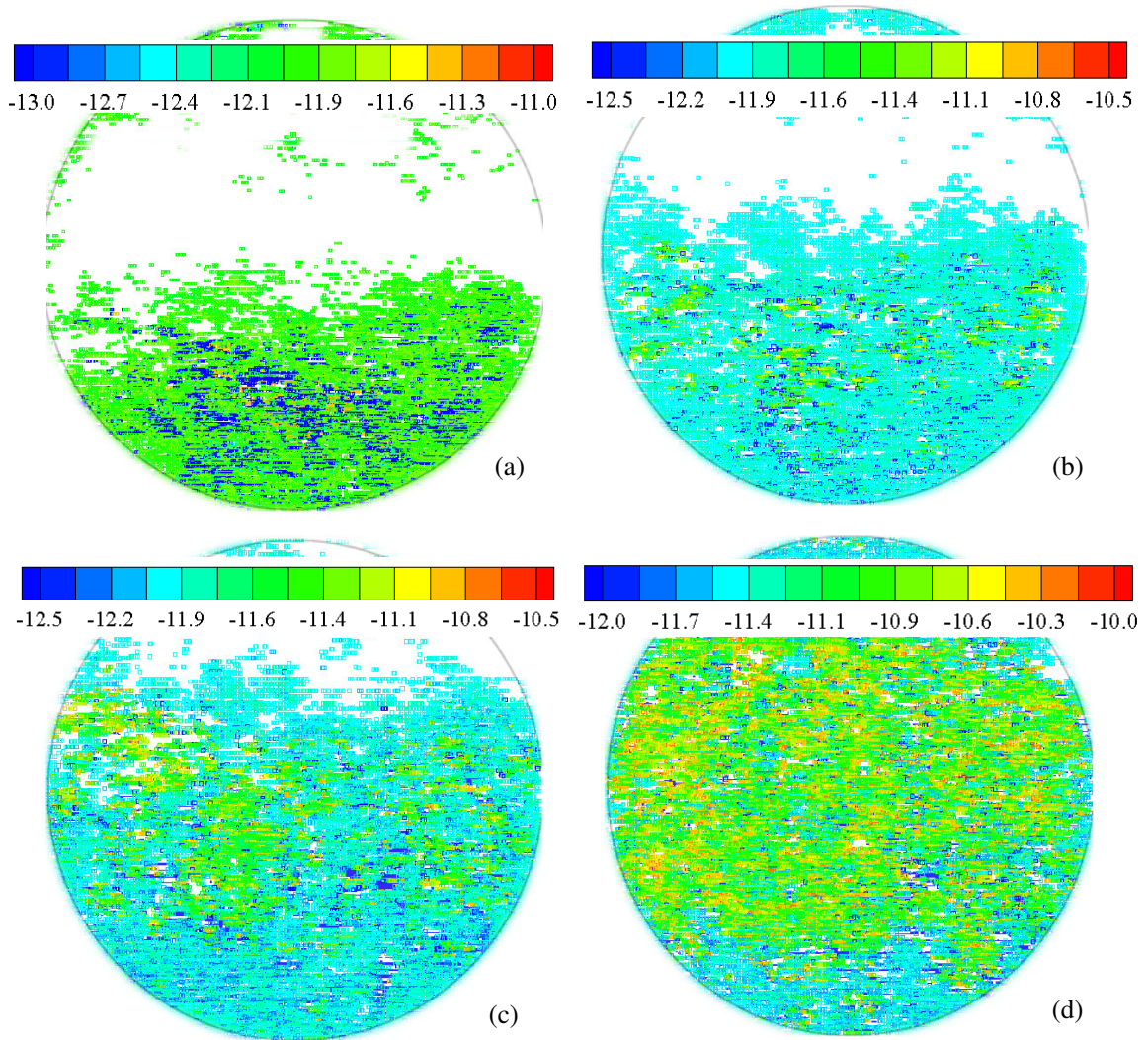


Figure 4.7: Instantaneous digitalized temperature field results (in °C) of images during PAT of ice I (corresponding to Figure 4.5)

Pressure assisted thawing process can be represented with the equations that are discussed in section 3.3.2, where momentum equation can be seen in Table 3.5 and energy equation can be seen in section 3.3.2.2. For PAT, Ra is 5.3×10^4 , Gr is 4.6×10^3 , Pr is 11.5, Ga is 8.5×10^6 , Ar is 3.3×10^1 and Ste is 0.053. The last group, Ga $(\alpha_0 \Delta T + \beta_0 \Delta p) / Re^2$, has a value of 4. As characteristic velocity $\sqrt{g \alpha_0 \Delta T L_0}$ is used which is the velocity caused by the temperature difference in the system. The value of Ar number implies that gravitational forces have more significant effect on momentum transport than the viscous forces. Moreover, Ga and Gr numbers also show the importance of gravitational forces in the process.

The momentum equations (Table 3.2 and 3.3) for the system are composed of the rate of momentum change, the convective momentum change, pressure term, frictional stresses and

the driving force brought by temperature and pressure effect on density. Frictional stresses are represented with $1/Re$, which is 2×10^{-2} and gravitational forces can be seen with $1/Fr$, which is 6.1×10^4 . As their values imply, frictional stresses do not play an important role in momentum transport as the gravitation plays.

The energy equation for PAT is similar the equations that are represented in Table 3.4. The main contribution is introduced by the rate of temperature change and the convective temperature change. The temperature change caused by the pressure appears with a constant of $\alpha_0 T_0$ having value of 6.7×10^{-2} . The thermal conduction term has a constant of $1/Gr.Pr$ (or $1/Ra$) that is calculated as 1.8×10^{-5} . The contribution of the term with $\alpha_0 T_0$ is more significant than the contribution of thermal conduction, as it has a higher order of magnitude. The change of kinetic energy to thermal energy is found to have a constant of 7.7×10^{-13} (Ec/Re) and has negligible effect on energy change of the system. The term contribution of gravitation to energy can be seen with a constant of 1.4×10^{-7} . The term having Θ/Ste represents the energy brought by crystallization enthalpy and the constant has a value of 12. Whereas the same term which arose from convection, having constant of 6.8×10^{-10} , evinces the negligibility of the convective contribution of crystallization enthalpy in the system. In conclusion, it can be stated that except the change of kinetic energy to thermal energy and the convective contribution by crystallization enthalpy all other terms should be considered for conservation of energy of the process.

When the term $\nabla \bar{U}$ is analyzed in detail, it allows investigating some parameters that can lighten fluid-mechanical characteristics of the system. As it has been given in equations (3.7), (3.8), (3.9) and (3.16), sequentially, shear rate, strain rate, vorticity and dissipation are calculated by using 2D velocity field results. For the whole sequence shear-rate takes values between -2×10^{-3} 1/s to 3×10^{-3} 1/s ($\dot{\gamma}^* = -0.60$ to 0.9). In the following figure (Figure 4.8) shear-rate contours can be seen with velocity fields that are depicted in Figure 4.6. In Figure 4.8, contours of only first and the last images are given. As can be seen from the first image, shear-rate has minimum values on the solid-liquid interface, where velocities are extremely small. The highest values are observed in the region of high velocity in the second image. For strain-rate a contrary behavior is observed; the high velocity areas have the minimum strain-rate values, and the low ones have maximum. In Figure 4.9 strain-rate contour can be seen for the last image, where difference concerning strain-rate values.

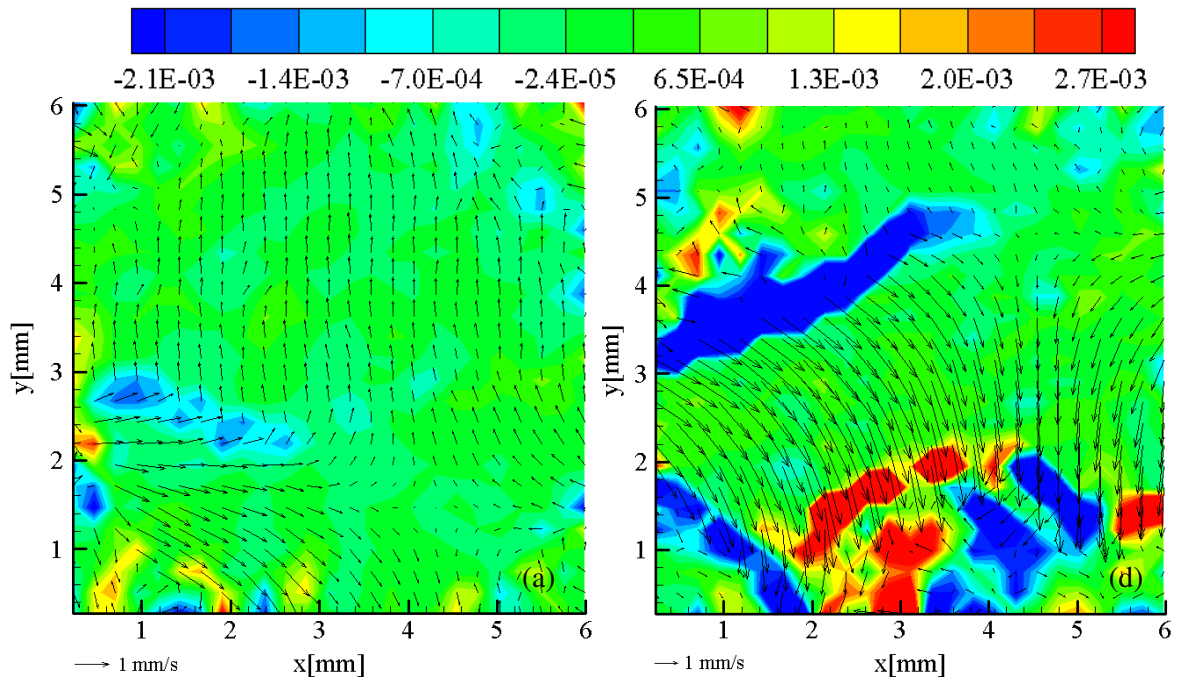


Figure 4.8: Shear-rate (in 1/s) contour plot for image (a) and (d) of PAT of ice I (corresponding to Figure 4.6)

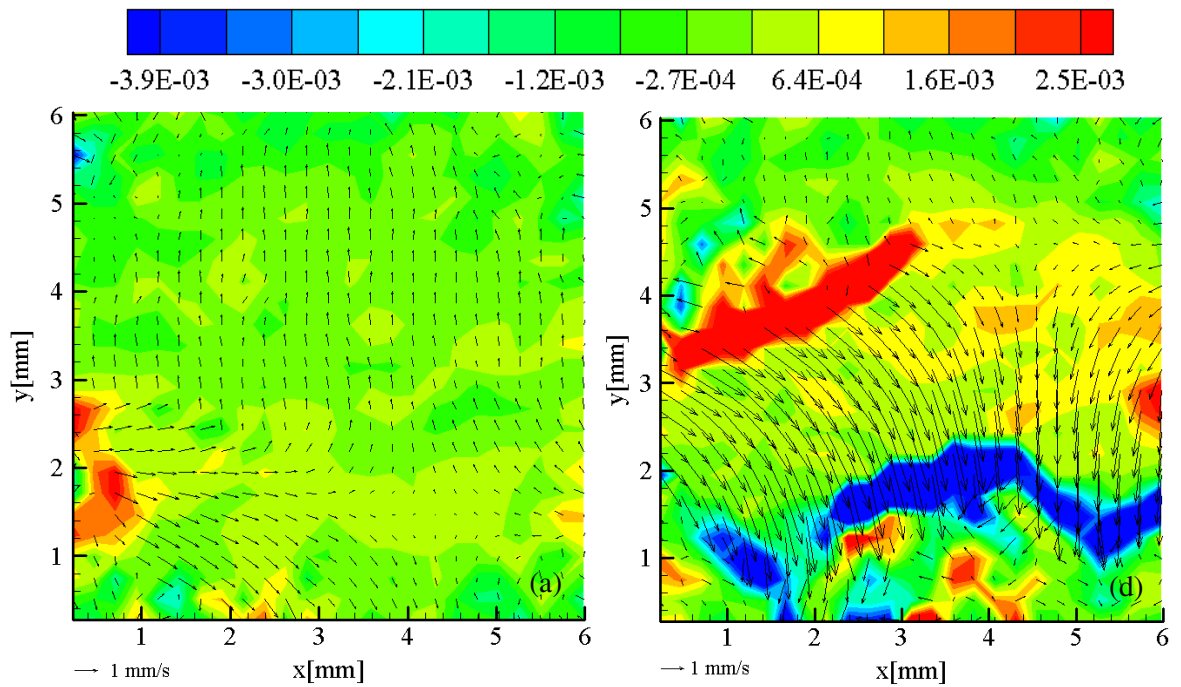


Figure 4.9: Strain-rate (in 1/s) contour plot for image (a) and (d) of PAT of ice I (corresponding to Figure 4.6)

At the beginning of the process strain-rate distribution is quite homogeneous. As process continues high strain-rate regions are observed again at solid-liquid interface as well as upper part of the cell where there are relatively high velocity vectors. Strain rate changes between -3.9×10^{-3} 1/s to 2.5×10^{-3} 1/s ($\dot{\epsilon}^* = -1.17$ to 0.75). Since negative strain rates correspond to compressive strain and positive rates to tensile strain, an observable compressive force exists in Figure 4.9 (d) in the region that is seen as blue. Moreover in the same image, the region observed with red represents the existence of tensile forces in this region.

Vorticity has a range from -8.6×10^{-3} 1/s to 7.3×10^{-3} 1/s ($\omega^* = -2.58$ to 2.19) during the whole process. It does not show any significant change at the beginning of the process. Near the end of sequence its value reaches its maximum in region 3 (in Figure 4.6 d). It has its minimum where the x-component of the velocity is almost zero, the region 2 in the aforesaid figure.

Viscous dissipation appears in conservation of energy equation (see equation 3.12 and Table 3.4) together with the dimensionless group of Ec/Re . The magnitude of this group, 10^{-13} , shows that this contribution to energy is negligible. Nevertheless as it shows the energy contribution to the system created by viscous forces in the fluid, its distribution through out the process as well as at different locations in the cell should be analyzed. For the current system dissipation has values from 1.1×10^{-6} 1/s² to 1.7×10^{-5} 1/s² ($\Phi^* = 0.10$ to 1.53). Figure 4.10 shows dissipation contours from PAT process at different times. The amount of energy which is obtained through dissipation may not be significant when it's compared to the total energy created in the system, but when biological systems are under consideration this negligible amount might eventually affect reaction dynamics as well as biochemical properties and the structure of the system. Whether this small amount of thermal energy can have a significant impact or not remains as subject of future studies.

On the effects of fluid- and thermo-dynamical properties on biological systems, studies carried on the culture of animal cells can be given as an example (van der Pol *et al.*, 1998). Laminar and turbulent flow conditions have been used to study the shear sensitivity of animal cells in various small scale systems. It has been concluded that the shear-induced death of animal cells is related to a range of parameters including shear stress, shear time, power dissipation etc. In general, sublethal cell damage or cell deaths are found to start in the range of shear stresses from 0.5 - 200 N/m². Other parameters that correlated with the disruption of animal cells caused by shear induced viscosity, surface tension, the length of the smallest turbulent eddy and generation of vortex. Turbulent eddies that are smaller than or even the

same size as the cell can be damaging. However the difficulty is to decide whether the different small scale devices used for shear research represent the correct down-scaling of the real systems.

The available information on animal cells can give an idea about the plant tissues as well, as they are being more sensitive to external changes due to their cell structure. Shear stress values for high pressure experiments of this study stays considerably small, having an order of magnitude of 10^{-5} , which is calculated by using the viscosity of water at 150 MPa ($p^* = 0.139$ and $T^* = 0.981$) and -10 °C. Of course for high pressure processing, additionally the effect of high pressure has a critical importance causing some structural and functional changes on biological cells. Pressure acting on cells induces shear stress in the cell wall and this shear stress is more harmful to cell than the flow induced shear stress on the surface (Hartmann & Delgado, 2003). Therefore, all those parameters should be taken into consideration in determining process conditions for the specific samples.

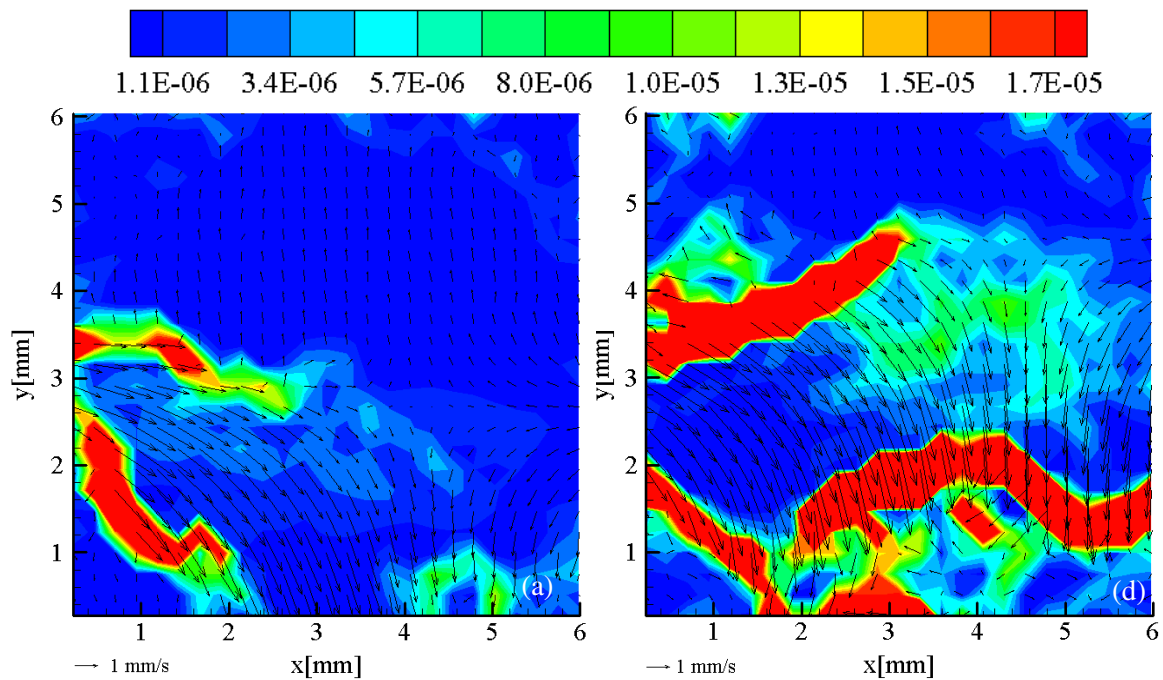


Figure 4.10: Dissipation (in $1/s^2$) contour plot for image (b) and (d) of PAT of ice I (corresponding to Figure 4.6)

4.3.2 Pressure Shift Thawing of Ice I

Pressure shift thawing (PST) experiments are carried out according to the procedure that is given in Section 2.2. In this section instantaneous temperature and velocity field results will be discussed in detail. Specifically for this experiment the temperature of the tempering bath is set to -6 °C. The initial temperature in the cell is -5.96 °C ($T^* = 0.996$) and the pressure is arranged to 50 MPa ($p^* = 0.046$). Then pressure is increased to achieve phase transition by crossing the phase change line. Pressure is increased till the entire volume of ice changes into water in the cell. Temperature-pressure in the cell during the process and its representation together with the phase change diagram of water can be seen in Figure 4.11.

Pressure increase rate corresponds 15 MPa/s for water at 20 °C. The same pressure increase rate creates a 0.7 to 2 MPa per second increase when there is ice I in the cell. The rate increases as process develops and reaches approx. 2 MPa/s during the motion of ice. It is observed that pressure increase causes the sample temperature to decrease in all of the evaluated sequences. The temperature declines until a minimum of -9.86 °C ($T^* = 0.982$). This temperature decrease upon pressurizing can be attributed to the absorption of the latent heat required for the melting process and the inability to supply simultaneously this amount of heat. A similar behavior in the temperature is also observed in literature (Denys *et al.*, 1997; Schlüter, 2004). In the first study (Denys *et al.*, 1997) it is reported a temperature decrease of almost 15 °C for 590 ml of Tylose and for a pressure increase of 200 MPa. Schlüter (2004) reported a decrease of 10 °C in temperature corresponding to a pressure increase of about 200 MPa for cylindrically shaped potato samples. Since the studies about high pressure thawing are rather scarce it is difficult to make direct comparison with literature. Moreover, most of the studies are dealing with quality attributes of thawed products not with the way, in which the thawing process is carried out.

The total time required for the phase change is 60 seconds ($t^* = 1.00$). The process time starts by pressure increase at time $t^* = 0$ and ends when the pressure is stopped, i.e. when the phase change is completed in the whole volume of the cell. The part of the analyzed sequence corresponds to the motion of ice which takes about 10 seconds ($t^* = 0.17$) for PST and instantaneous images from the sequence can be seen in Figure 4.12. The time of the images will be given in seconds with respect to time scale in Figure 4.11(a).

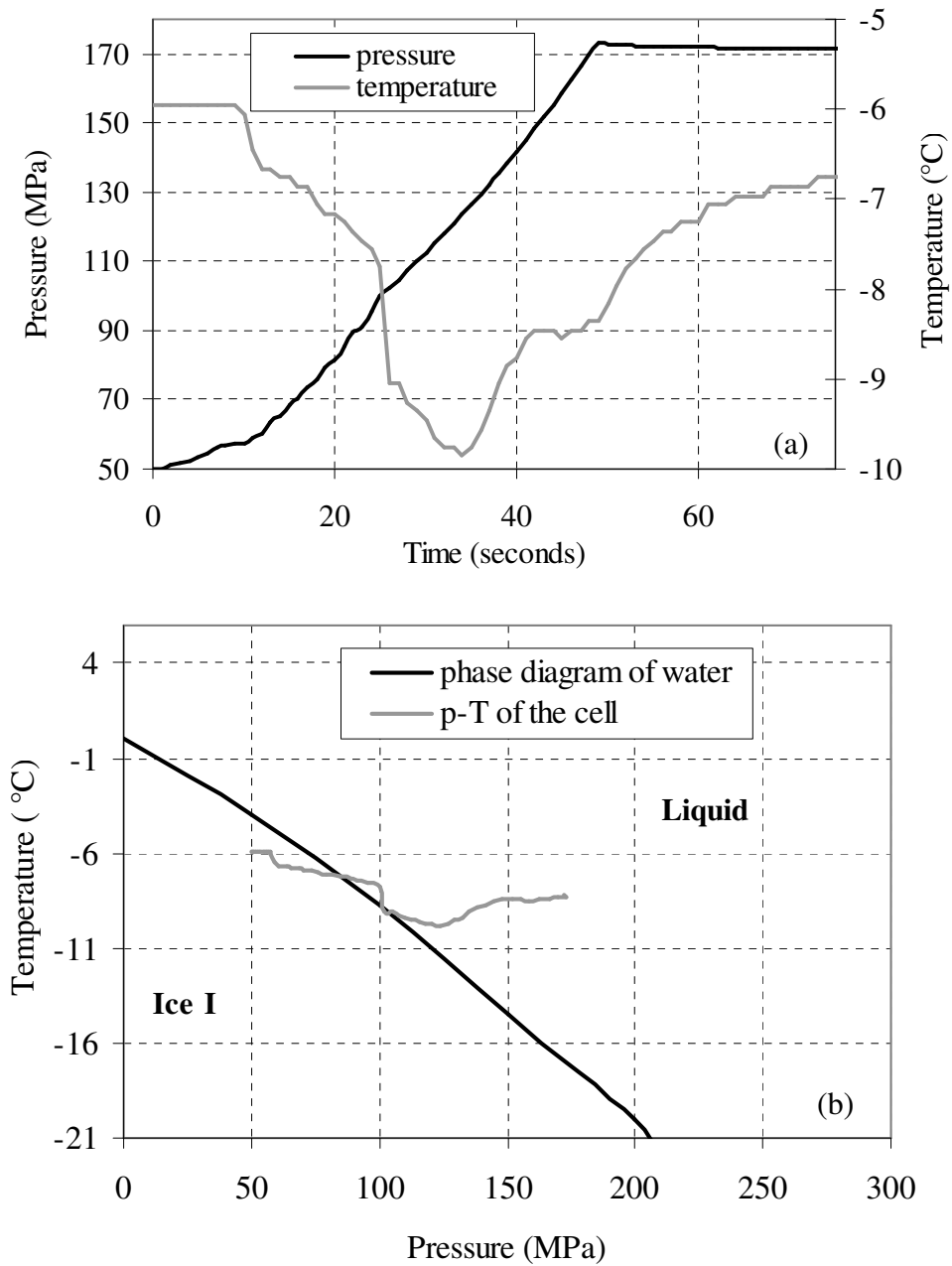


Figure 4.11: Pressure-temperature change measured in the cell during PST of ice I (a) given respect to time (b) given with the phase change diagram of water.

It is possible to control the process time by arranging the pressure increase rate. For visibility of the process and to obtain suitable time interval between images experiments are carried out with this pressure rate. The process time for PAT around 300 seconds, because of the lack of forced convection that is brought to the process by pressure.

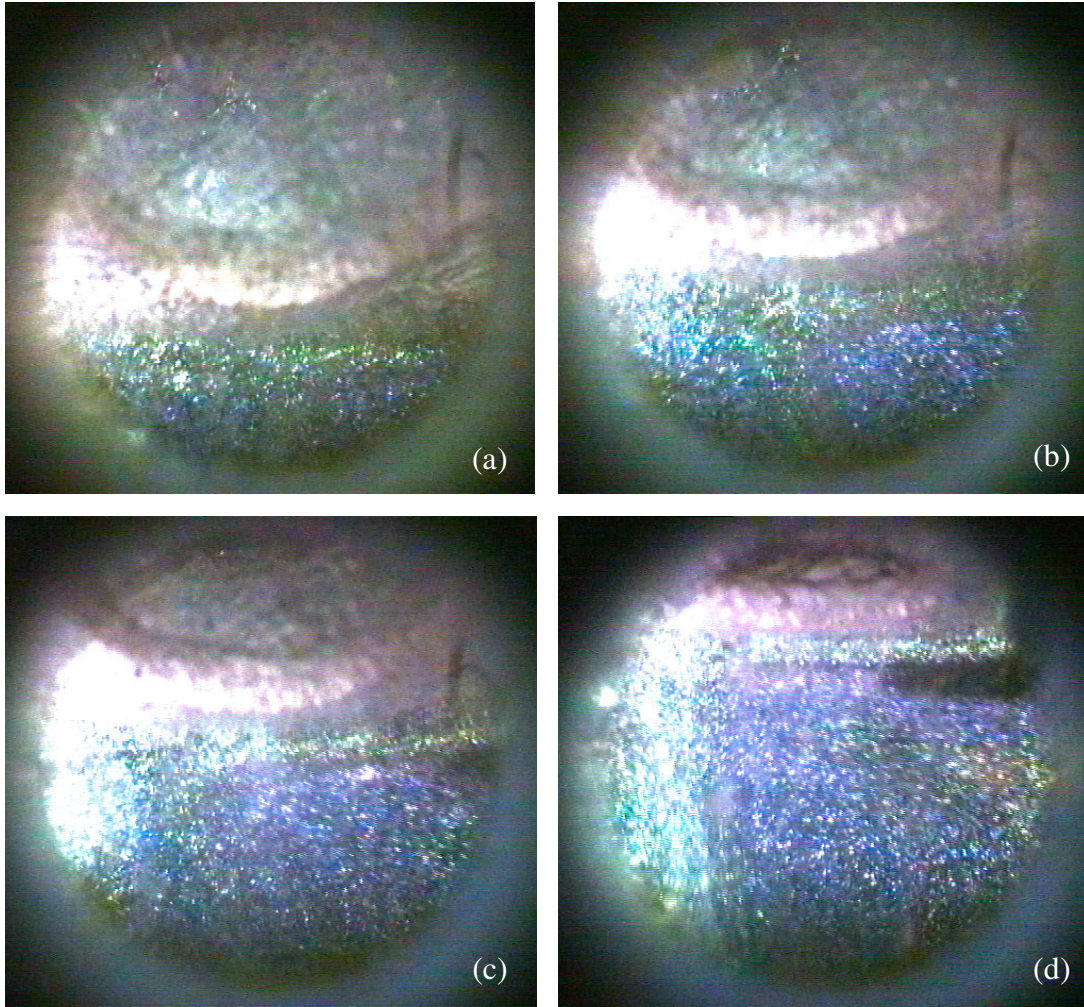


Figure 4.12: Images from PST of ice I at different times. (a) $t^* = 0.65$ (b) $t^* = 0.68$ (c) $t^* = 0.72$ and (d) $t^* = 0.75$.

The thawing in the cell is first observed by a motion in the centre. The diffuse transparency of the front ice layer and the reflected light from liquid crystals make it possible to observe the motion behind the ice layer at the beginning of the thawing. This motion shows that thawing starts in the central region of the cell. Approximately 20 seconds ($t^* = 0.33$) after the start of pressure increase, the first motion behind the ice layer is observed. The ice layer detaches itself from the surfaces of the walls and window, and starts to move upwards at around $t^* = 0.58$.

The images are also analyzed with PIV and the corresponding PIV results for these images can be seen in Figure 4.13. A similar flow mechanism can be observed like for PAT of ice I. As it can be seen in Figure 4.13 (a), ice layer moves upwards after detaching itself from the boundaries of the cell. At this instant ice part is moving with an average velocity of 1 mm/s

($v^* = 0.67$). The characteristic velocity for process is taken as the inlet velocity of water and it is 1.5 mm/s ($v^* = 1.00$). On the phase change interface (upper boundary of gray area in Figure 4.13a) the separation layer is not as strong as it is for PAT (Figure 4.6a). Through the interface fluid moves together with the ice layer directed to upwards. It shows that, in case of PST, ice structure is strongly affected from the pressure increase and it immediately starts to melt as well as on the ice-water interface. Point 1 in Figure 4.13 (a) has 2.3 % of the surrounding fluid velocity and a similar characteristic can be seen in other images in Figure 4.13. Again this point creates a stagnation type flow in this region. Disturbed flow areas, located at the right side of the cell, are observable even at the first image. The right side is where pressure inlet is located. The location of the inlet causes an asymmetry towards to the opposite direction of PAT. The maximum velocity in region 2 is 1.2 mm/s ($v^* = 0.80$) and this maximum velocity is seen near the ice-water interface. In region 3, velocity increases in the direction from center of the cell to the wall and takes its maximum value as 2 mm/s ($v^* = 1.33$).

In Figure 4.13 (b) flow disturbance in region 3 becomes more visible and the velocity values in this region are on average 1 mm/s ($v^* = 0.67$). In region 2, the maximum velocity has a maximum value of 1.2 mm/s ($v^* = 0.80$) as in the first image, and in the near wall region velocity decreases to an average of 0.6 mm/s ($v^* = 0.40$). Ice velocity remains almost unchanged being 1 mm/s ($v^* = 0.67$) on average.

In Figure 4.13 (c) ,in the upper part of the cell, point 1 can be observed as stagnation point in front of a vortex which just begins to form. The average velocity values for region 2 stay as before, whereas the left side of the region 3 has increased velocities. It can be seen that the maximum velocity reaches 2.3 mm/s ($v^* = 1.53$) and the average velocity increases to 1.8 mm/s ($v^* = 1.20$). The flow disturbances together with significantly increased velocities bring the possibility to have turbulence in region 3. When we compare this flow characteristic with the one from PAT, the main difference is flow disarrangement caused by the application of pressure.

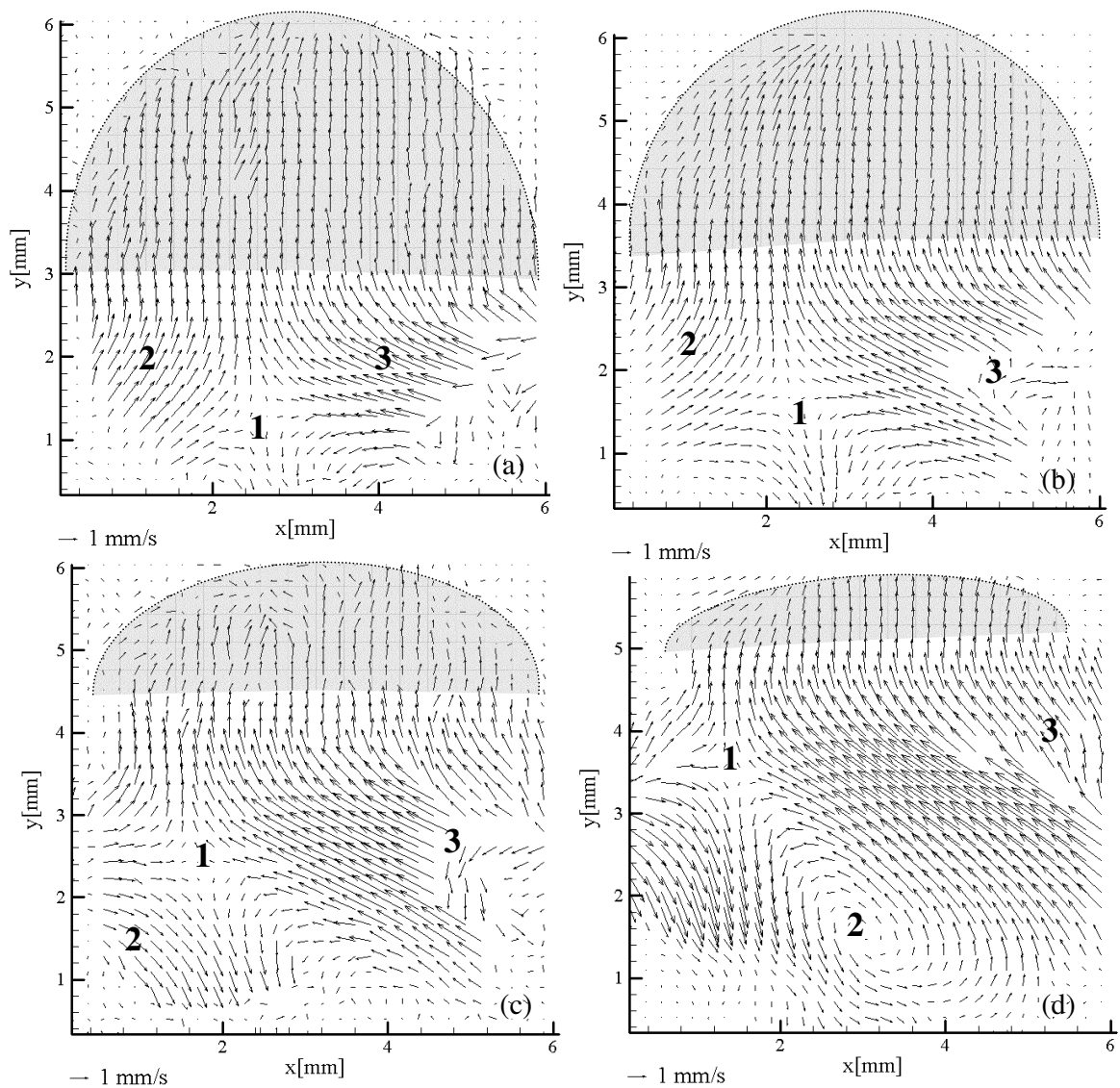


Figure 4.13: PIV analysis of images during PST of ice I (corresponding images for Figure 4.12)

In Figure 4.13 (d) the vortex is completely formed in the center of the flow. The flow is accelerated not only because of the pressure but also because of the increased amount of water volume in the cell. In other words, the last volume of ice is also changed into water at that moment and this creates acceleration in flow because of the sudden density change. The regions surrounding labeled points prove this with their high velocities. Between points 2 and 3, the average velocity is measured as 2.7 mm/s ($v^* = 1.80$), that is the maximum velocity that appears in the whole sequence as well as in the whole sequences represented in this work. The two minima of velocity are found at point 1 and 2, at stagnation point and at the center of the

vortex, respectively. The velocities are 0.18 mm/s ($v^* = 0.12$) for point 1 and 0.12 mm/s ($v^* = 0.08$) for point 2.

The temperature differences that can be observed by eye from the color of the liquid crystals are different for PAT (Figure 4.5) and PST (Figure 4.12). In Figure 4.12 the temperature gradients in the cell are more apparent. Digitalized temperature values for those images can be seen in Figure 4.14.

First image in Figure 4.14 belongs $t^* = 0.65$, which is 5 seconds ($t^* = 0.08$) after ice begins to arise. The ice layer is observable with the white curvature located horizontally in the middle of the cell. The temperature distribution is also detectable in the upper half of the cell. Actually as can be seen from the corresponding image in Figure 4.12 (a), this area is occupied by ice. Unlikely to the case in PAT, the ice structure discomposes faster in the center. Therefore, the reflected light from liquid crystals expresses the hue value in the calculation range but not the exact values because the liquid crystals are embedded in ice. Since the calibration of TLC is carried out just with liquid phase, temperature field in the ice region is not taken into consideration. In the fluid region, temperature changes between $-8\text{ }^\circ\text{C}$ to $-9\text{ }^\circ\text{C}$. At this moment the temperature value read from the thermocouple in the cell is $-8.7\text{ }^\circ\text{C}$ ($T^* = 0.986$).

In Figure 4.14 (b) temperature changes between $-7.6\text{ }^\circ\text{C}$ ($T^* = 0.990$) and $-8.7\text{ }^\circ\text{C}$ ($T^* = 0.986$). If the coldest area on the right side of the cell is found in Figure 4.13 (b), it can be gathered that it corresponds to region 3 where the flow faces with disturbances. Therefore the contribution of convective transport to temperature distribution in the cell should play an important role. After two seconds, in Figure 4.14 (c), the temperature in the center of the cell increases to a range of $-7.6\text{ }^\circ\text{C}$ ($T^* = 0.990$) to $-7\text{ }^\circ\text{C}$ ($T^* = 0.993$). Lower part of the ice layer (the white area) can be differentiated with its lower temperatures than the center of the cell. The fluid having direct contact with ice has expectedly lower temperatures. If the velocity profile of the figure is noticed in Figure 4.13 (c), it can be observed that the coldest area overlaps with the area where the flow is not fully developed. At this moment, the thermocouple shows $-8.46\text{ }^\circ\text{C}$ ($T^* = 0.987$) as temperature. In the last image, warmer regions become dominant and temperature in this region reaches to $-7\text{ }^\circ\text{C}$ ($T^* = 0.993$). The ice and the black area in Figure 4.12 (d) are detectable in the temperature field. Here again, the flow distortion in velocity field of the image (Figure 4.13 d) corresponds to the area with minimum temperature. Thermocouple reads still $-8.46\text{ }^\circ\text{C}$ ($T^* = 0.987$) at this moment. As a

reason, it could be considered that PST is occurring at a fast rate, the response time of the thermocouple may not be enough to gather the correct temperature. Moreover, the place of thermocouple is located at the top of the cell and it is certain that the temperature can vary between different locations of the cell in spite of the small volume of the device. For the whole sequence temperature difference can reach up to a value of almost 2 °C ($T^* = 1.026$). It shows that even with a volume of 2 ml, some inhomogeneities in temperature profile can be possible during high pressure processing. As previously discussed in section 1.1, high pressure processing is reported as an instantaneous and homogeneous process. Strong effects of forced convection observed in case of PST prove in contrary of the given statements in those studies. Delgado

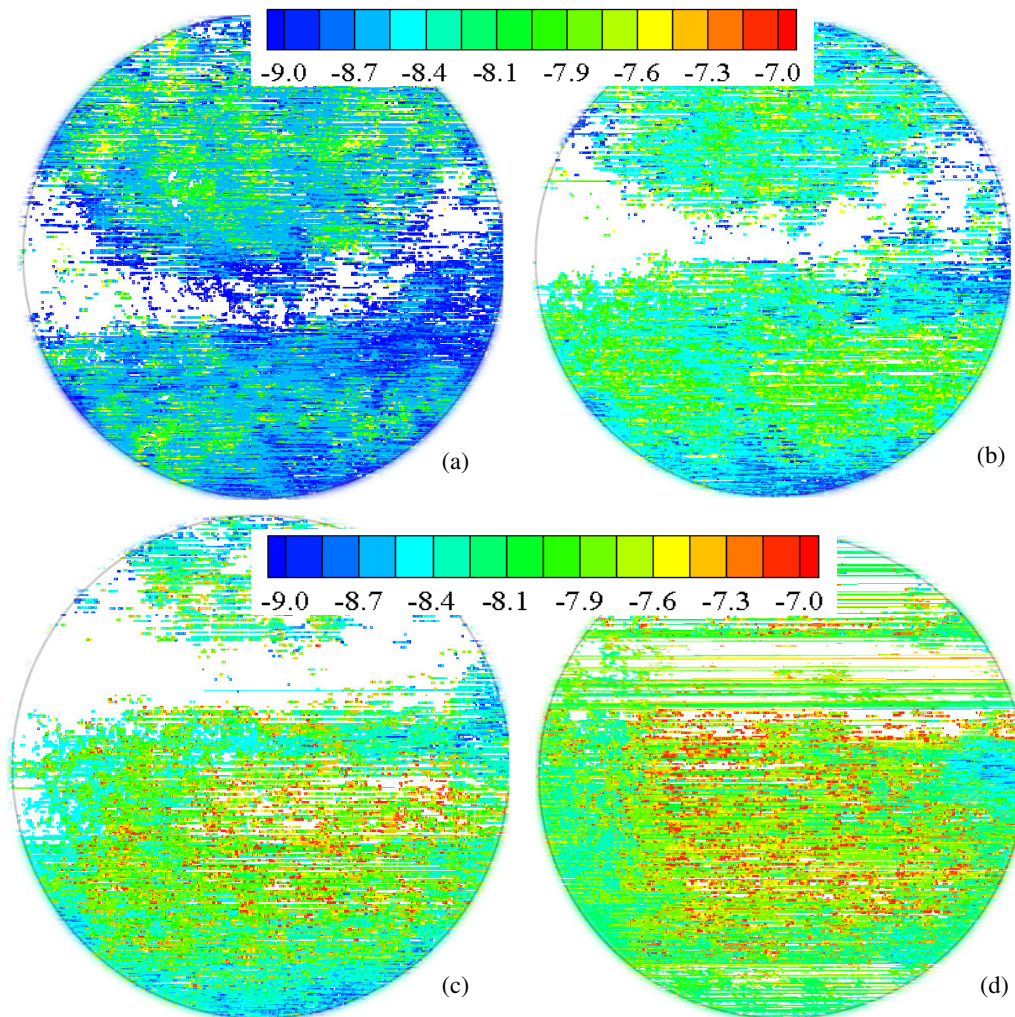


Figure 4.14: Temperature field results (in °C) of images during PST of ice I (corresponding to Figure 4.12)

and Hartmann (2002) have also investigated and combined theoretical and experimental findings. They concluded that the pressure effect can be considered as an instantaneous but not homogeneous in processing of fluid food.

For PST process the system of equations are given in section 3.3.1 and dimensionless forms of equations can be found in Tables 3.1, 3.2, 3.3 and 3.4. Re number has a value of 11.8, the Fr number is 1.64×10^{-5} , Ec is 2.3×10^{-12} , Pr is 11.5 and Ste number is 0.039.

Dimensionless form of momentum equation (Table 3.2 and 3.3) is composed of the rate of momentum change, the convective momentum transport, pressure, frictional stresses and gravitation. Frictional stresses appear together with $1/Re$ which has a value of 0.085 and gravitational forces can be seen with $1/Fr$, which is 6.1×10^4 . Consequently, frictional forces do not play an important role in momentum transport in comparison with the contribution of gravity.

The dimensionless form of energy equation for PST can be seen in Table 3.4. The main contribution is introduced by the rate of temperature change and the convective temperature change. $\alpha_0 T_0$ has a value of 6.7×10^{-2} , that shows it has less importance relative to the rate of temperature change and its convective contribution. The thermal conductivity should be considered with $1/Re.Pr$ (or $1/Pe$) which is 7.5×10^{-3} and has again less significance compared to the mentioned terms. The change of kinetic energy to thermal energy is found to have a constant of 1.9×10^{-13} (Ec/Re) and has negligible contribution to the energy of the system. Gravitation term appears here with the dimensionless group Ec/Fr which has a value of 1.4×10^{-7} . Thus the effect of gravity on energy can not be neglected but it is not so significant either in comparison to the terms except the term of change of kinetic energy to thermal energy. It should be emphasized that the contribution of gravity to momentum transport is more significant than its effect on energy transport of the process. The other two terms appearing in energy equation are the temperature change caused by crystallization enthalpy and its convective contribution. The former is represented with the dimensionless number Θ/Ste having a value of 19, and the dimensionless group for the latter is $Ec\Theta/Ste$ with a value of 6×10^{-11} . Therefore, only the direct temperature change caused by crystallization enthalpy plays an important role and convective contribution can be neglected.

Shear rate, strain rate, vorticity and dissipation are calculated as it is previously mentioned in section 4.2.1 by using velocity field results. Through the entire process shear rate has values between -3×10^{-3} 1/s and 5.1×10^{-3} 1/s ($\dot{\gamma}^* = -0.18$ to 0.31). As it is for PAT process, only the

maximum shear rate is increased in PST. Shear rate contours for the first and the last images of Figure 4.13 are depicted in Figure 4.15. At the beginning of the process (Figure 4.15a) there are inconsiderable differences in shear rate in the cell. The negative shear rate areas lay on the boundary regions and also where flow disturbance is seen. Through the sequence, these negative shear rate areas occur in this flow disturbance region. In Figure 4.15 (d) shear rate is positive in the centre of vortex and negative in its surrounding region. The highest positive values are seen on the boundary where the vortex circle intersects with disturbed flow region. The negative maximum can be seen at the right side of the vortex.

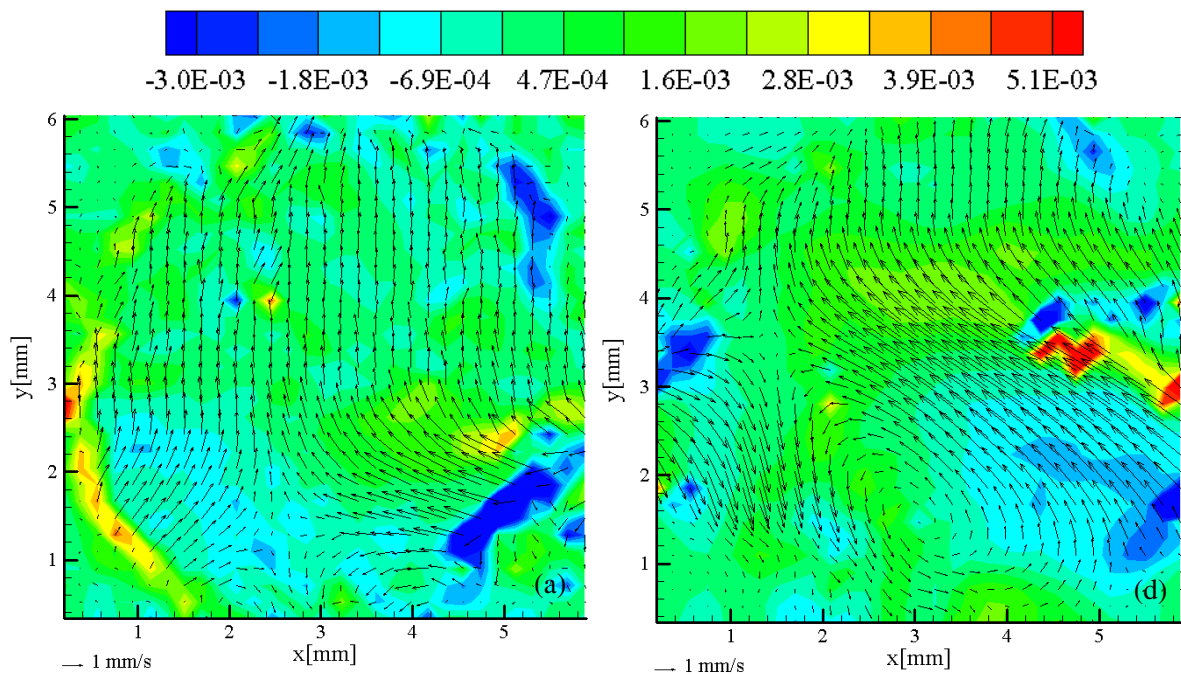


Figure 4.15: Shear-rate (in 1/s) contour plot for image (a) and (d) of PST of ice I (corresponding to Figure 4.13)

The strain rate takes values between -3.6×10^{-3} 1/s ($\dot{\epsilon}^* = -0.22$) and 6.3×10^{-3} 1/s ($\dot{\epsilon}^* = 0.38$) during the process. In the following figure (Figure 4.16), the contour plots of strain rate can be seen for PST. In the first image, the highest positive strain rate area accords to the negative shear rate area in Figure 4.15 (a). Moreover, the maximum negative of strain rate can be seen on the outer boundary. In Figure 4.16 (d) the positive maximum is in the centre of the vortex and in the left side of the centre strain rate reaches its negative maximum where the compressive forces are dominated.

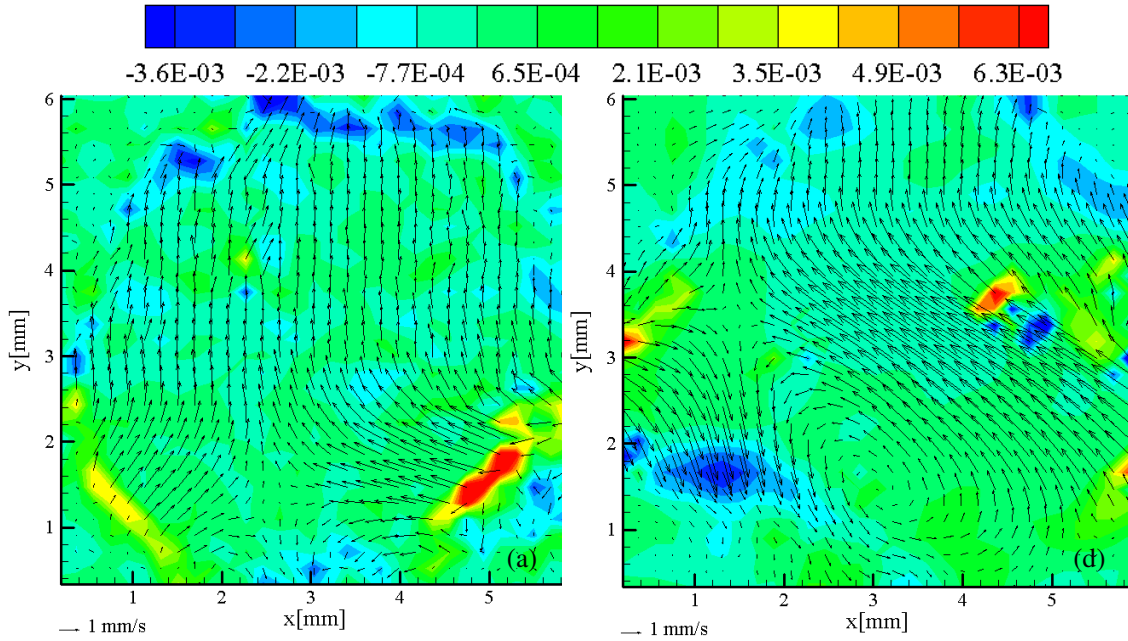


Figure 4.16: Strain-rate (in 1/s) contour plot for image (a) and (d) of PST of ice I (corresponding to Figure 4.13)

Vorticity behavior of the process is depicted in Figure 4.17. From the physical definition, the negative vorticity values represent clockwise rotation and positive values interpret counter-clockwise rotation in the fluid motion. In the first figure a small area is observed with negative vorticity values at the solid liquid interface. The vortex in the middle of the cell can definitely be observed in vorticity contour in Figure 4.17 (d). As its sign also affirms, there is a counter-clockwise rotation where the vorticity has its positive maximum in the cell. The slight rotation corresponding to the negative vorticity values can also be differentiated from the direction of the velocity vectors in blue areas. Its values changes between (ω^*) -0.24 and 0.27.

Viscous dissipation is also analyzed for PST process. It has values between $9.7 \times 10^{-6} \text{ 1/s}^2$ ($\Phi^* = 0.035$) and $1.5 \times 10^{-4} \text{ 1/s}^2$ ($\Phi^* = 0.54$), which are approximately ten fold increased in comparison with PAT. Indeed, dissipation reveals almost in the same manner as it is observed for PAT. The maximum dissipation values are observed in the regions depicted with 3 in Figure 4.13 for the whole sequence.

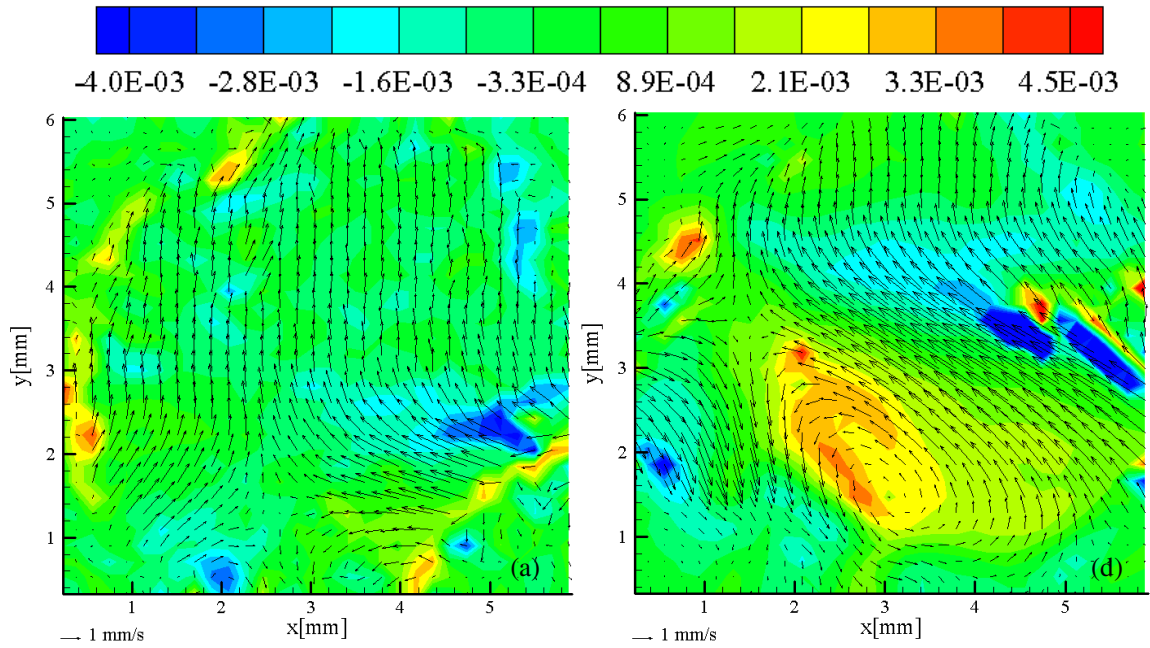


Figure 4.17: Vorticity (in 1/s) contour plot for image (a) and (d) of PST of ice I (corresponding to Figure 4.13)

When the values of those parameters are compared for PAT and PSF, it is seen that values are in the same order of magnitude. Maximum shear rate and strain rate values for PST are two times greater than that of PAT. Due to the effect of pressure introduced to the process, higher velocity values and relatively greater shear and strain rate values are observed. Moreover, pressure brings inhomogenities to thermal and fluid-dynamical properties of the system.

4.3.3 Pressure Shift Freezing to Ice I

For pressure shift freezing (PSF) to ice I, the experiments are performed according to the procedure explained in Section 2.2. For the experiment that will be discussed here, initial temperature and pressure of the cell are $-8.5\text{ }^{\circ}\text{C}$ ($T^* = 0.987$) and 160 MPa ($p^* = 0.148$). Temperature of the tempering bath is kept constant at $-10\text{ }^{\circ}\text{C}$ throughout the process. Phase change process is induced by decompression of the cell volume. The pressure decrease rate is again 15 MPa/s (for water at $20\text{ }^{\circ}\text{C}$). The temperature of the cell measured by thermocouple versus pressure of the cell during the process can be seen in Figure 4.18. The time between the start of pressure decrease till the sharp temperature change corresponding to phase change is approx. 50 seconds ($t^* = 0.83$) which can be seen from the Figure 4.18(a). Decompression starts at around 15 seconds ($t^* = 0.25$) and continues until 60 seconds ($t^* = 1.00$). The instant at which phase change occurs can be differentiated with a sudden temperature increase which is caused by release of latent enthalpy. At the time of release of heat temperature increases from $-8.8\text{ }^{\circ}\text{C}$ ($T^* = 0.986$) to $-7.0\text{ }^{\circ}\text{C}$ ($T^* = 0.993$), which corresponds to time $t^* = 0.83$. At this moment pressure stays constant for a couple of seconds and continues to decrease. A pressure increase is supposed to happen because of the volume change caused by ice formation in the cell. Since decompression is applied also during the phase change, this potential pressure increase is compensated by this pressure release and only at the moment of freezing pressure stays constant.

In high pressure shift freezing studies it has been observed that during pressure release the temperature of the sample is first depressed due to depressurization. When the difference between the sample temperature and the temperature corresponding to the current pressure becomes too large, a sudden temperature rise is observed at the instant of nucleation (Denys *et al.*, 1997; Chevalier *et al.*, 2000; LeBail *et al.*, 2002). And this temperature difference is called as supercooling, in other words it is the phenomena when a liquid is cooled down below its freezing point without freezing taking place or a metastable condition. The temperature decrease at the beginning of the process corresponds approximately between 20 ($t^* = 0.33$) and 50 seconds ($t^* = 0.83$) in Figure 4.18(a). In Figure 4.18(b), it can be seen that phase change takes place not exactly on the phase change line of water but at a lower pressure than the pressure on the phase change line. The difference between the temperature at which the nucleation starts and the temperature corresponding this pressure on phase change line of water is the amount of supercooling and it is $2.8\text{ }^{\circ}\text{C}$ ($T^* = 1.029$) in this case.

The degree of supercooling closely depends on the pressure release rate. It has been reported that the maximum supercooling, which could be reached for pure water with pressure levels of 150 MPa and 100 MPa, is 14.3 °C and 8.7 °C, respectively. However, such supercooling is possible only if the pressure release is instantaneous. Chevalier *et al.* (2000) could reach a supercooling of 5.4 °C (at 100 MPa) and 8.9 °C (at 150 MPa) in their experiments.

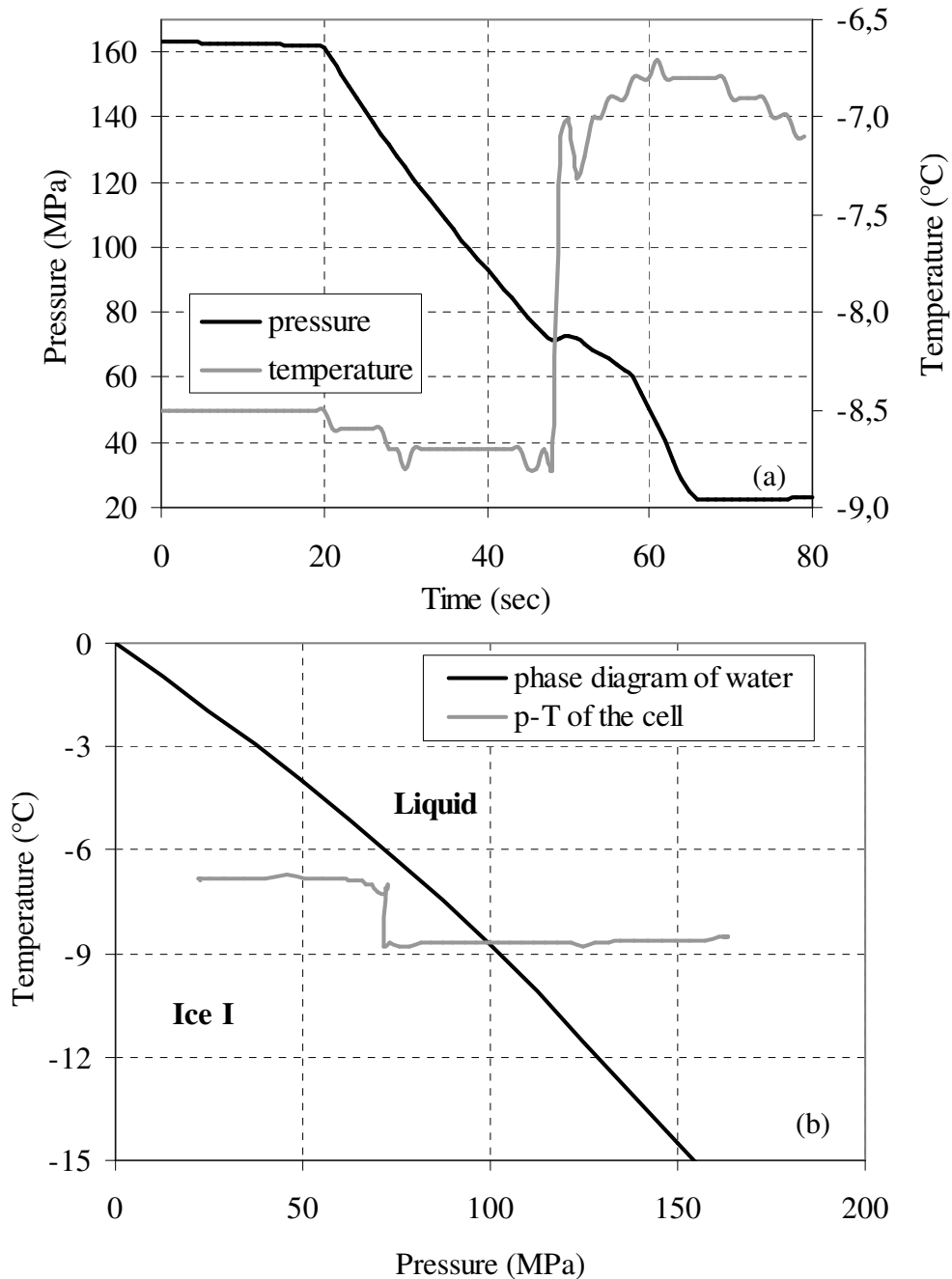


Figure 4.18: Pressure-temperature change during PSF of ice I. (a) given respect to time (b) given with phase change diagram of water.

Principally, supercooling induces nucleation at an elevated rate. Thereafter, the temperature tends to increase up to the atmospheric freezing temperature according to the phase change diagram of water under high pressure. By the help of pressure release ice crystals grow while nucleation might still be occurring due to the rapid evolution. As LeBail *et al.*(2002) also state the formation of homogeneous ice nucleation at the core is induced and in this way small ice crystals can be obtained. Here, the term homogeneous does not refer to a homogeneous ice nucleation where there is no surfaces and particles exist which effect the nucleation. This homogeneity is the formation of more uniform ice crystals compared to conventional freezing. The amount of supercooling in our experiments (2.8 °C) is comparatively smaller than the ones reported in literature (14.3, 8.7, 5.4, 8.9 °C). Other than experimental and dimensional differences, another reason for this difference may lay in the extra inhomogeneities brought to the system by existence of liquid crystals. As it was already given their diameter changes between 10 to 15 µm. The concentration that is used results in a final particle number of approximately 10^{13} , which is a high number of particles and this can not be seen in a natural system. Therefore, existence of liquid crystals may produce more nucleation surfaces during ice nucleation. As a result, high degrees of supercooling can not be achieved.

The main advantage of high pressure is reported as this characteristic of facilitating supercooling and promoting rapid and uniform ice nucleation in the sample. Application of slow or classical freezing generally results in larger ice crystals causing extensive mechanical damage. In this study, classical freezing can not be experimentally compared with high pressure freezing because during classical freezing ice formation occurs first on the window unit and visualization of the process becomes impossible.

After nucleation takes place the temperature in the cell continues to increase for a while because of the released latent enthalpy. After that, it is equalized with the surrounding temperature controlled by thermal bath.

The images for the sequence are demonstrated in Figure 4.19. Images in this figure belong to approximately 25 seconds before nucleation ($t^* = 0.83$). The color change from white to yellow is first observed at the beginning of the process at time zero (Figure 4.19a). Altering of reflected light from yellow to blue band is occurring in almost $t^* = 0.12$. Corresponding time of each image in the sequence can be seen in Figure 4.19. Sudden ice formation becomes visible on the window at around $t^* = 1.00$. As it can also be visualized from video sequence,

nucleation is taking place suddenly. Therefore, it is not possible to analyze the moment of nucleation in the cell volume.

The velocity profile and contour plots for the process are demonstrated in Figure 4.20. As it can be seen from this figure, the flow originates from the source of the pressure release. The flow is directed to the pressure inlet on the bottom-right of the cell. The strong interaction between pressure and evolution of velocity through the process can be noticeably observed from velocity contour plots. Velocity is increasing as long as process continues. Actually the rate of pressure release is not altered during the process but declining pressure has some effects on physical characteristics of water. Its effect on density would play a role in fluid dynamical properties as well. At a given temperature when decompression is introduced to a volume of water, density shows a tendency to diminish as well. Therefore convective transport can eventuates with a higher rate because of the lower density of liquid.

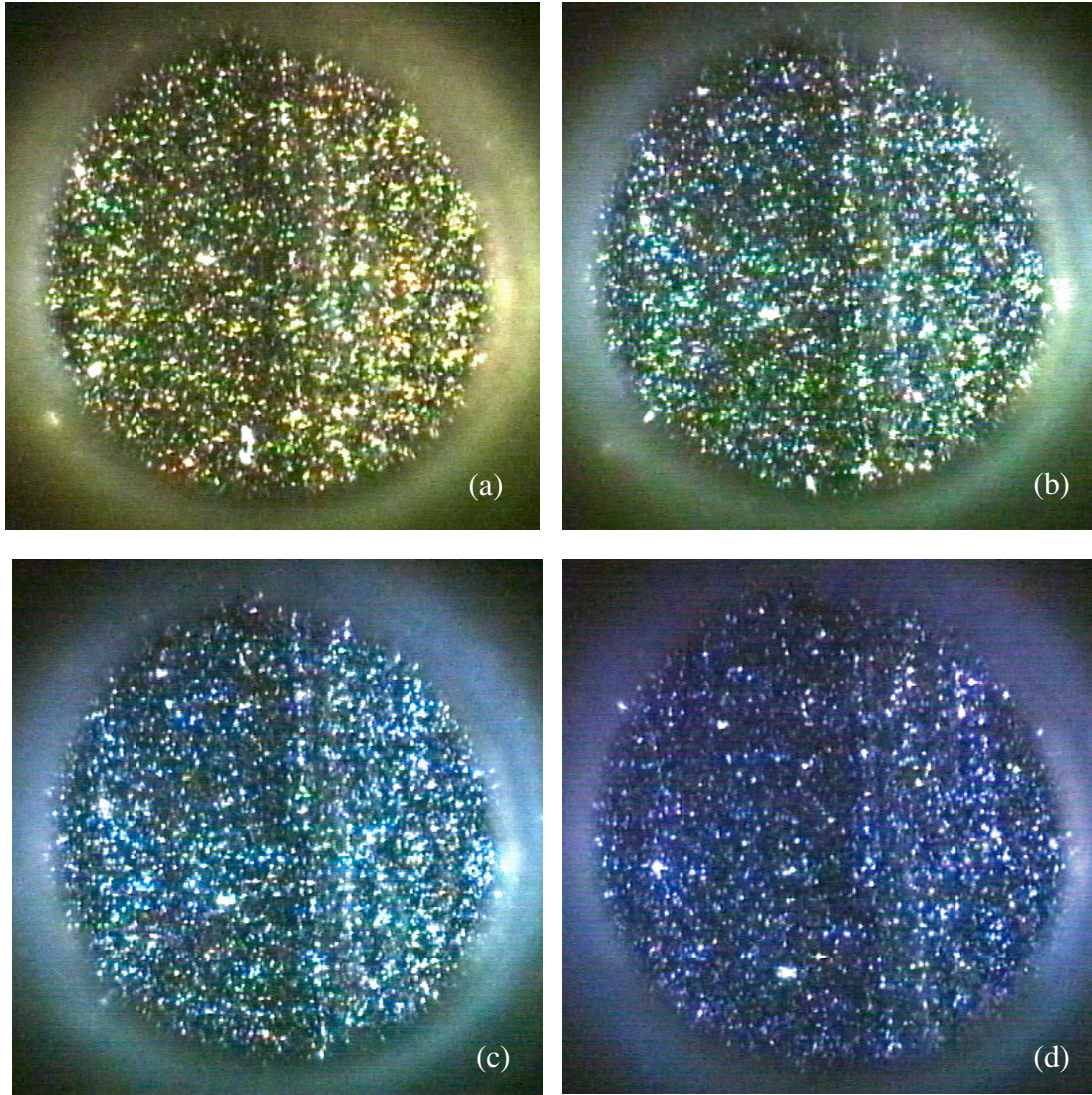


Figure 4.19: Images from PSF of ice I at different times (a) $t^* = 0.38$, (b) $t^* = 0.43$, (c) $t^* = 0.45$, and (d) $t^* = 0.50$.

Digitalized temperature fields of the process are depicted in Figure 4.21. As it could also be gathered from Figure 4.19, temperature fields throughout the process are homogeneous. Those images correspond to the period just after the pressure release. As previously discussed in this section, the temperature of the sample is first depressed due to depressurization which can be seen in Figure 4.18 (a). The amount of decrease is $0.3\text{ }^{\circ}\text{C}$ if it is calculated from the thermocouple measurements. Whereas the digitalized temperature fields depict stronger decrease in temperature. Temperature decrease between the first and the last image amounts to almost $2\text{ }^{\circ}\text{C}$ ($T^* = 1.026$). This discrepancy can be caused because of the slower time response of the thermocouple compared to the rate of freezing process.

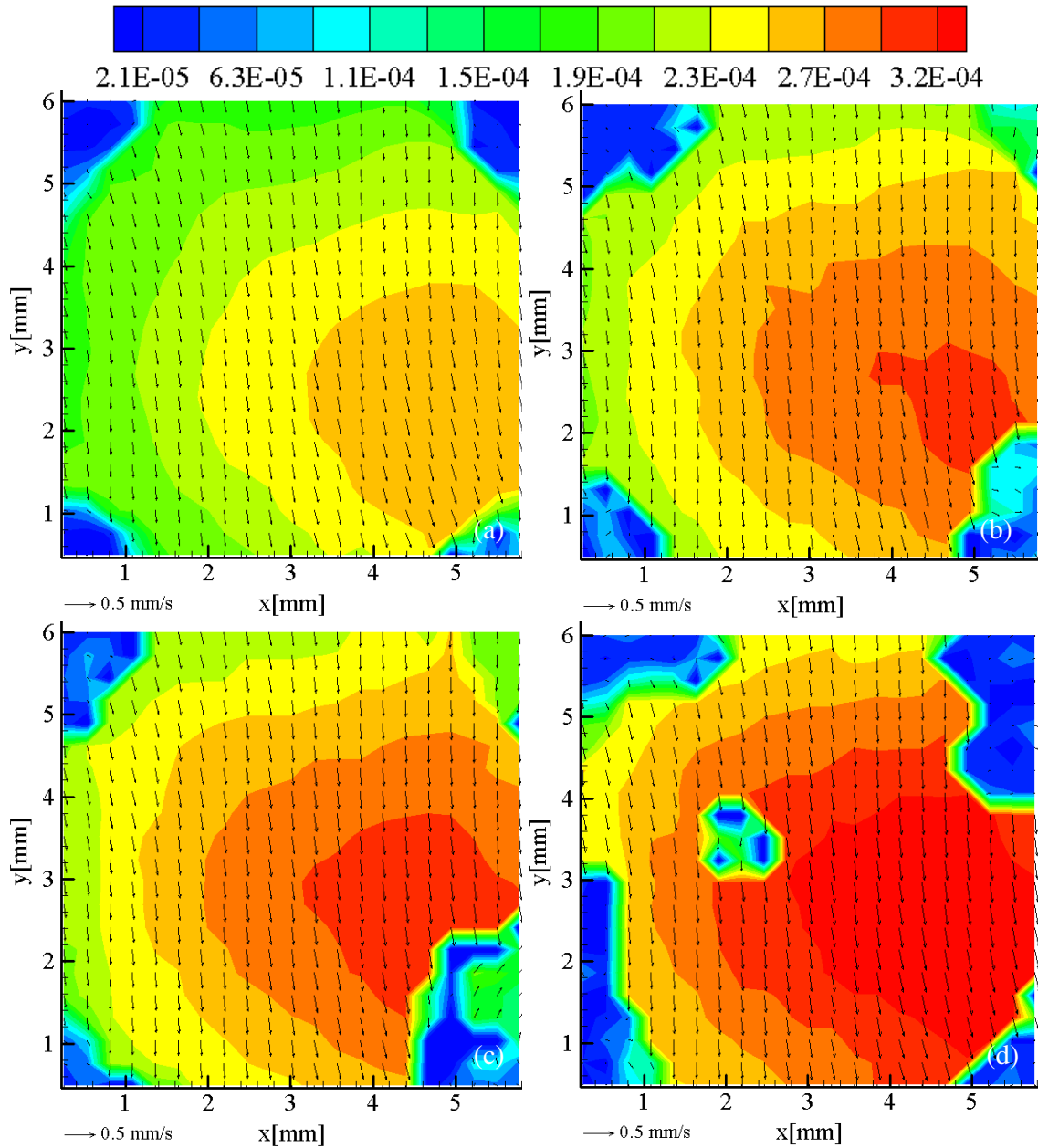


Figure 4.20: Velocity contour (in m/s) and PIV results of images during PSF of ice I (corresponding to Figure 4.19)

The difficulty concerning inefficient rate of data acquisition is enunciated in literature as well. Experimental determination of supercooling could be efficient only if temperature and pressure variations are recorded with a high data acquisition rate (Chevalier *et al.*, 2000). They compared the measured temperature values with the theoretically supposed temperature at corresponding pressure and obtained differences up to 5 °C s.

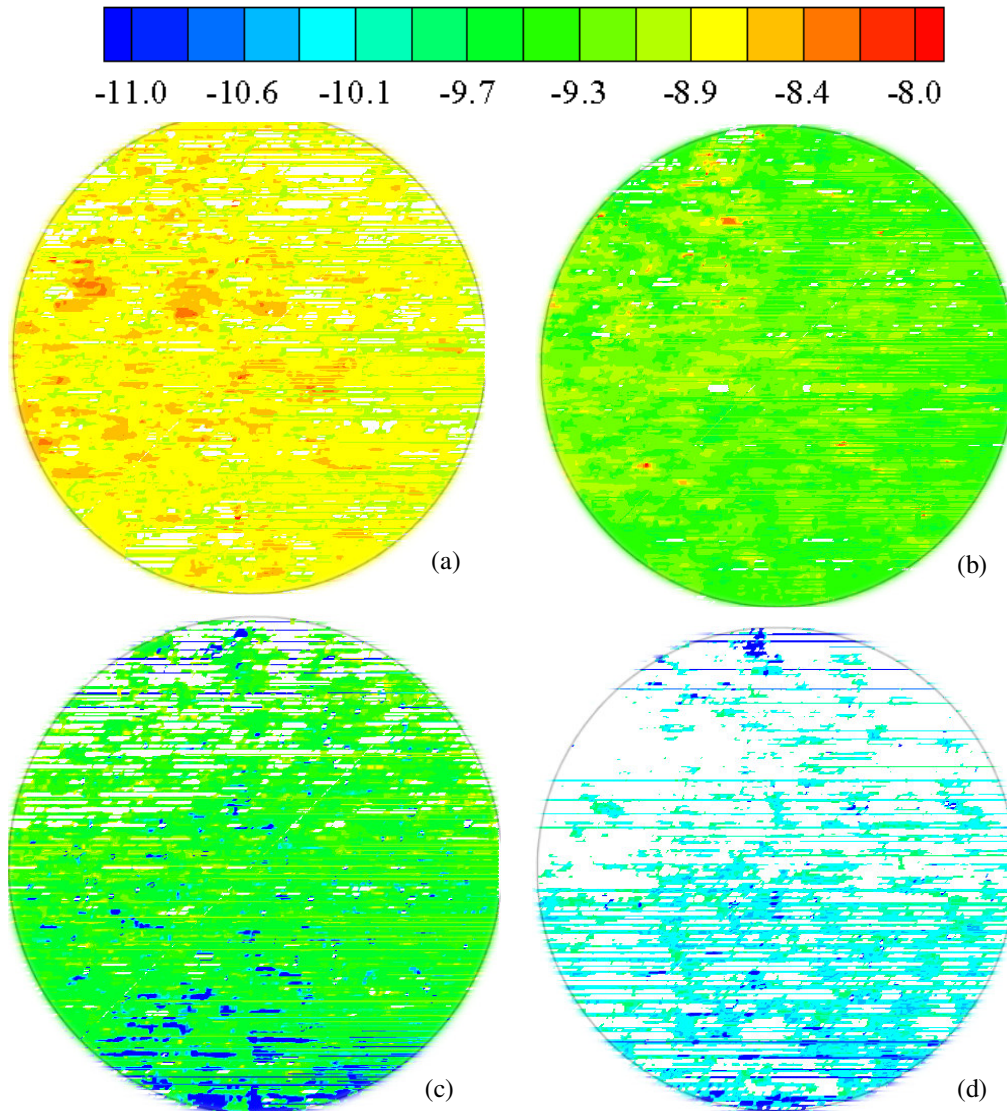


Figure 4.21: Temperature field results (in °C) of images during PSF of ice I (corresponding to Figure 4.19)

PSF process is represented with the equations and dimensionless numbers that are developed for PST process. Dimensionless form of momentum equation is, in this case, composed of only equations for fluid phase not the solid phase while there is no solid body motion in system (see Table 3.2). Dimensionless form of energy equation for the process is given in Table 3.4. Characteristic dimensionless numbers for PSF are same like PST because the same reference temperature and velocity values are accepted. An important difference concerning flow mechanism is the effect of gravitation. In this time gravitation and the force applied by release of pressure are in the same direction. Briefly, all terms in Table 3.4 are important in

energy transport except the change of kinetic energy to thermal energy and the convective part of crystallization enthalpy.

During PSF process minimum velocity values and more homogeneous flow fields are observed in comparison with other processes. Other parameters characterizing the flow field are also investigated for PSF. Shear rate changes between -5.3×10^{-4} 1/s ($\dot{\gamma}^* = -0.032$) and 5.1×10^{-4} 1/s ($\dot{\gamma}^* = 0.031$) and does not show any significant difference according to the position in the cell as well as in the time course of the entire process. Negative maximums are observed on the outer boundaries. Positive maximums are located at the region where slight flow disturbances occur, i.e. near the pressure inlet (see Figure 4.20c). Regions at which compressive strain is observed, are again near the pressure inlet and as well as the upper half of the cell. No considerable tensile strain is observed during the process. Strain rate has values between -2×10^{-4} 1/s ($\dot{\epsilon}^* = -0,012$) and 5×10^{-4} 1/s ($\dot{\epsilon}^* = 0.032$). Dissipation during the process has extremely small values relative to that of discussed processes. It takes values between 2×10^{-10} 1/s² and 6×10^{-10} 1/s² ($\Phi^* = 7.2 \times 10^{-7}$ to 2.2×10^{-6}). When those parameters are compared with those of PAT and PST processes, it is seen that PSF has noticeably lower values for dissipation. For shear and strain rates there is a difference of 10 fold whereas for dissipation this difference becomes 10^5 fold. A main reason can be the change of density of water to ice, which is diminishing as pressure decreases.

High pressure freezing has been investigated and addressed in many of the studies because it's a determining process in preservation of food. The main interest other than its effects on final product quality is the effect of mechanical stresses acting on the biological tissues. Mechanical stress concept in freezing is actually refers to the stress that is brought to the system upon freezing. The main advantage of PSF is stated by not directly comparing the amount of stress but investigating its effects on final product quality.

4.3.4 Pressure Assisted Thawing of Ice III

Pressure and temperature conditions for ice III region can be seen in Figure 4.3. The only applicable thawing process for ice III is the pressure assisted thawing. Phase change process of ice III can not be easily controlled by pressure due to its existence in a quite narrow pressure range and to reach this region, it is started from ice I. Therefore the temperature pressure course of the experiment is presented together with this preparation step. At the beginning the temperature of the tempering bath is set to $-25\text{ }^{\circ}\text{C}$. First ice I is obtained in the cell and by pressure increase ice I-ice III phase change line is crossed, the process can be seen in Figure 4.22. During solid-solid phase transition between ice I-ice III a pressure decrease of 20 MPa ($p^* = 0.019$) is observed (the region depicted with a circle) which is a sign of density change of ice. Ice III has higher density than of ice I (see also Appendix A, Table A.2) and it is reported as $1.14 \times 10^3\text{ kg/m}^3$ (Tchijov *et al.*, 2004; Akyurt *et al.*, 2002) at around 300 MPa ($p^* = 0.278$), at those pressure and temperature conditions water has a density of $1.11 \times 10^3\text{ kg/m}^3$. Before thawing, initial temperature and pressure is set to $-23\text{ }^{\circ}\text{C}$ ($T^* = 0.933$) and 285 MPa ($p^* = 0.264$). Then the temperature of the surrounding bath is arranged to $-10\text{ }^{\circ}\text{C}$. Temperature pressure history of the process is given in Figure 4.22. The phase change temperature and pressure corresponds to $-19\text{ }^{\circ}\text{C}$ ($T^* = 0.948$) and 262 MPa ($p^* = 0.242$) according to the phase change diagram of water.

Temperature-pressure behavior during this process shows quite a different characteristic compared to other discussed processes. Controlling the process, i.e. the required temperature pressure conditions, is more difficult than as it is in other processes. It is started from ice III region in phase change diagram of water and it has been observed that temperature-pressure conditions are suddenly shifted to ice I or ice V region. This phenomenon is unique to ice III (and ice V) from the ice types that are currently under discussion and it is named as metastability of ice III.

Structure and properties of ice III have been often under investigation in the frame of high pressure processing. Concerning food systems a recent study introduced new concepts to HP food processing at low temperatures. Urrutia Benet *et al.* (2004) studied with potato samples having initial water content of 77% and observed a region where no nucleation of ice crystals are obtained by cooling in a region of ice III. According to this new region liquid/ice I/ice III triple point shifts from $-22\text{ }^{\circ}\text{C}$ at 209 MPa to $-28\text{ }^{\circ}\text{C}$ at 240 MPa. And it is defined as a

metastable liquid phase by Schlüter *et al.* (2004) after the statement of the same concept by Bridgmann (1912) and Evans (1967).

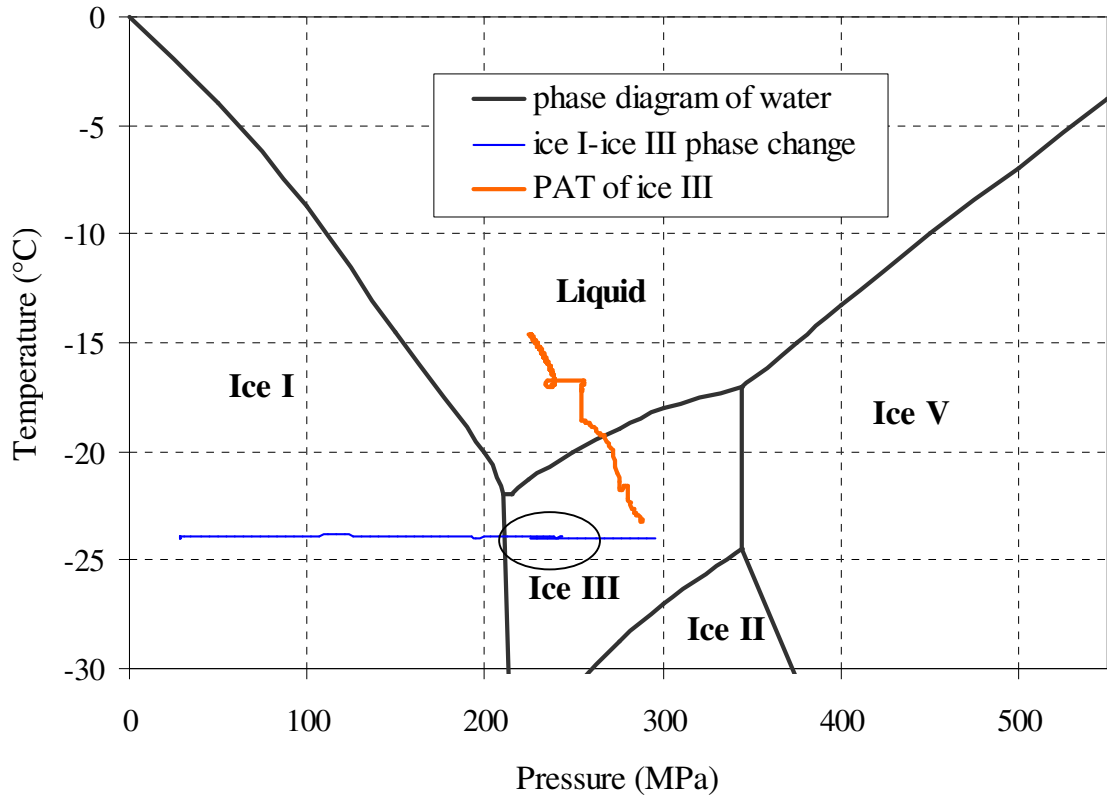


Figure 4.22: Pressure-temperature change during phase change processes related to ice III given with phase change diagram of water.

Different properties of ice III creates considerable changes in the flow characteristics as well. In this case two instants from the sequence are depicted due to the resemblance of velocity profiles within consecutive moments. In Figure 4.23, images (a, c) and corresponding velocity profiles (b, d) for this sequence can be seen. Thawing process occurs in 250 seconds ($t^* = 1$) and the motion of ice corresponds to a 30 second ($t^* = 0.12$) period in the whole thawing process and it begins at around $t^* = 0.48$ and ends at $t^* = 0.60$. Due to higher temperatures on the walls ice starts to detach itself from the walls but in this case it moves downward because of its higher density than that of water.

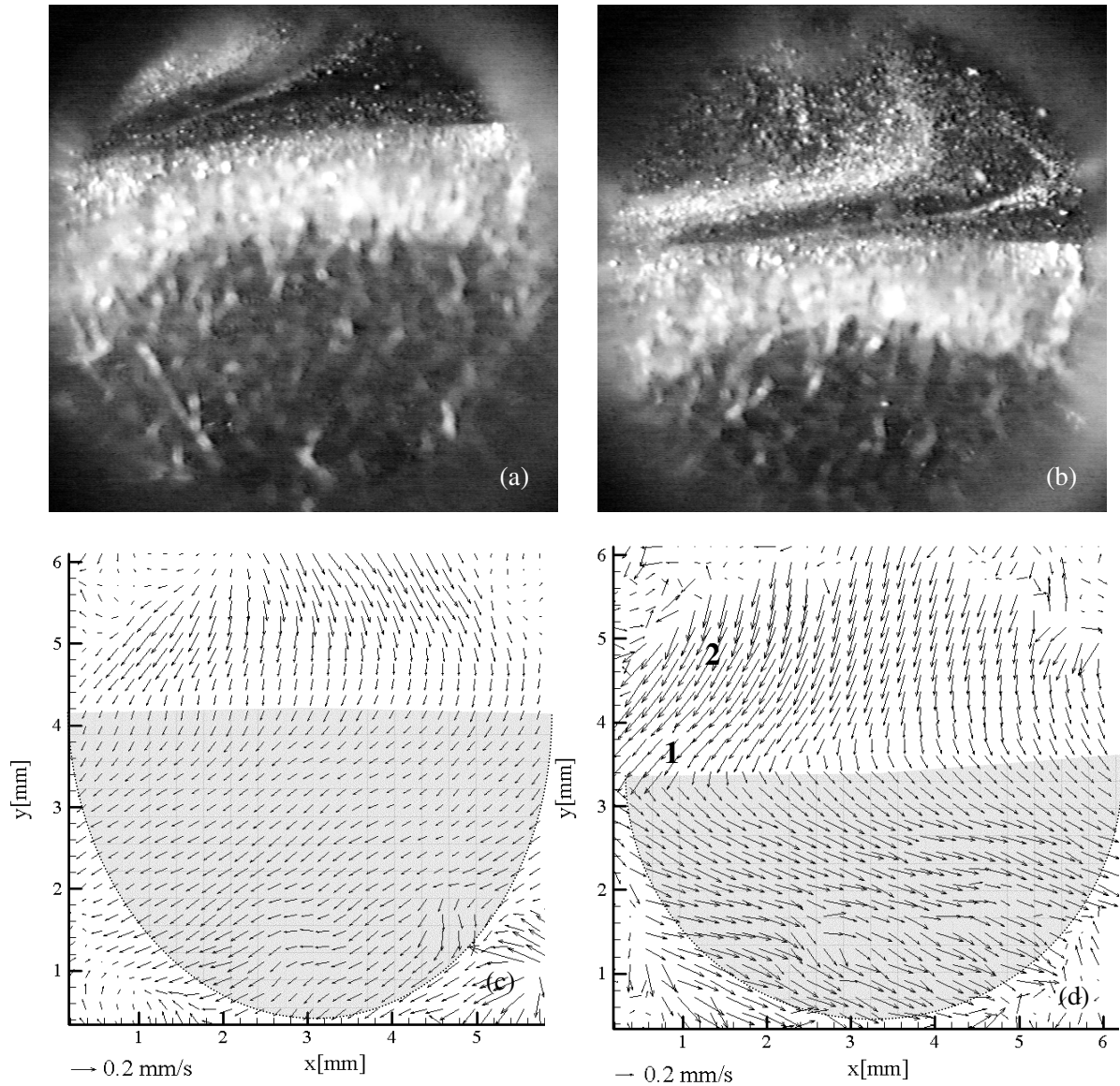


Figure 4.23: Images and PIV results from PAT of ice III (a) - (c) $t^* = 0.50$, (b) - (d) $t^* = 0.60$.

Ice layer is again detectable in real images as well as in PIV results. It has been observed that structure of ice III is visually different from Ice I. Its structure is not opaque as in the case of ice I. Some disturbances occur during PIV evaluations caused by this transparent appearance of ice as it can be seen in Figure 4.23 (d). Motion of ice, in this case, is not unidirectional like in the case of ice I and it changes its place in horizontal direction in the cell as well. This is caused by the effect of gravitational forces acting in the same direction of motion. For ice I gravity has a decelerating effect on the ice motion but here accelerating.

In the flow field of ice III, there can not be seen any dominant vortex as in case of ice I. There is a stagnant flow through the process. The average velocity of ice body in Figure 4.23 (c) is 0.08 mm/s and at the same moment fluid has a velocity of 0.2 mm/s ($v^* = 0.03$). As thawing proceeds velocity values increase for both ice and water, at maximum, ice velocity reaches 0.2 mm/s ($v^* = 0.03$) at the end of the process. Liquid velocity has its maximum the end of the process too and this is 0.47 mm/s ($v^* = 0.08$).

Other flow parameters discussed do not show significant differences in the sequence. Shear rate takes values between -7.9×10^{-4} 1/s ($\dot{\gamma}^* = -0.20$) and 1.0×10^{-3} 1/s ($\dot{\gamma}^* = 0.25$), having the negative maximum during the process at liquid-solid interface (region 1 in Figure 4.23d). Strain rate changes between -1.8×10^{-3} 1/s ($\dot{\epsilon}^* = -0.45$) and 1.9×10^{-3} 1/s ($\dot{\epsilon}^* = 0.46$) without any significant distribution in the cell. When vorticity values are observed, positive values are seen at and under region 1 till to a maximum of 1.0×10^{-3} 1/s ($\omega^* = 0.25$) and negative values are found in region 2 to a maximum of -5.7×10^{-4} 1/s ($\omega^* = -0.14$). Dissipation does not show any considerable change during the process and has values between 1.16×10^{-7} 1/s² ($\Phi^* = 0.007$) and 1.74×10^{-6} 1/s² ($\Phi^* = 0.11$). Higher dissipation areas are observed on ice-water interface.

Phase transitions in ice III region has also been investigated concerning inactivation of microorganisms. Luscher *et al.*(2004) found that subjecting *L.innocua* to phase transitions between ice I and ice III by pressurizing frozen aqueous systems above 200 MPa appears to be an effective way to reduce bacterial contamination, since with this strategy, three log cycles of reduction can be achieved instantaneously. In contrast, a holding time of 15 min is required to obtain the identical degree of bacterial decontamination in liquid state. It was also pointed out that the cellular damage is probably associated with the mechanical stress during the phase transition and not with the impact of pressure itself. In our study this mechanical stress can not be quantified but the visual effect in form of a sudden structure change during the transition from ice I to ice III is observed as a contribution to this phenomena.

The effect of ice III formation on cellular structures should also be investigated by the same study group (Luscher, 2005). They performed structural analyses of the plant tissue such as cell membrane, texture, color and visual appearance. Freezing to high ice polymorphs of a higher than liquid water (especially ice III) resulted in an excellent preservation of textural characteristics. Short phase transition as well as favourable volume changes improves the

quality of biological samples. As a result, the phase change with the lowest extent of cellular damage seems to be freezing to ice III, close to the triple point liquid- ice III- ice V.

4.3.5 Phase Change Processes of Ice V

Ice V, one of the high order ice modifications, is also investigated concerning its fluid-mechanics properties. In this section, different phase change processes of ice V are discussed together. As in the case of ice III, it is required to obtain only ice I, or both ice I and ice III to reach ice V region (Figure 4.3). It is selected the former and it is first obtained ice I in the cell, it is thawed by increasing pressure and after that again by compression ice V is achieved.

According to the terminology introduced to HP low temperature processing by Urrutia Benet *et al.* (2004), pressure shift freezing means that a sample is frozen due to a pressure release, leading to an instantaneous crystallization of ice, homogeneously distributed throughout the sample, as a consequence of the isotropic nature of pressure. Ice I is the only ice modification susceptible to PSF with its negative slope in the phase change line. Pressure induced freezing (PIF) is a process that involves the induction of a freezing phase change by pressure increase. This process is only applicable for higher ice modifications. Therefore this process is called PIT of ice V.

For PIT to ice V, the initial pressure in liquid region is 230 MPa at around -14 °C ($T^* = 0.966$). Then the pressure is increased till ice V is observed in the cell. The formation of ice V takes place at 535 MPa for this process. A supercooling effect can be noticed from temperature pressure course of the process (Figure 4.24). At the moment of freezing temperature suddenly increases from -10.2 °C ($T^* = 0.981$) to -6.4 °C ($T^* = 0.995$). A similar process curve and a supercooling of 5 °C are reported with water in literature as well (Urrutia Benet *et al.*, 2004).

The instable characteristic of ice V is observed in controlling the system. It is noticed that there are difficulties to accomplish the required temperature and pressure conditions for processes of ice V. Another point that could be effective in this behavior is that the physical properties of the experimental device do not allow reaching practically to 700 MPa ($p^* = 0.648$) for ice V process. Before reaching ice V region ice I region should be crossed first and during this phase change a volume decrease occurs. Therefore the practical maximum pressure in the cell can reach around 600 MPa for ice V experiments.

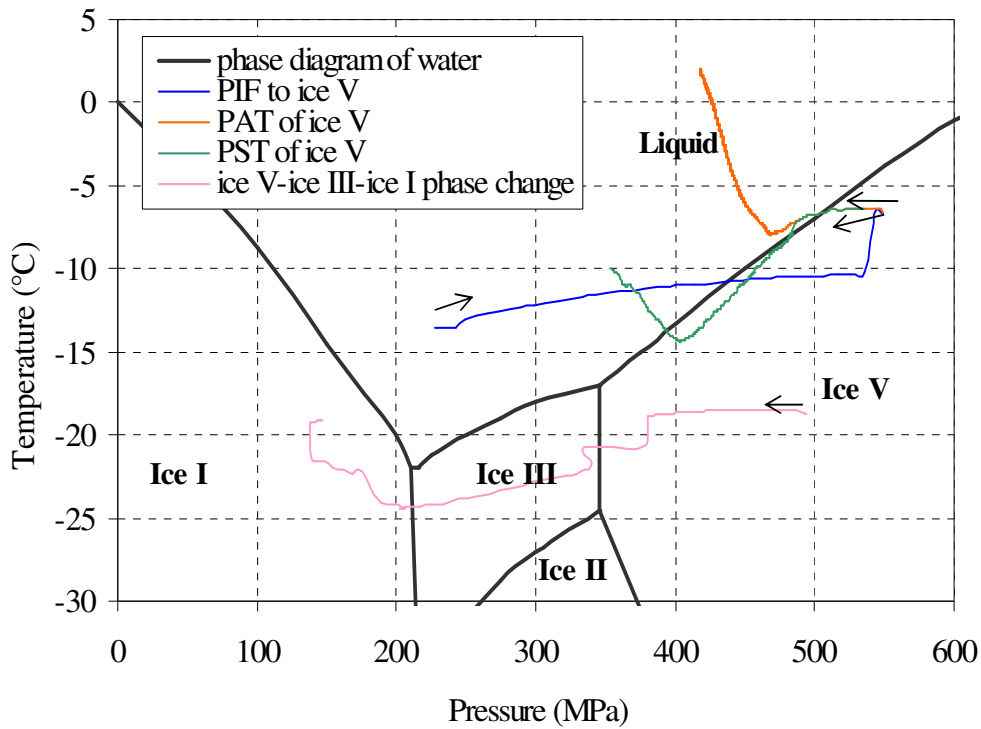


Figure 4.24: Pressure-temperature change during phase change processes of ice V given with phase change diagram of water.

Pressure shift thawing and pressure assisted thawing of ice V show similar characteristics concerning temperature and pressure behavior of the processes (see Figure 4.24). In pressure assisted thawing pressure decrease is taking place so fast that it creates a similar effect as in PST. The whole PAT process that is shown in graph occurs in 340 seconds ($t^* = 1.00$) and the motion of ice (the analyzed sequence) takes 25 seconds beginning from the moment around at 290 seconds ($t^* = 0.85$). During thawing temperature decreases 1.2 °C ($T^* = 1.023$) due to absorption of latent heat from surrounding. This amount reaches to 6.5 °C ($T^* = 1.043$) for PST because of the effect of pressure release as it can be seen from the graph. PST process lasts totally 110 seconds, the part of the analyzed images corresponds to the time between around $t^* = 0.21$ to 0.27 where the ice motion in the cell is observed

Images from PAT of ice V are given in Figure 4.25. A similar flow characteristic is observed as in ice III. The motion of ice is again downwards because of the density difference, ice V has a density of $1.25 \times 10^3 \text{ kg/m}^3$ (Tchijov *et al.*, 2004; Akyurt *et al.*, 2002) at around 500 MPa at which water has a density of $1.16 \times 10^3 \text{ kg/m}^3$. This motion creates again a stagnant type flow again with ice motion that is not unidirectional. In the fluid, maximum velocity is

gathered as 0.75 mm/s ($v^* = 0.12$) and location of high velocities can be seen in vector representation of the image (Figure 4.25d). Ice velocity becomes 0.09 mm/s ($v^* = 0.01$) at maximum through the process.

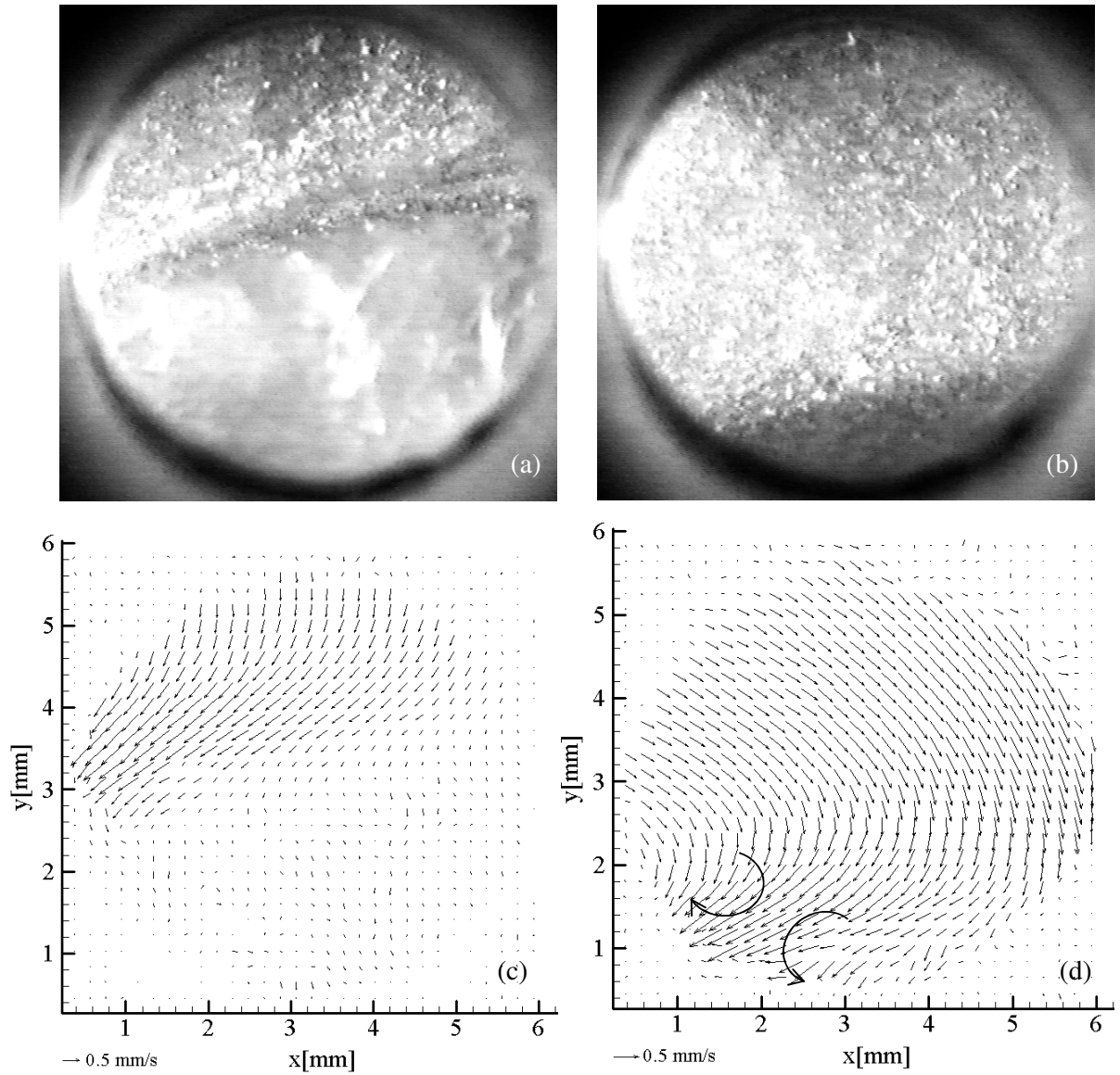


Figure 4.25: Images and PIV results from PAT of ice V (a) - (c) $t^* = 0.88$, (b) - (d) $t^* = 0.93$.

In the frame of analyzing other flow parameters, high shear rate areas are observed in ice-water interface having a maximum value of 1.1×10^{-3} 1/s ($\dot{\gamma}^* = 0.37$). As it can be predicted, these areas are high compressive strain regions due to negative strain rates of -2.6×10^{-3} 1/s ($\dot{\epsilon}^* = -0.88$). Moreover, from vorticity values the origin of vortex that is seen in Figure 4.25

(d) can be differentiated with negative vorticity values ($1.6 \times 10^{-3} \text{ 1/s}^2$, $\omega^* = 0.54$) implying the direction of the circular motion. And a layer (which lays between depicted vortices in the corresponding figure) can also be observed where two different directions of vortex exist at the same moment, where positive vorticity value is $1.4 \times 10^{-3} \text{ 1/s}$ ($\omega^* = 0.48$). Dissipation in the cell has its minimum value in the whole cell volume and it is $4.9 \times 10^{-7} \text{ 1/s}^2$ ($\Phi^* = 0.057$). It has the maximum value of $7.4 \times 10^{-6} \text{ 1/s}^2$ ($\Phi^* = 0.86$) in the region where the contact of two vortices are observed in Figure 4.25 (d).

Figure 4.26 depict the images and PIV representations of images for pressure shift thawing of ice V. Due to similarities between PAT and PST of ice V difference points are discussed concerning the flow field. As Figure 4.26(a) shows at the beginning of the process almost same flow type is observed as in PAT of ice V. As long as process continues, pressure removal alters the direction of motion and at the same time it causes symmetrical vortices to occur in the cell (Figure 4.26b). The flow distortion in this image is caused by the excess light reflection of the TLC in this region. As previously discussed, those undesirable reflections are probably caused by different arrangements of TLC during ice-water transition.

In general higher velocities and larger high velocity areas are observed for the current process (for PST of ice V). From the beginning of the process in fluid region the average velocity is 1.2 mm/s ($v^* = 0.80$) and the maximum is 1.5 mm/s ($v^* = 1.00$). At the end of the process, high shear rate areas are located on the lower end of the vortex in Figure 4.26(d) having value of $2.2 \times 10^{-3} \text{ 1/s}$ ($\dot{\gamma}^* = 0.75$). Except that, there can be no significant difference observed in shear rate values during the process. Related with strain rate, region with compressive strain is recognized on the lower end of the right vortex ($-6.0 \times 10^{-3} \text{ 1/s}$, $\dot{\epsilon}^* = -2.04$). Vorticity results validate existence of two counter rotating vortices by taking negative maximum at the left and positive one at the right side of the cell, $-2.1 \times 10^{-3} \text{ 1/s}$ ($\omega^* = 0.71$) and $4.0 \times 10^{-3} \text{ 1/s}$ ($\omega^* = 1.36$) respectively. The contribution of dissipation can only be seen on the outer boundary of the motion, there is no significant difference observed between ice-water layer and in the fluid. Dissipation has an average value of $3.0 \times 10^{-6} \text{ 1/s}^2$ ($\Phi^* = 0.036$) in the cell and a maximum of $1.9 \times 10^{-5} \text{ 1/s}^2$ ($\Phi^* = 0.23$) on the boundary of the cell.

Another observation concerns structural differences between ice III and ice V. Ice III is seen transparent during the processes whereas ice V's appearance has an opaque characteristic.

This may be a sign of metastable region of ice III and this transparency can be caused by the existence of ice-water mixture behind the ice layer instead of only ice.

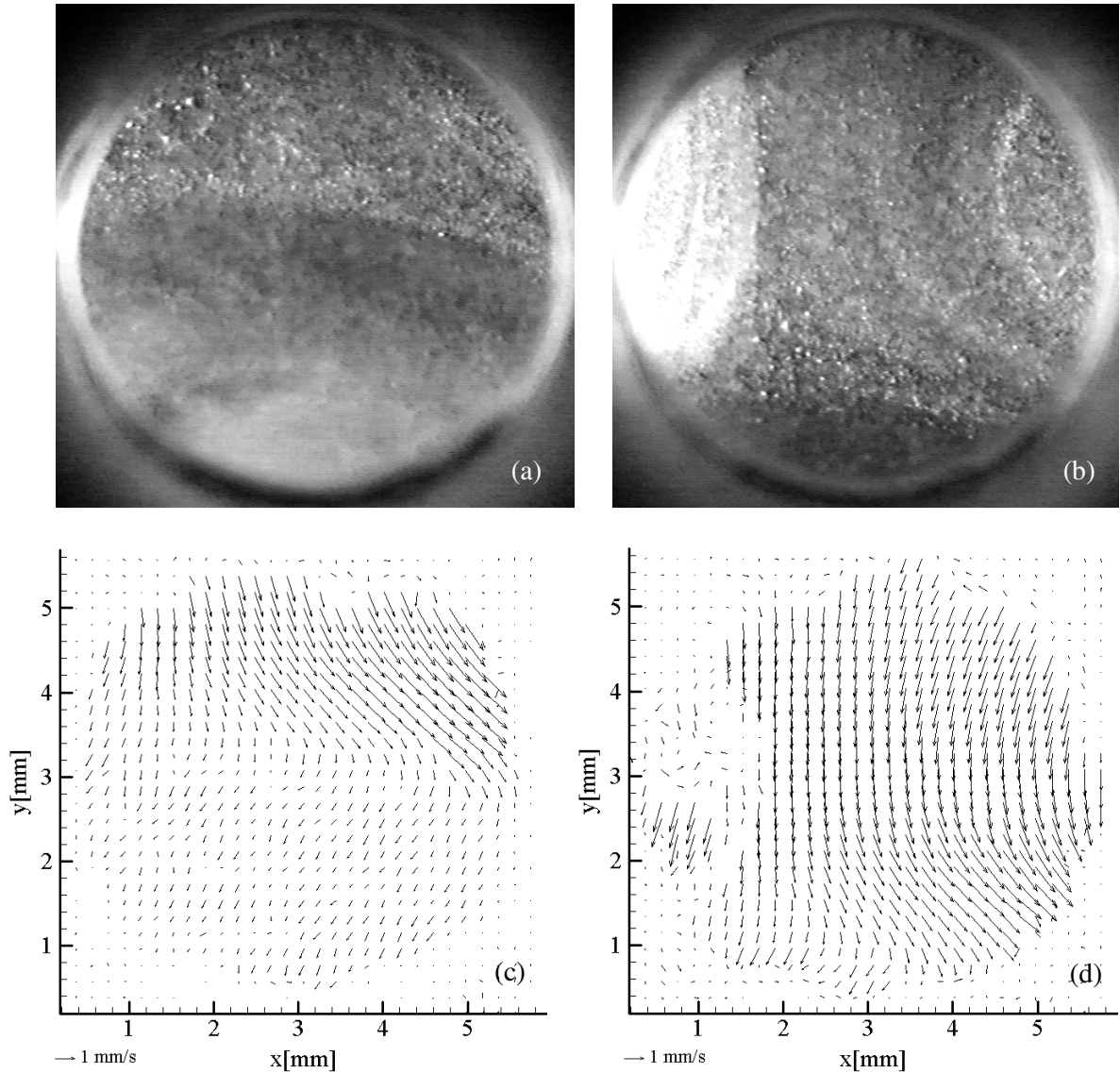


Figure 4.26: Images and PIV results from PST of ice V (a) - (c) $t^* = 0.68$, (b) - (d) $t^* = 0.82$.

With the increasing interest to HPP, ice V is also under investigation concerning more its physical properties. A recent study (Luscher, 2005) focused on its use and application in biological systems, too. According to their results, freezing to ice V is comparable to conventional freezing and showed less destructive effects than conventional freezing and freezing to ice I.

Solid-solid phase changes between different ice types are also given in Figure 4.24. For this experiment, pressure is increased in the cell with a higher rate (almost five times higher). And at this process conditions directly ice I-ice III and ice V solid-solid phase transitions occur, during the process always solid phase is visualized in the cell with slight appearance changes in the opacity of ice. Noticeably, the reverse process starting from ice V is given in study of Urrutia Benet *et al.* (2004) and definitely the same temperature-pressure behavior is observed. Relatively fast pressure release and respectively increase cause the sample to follow a different freezing/thawing characteristic. This characteristic is reported as melting curve of ice V related with its known metastability. Further investigation of these visual properties would give promising information for this concept.

Another ice formation which occurs close to ice V region is ice VI and there is a study that reports the advantages of ice VI in freezing of meat. Even ice VI is not in scope of the work, it is necessary to know that ice VI freezing has some clear advantages over classical ice I freezing. Ice VI freeze-substitution microscopy showed no traces of structural alteration on muscle fibres compared with the damage caused by ice I freezing (Molina-Garcia *et al.* 2004). Further research dealing ice V phase change processes seem to be promising to discover its advantages in food processing.

4.4 Discussion

In this section a general overview for all the processes will be presented to give a comprehensive explanation as well as to be able to compare important parameters for different processes. As convective field calculations being an important part of the results, first of all, the maximum velocity values in the cell for solid (ice) and for fluid (water) are presented for all processes (Figure 4.27). For ice I, in case of pressure shift thawing (PST), higher velocities occur for fluid and solid phase in the cell, in comparison to pressure assisted thawing (PAT) process. The difference in solid velocities is the highest for ice I when PST and PAT processes are compared (Figure 4.27b). In case of PAT ice motion starts after solid is separated from the inner wall surface. Whereas for PST, when the cell is subjected to pressure ice detaches itself immediately from the cell wall. Under this sudden change it starts to move with an accelerated rate compared to PAT. As process and pressure increase, velocity of ice continues to increase moderately (from 0.7 to 1.2 mm/s). This increase is also observed

for PAT (from 0.5 to 0.7 mm/s) but more slightly due to the lack of forced convection in the cell. A similar behavior is noticeable for ice V phase changes even with greater differences. Since the direction of gravity enhances the motion, its effect together with pressure creates more significant increase in velocities.

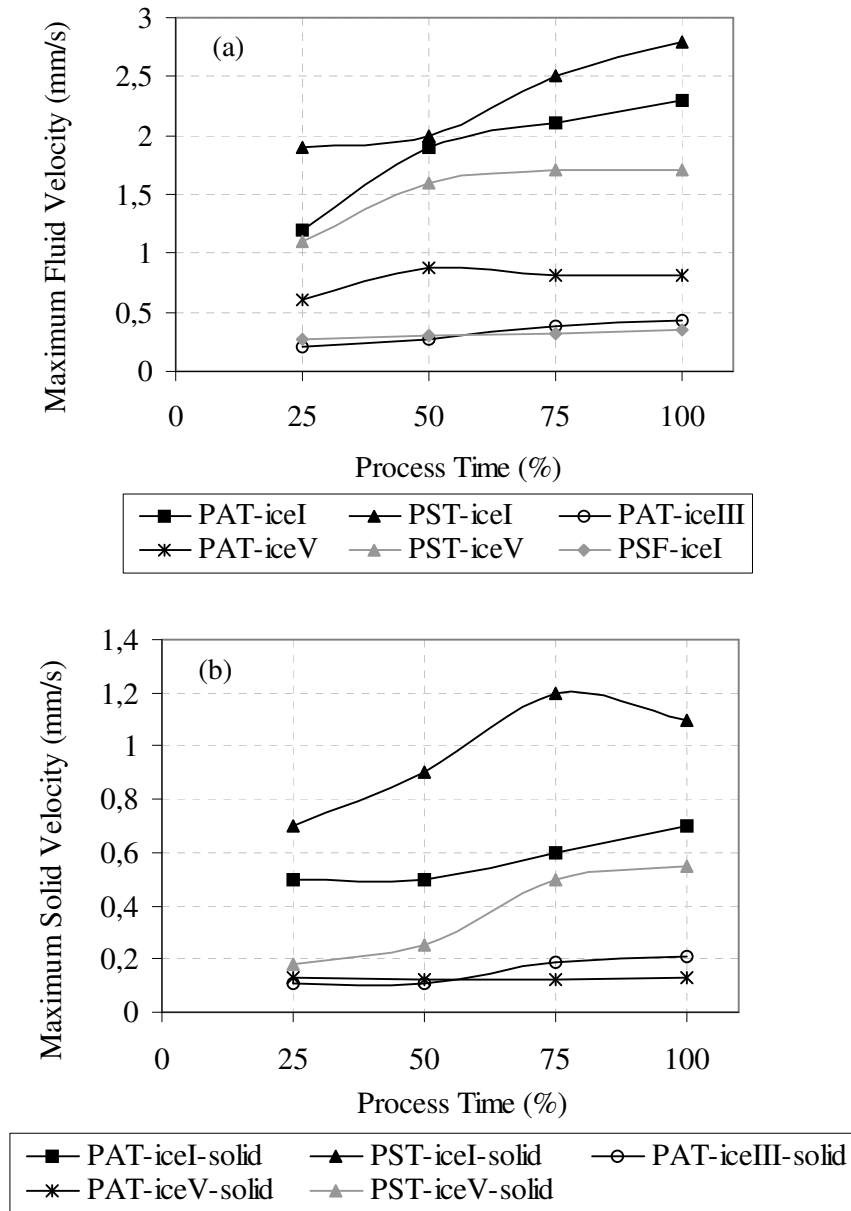


Figure 4.27: Maximum velocity values for all processes (a) for water (b) for ice.

A comparison of processes is performed concerning also other fluid-dynamical parameters which are discussed for each process separately. The shear rate does not exhibit a considerable alteration for all sequences and has an order of magnitude of 10^{-3} (1/s). Only for

PSF to ice I, there is ten fold decrease in shear rate values. Within PAT of ice I, ice III and ice V, minimum shear rates belong to ice III and ice V. Although the shear rate stays under critical values, a two fold difference is distinguished between PAT and PST processes and ice I and ice III-V processes as well. A similar relation is also recognized for strain rate values during the processes. Except PSF, all applications have values in the same order of magnitude and the highest measurements are for PAT and PST of ice I, as shear rate values for PST having two times greater values than that for PAT.

By means of experimental temperature values, local heat transfer is further investigated by an attempt to calculate Nusselt number for the heat change surface of ice layer and water in the cell. Nusselt number is actually the dimensionless temperature gradient between ice-water layer. To calculate Nu number experimentally, first, the heat flux released by latent heat in one second of the process is determined. The volume of ice that changes into water in one second of the process is approx. 0.45 g/s for PST and the temperature difference between ice and water, assuming that ice keeps the initial temperature as at the beginning of the process, is $\Delta T = 3 \text{ }^{\circ}\text{C}$ ($T^* = 0.96$). According to the approach presented in literature (see for example Jischa,1982), Stanton number should be first evaluated to reach Nu number. Related equations can be seen in Table A.6 in Appendix C. For pressure shift thawing Nu number is found as 3.9. For free convection case, Nu number is calculated as a function of Pr and Gr. It has to be also assumed that there is adiabatic conditions at the walls, to calculate the Nu number only between ice and water. By using this approach Nu is found as 2.3 for PAT of ice I. Predictably, higher velocities in the fluid enhances the convective heat transfer in the system and therefore higher Nu number can be observed for the flow caused by forced convection. It can be concluded that the dimensionless temperature gradient between ice and water is more developed in case of PST process. Nu number is once more calculated for the same system under atmospheric pressure by replacing physical properties under high pressure with the ones under atmospheric pressure and a Nu number of 1.3 is obtained for PST process. Nu number for $p^* = 0.13$ is 3.9 and for $p^* = 0.0001$ is 1.3, which can depict an enhanced convective transport mechanism under high pressure. Nu numbers are compared with the work of Kowalczyk (2004) and good agreement is found ($Nu=3.6$). Actually alteration of physical properties of water is decisive in controlling all transfer mechanisms in systems. Whereas, these properties reveal different alterations under high pressure. Although there is still an indefiniteness concerning the final effect, studies emphasize a tendency in concluding that the better transfer mechanisms are obtained under high pressure.

Regarding other flow parameters, vortex in fluid region have the minimum magnitude for ice III and ice V PAT processes. For PAT and PST processes of ice I, unpredictably PAT results in approximately two times higher vorticity values than PST. This maximum value does not belong to the whole sequence but only the last moments which velocity has maximum values. When the dissipation is compared for all sequences, PSF depicts the minimum values, than ice III and ice V processes, consecutively. The maximum values of dissipation is observed for PAT of ice I, PST of ice I and ice V.

Although shear and strain rates do not exceed critical values of these processes (section 4.2.1), the final effect can be discussed concerning biological cells and structures. Some experiments carried out about the influence of phase change under high pressure on cell membrane structure of potato tissues (Schlüter, 2004). It is seen that different process times and temperatures may cause deterioration of the membranes. Freezing and thawing result in stronger membrane disintegration than high pressure alone. Higher membrane damage led probably to a higher release of autolytic enzymes, which increased the rate of reaction as well. The duration of the phase transition and the volume change of water have been found decisive factors on membrane structure. It has been concluded that a phase change with volume decrease (formation of ice III and V) is less destructive for cellular membranes than with volume increase. Even if the system under investigation seems not to have critical effects on biological structures, its potential should be investigated further.

The crucial effect of process parameters under high pressure can be better recognized on protein structures as building elements of enzymes and biological structures. Structural rearrangements taking place in proteins under pressure are governed by the Le Chatelier Principle, which says that processes associated with a volume decrease are encouraged by pressure, whereas processes involving a volume increase are inhibited by pressure (Knorr, 1999). Covalent bonds are almost unaffected by high pressure and so the primary structure of proteins will remain intact during pressure treatment. Secondary structure changes occur at pressure above 300 MPa, which might be explained by the rupture of hydrogen bonds (Knorr, 1999). Irreversible reduction of catalytic potential of enzymes is caused by high pressure. Whereas, it is also observed that enzymes may also be stabilized by pressure against thermal attack. A typical denaturation kinetics of an enzyme (β -amylase) can be seen in Figure 4.28. As the curve demonstrates, it is not straightforward to find an optimum p - T condition to control activity of enzymes, respectively structure of proteins.

Possibly the reaction kinetics and denaturation of proteins are sensitive as well at lower temperatures. Under these circumstances it would create important alterations to have even infinitesimal changes in pressure and temperature. Therefore, even local changes that can be caused from flow mechanical properties play an important role on process effectiveness.

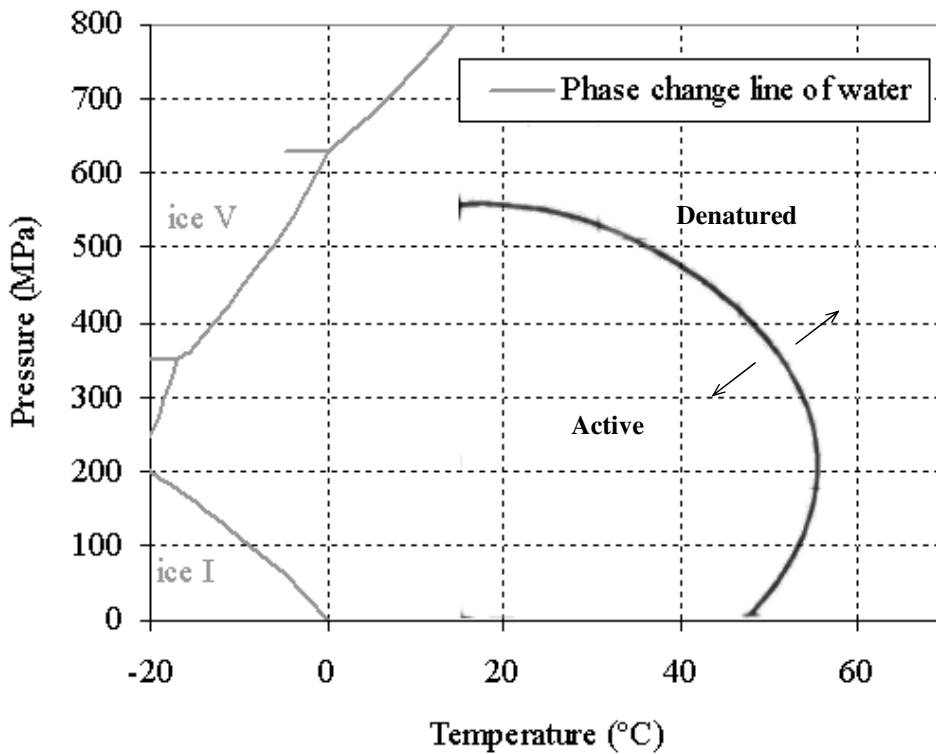


Figure 4.28: Denaturation kinetics of proteins under high pressure and phase change diagram of water (courtesy of Heinz, 2005)

During low temperature processing destructive effect of additional concepts is unavoidable. As it is discussed, the most of the damage that a plant tissue is faced with is cracking upon freezing. Although advantages of freezing under high pressure are proved in many studies (see section 1.1), there are still points to be cleared. As it is also investigated by Lévy *et al.* (1999), light microscopy results of freezing shows that fast rate pressure freezing causes more uniform ice structure in oil-in-water emulsion systems. Although freezing by pressure release should promote fast and uniform nucleation even in samples of larger diameter, it remains to be investigated whether the characteristics of ice crystals (small size, round form, lack of specific orientation) could be maintained in large frozen samples, due to the slower removal of the latent heat of crystallization and the risk of recrystallization in the central parts of the samples.

5 CONCLUSION AND FUTURE ASPECTS

High pressure (HP) treatment of food has substantially broadened the range of possibilities for food processing and product development (e.g. Knorr, 1996, 1999; Butz *et al.* 1997). This emerging technology provides a product-sensitive treatment of raw materials and results in a better final product quality as compared with the conventional methods of heat treatment. Increasingly over the last decades HP has found application in the areas of enzyme inactivation, pasteurization, microbial inactivation and phase transitions in biological systems.

In this study, phase change processes of water under high pressure were investigated. The goal was to analyze the fluid-mechanical characteristics of the system and their interactions thermodynamically. To aid in the visualization of the process, thermo-liquid crystals (TLC) were used as temperature indicators but also served as tracer particles. The use of TLC under high pressure was first applied by Pehl *et al.* (1999). In this study, the method was further developed and successfully applied to phase change processes, as well. It is known that the wavelength of the reflected light shows opponent changes when TLC are subjected to variations in temperature and pressure separately. Therefore, the characteristic temperature pressure relationship for a given TLC should be specifically analyzed for each individual system. By means of characterization experiments, it was established that the light reflective property of TLC is suitable for use under high pressure. The TLC needed to be calibrated at different temperatures and pressures in order to convert the color information to the corresponding temperatures. According to the calculated margin of error of this method, use of TLC for such a system was found to be effective. The difficulties associated with the practical application of TLC as a tool in the observation of this type of system must be considered on a case-by-case basis. Additionally, the exact structure of TLC in an ice matrix should be further investigated. In this study, it was assumed that the TLC are not subjected to any structural changes after the ice matrix, which could affect the reflective properties of the TLC.

The apparent advantages reported in literature (e.g. Kanda and Aoki, 1992; Fuchigami *et al.* 1998; Koch *et al.*, 1996; Knorr *et al.*, 1998) about phase change processes under high pressure served as the motivation to further investigate these processes and water was selected due to its role as the most important component of many foods. The method proved to be suitable for

the use for solid-liquid systems under high pressure. The method offers the advantage of allowing an analysis of the convective and thermal changes in the system. The PIV method was employed to generate 2D velocity information, which was used to create velocity profiles. Additional parameters were also calculated using this 2D velocity information, which were necessary in order to provide a clearer picture of the system.

According to results from the convective fields and temperature fields, differences between the distinct phase change processes were observed. One of the primary observations was the detection of interaction between solid and liquid motion during the processes. The solid phase can be distinguished and its motion analyzed with PIV independently from the liquid phase. This contribution concerning an experimental application under high pressure is presented for the first time in the literature. The motion of the solid phase was observed to be a determining parameter in the fluid flow and was directly affected by application of pressure. Its velocity as a solid body increased in the vicinity of pressure and it created different convective and thermal field properties in the liquid. The fluid region consists of different areas with distinct flow properties. During pressure assisted thawing (PAT) as well as pressure shift thawing (PST) processes, stagnation and extensional flow characteristics were observed. Additionally, in PST processing, vortices were formed during thawing. Although this convective behavior was expected to have a positive effect on heat transfer in the system, larger temperature differences were observed in the temperature field. When the process is carried out under constant pressure (PAT), the temperature profile in the cell demonstrated almost a homogeneous behavior. However, in the case of pressure controlled process (PST), the temperature differences were more substantial during the process. This brings to the fore the concept of the “homogeneous effects of high pressure”, once again. Inhomogeneity concept was introduced for the first time by Delgado and Hartmann (2002), regarding experimental results and theoretical considerations. If inhomogeneity would be a factor considering the small sample volume of 2 ml, then this phenomenon would still require further investigation into applications using larger volumes and dimensions.

Dimensional analysis was carried out in order to create a mathematical description of the system. The importance of each single term and their relationships to one another were able to be observed by analyzing equations representing the processes. In this manner, continuity, momentum and energy equations were set up and rearranged according to the requirements of the different processes, which included pressure assisted thawing (free convection) and

pressure shift thawing (forced convection). These equations are represented in dimensionless form in order to aid in the analysis of the system and to lend a more global approach to the process. Dimensionless numbers such as Reynolds, Froude, Eckert, Prandtl, Stephan, Grashof, Archimedes and Nusselt were determined for the system.

Dimensional analysis revealed the important convective transport parameters associated with these processes. Although the concept of turbulence has neither been investigated nor explained for high pressure systems so far, according to the Re numbers for all of the processes, the flow type can be described as laminar, because it does not exceed the range defined for free stream flow. In the case of low Re numbers, the inertial forces do not dominate the viscous mechanism of momentum transfer. Again, it should be noted that the application of these processes in larger dimensions, as well as the analysis of the parameters on large-scale high pressure processes, require further investigation.

The contribution of frictional stresses in the momentum equation described by dimensionless groups (Ec/Re , Ec/Fr , Ec/Ste), as well as the contribution of viscous dissipation and the conversion of kinetic energy to thermal energy in the energy equation, have proven to be negligible for infinitesimal fluid velocities. Thermal conduction and contribution of gravitational forces should also be considered in reference to the frictional stresses. Although fluid velocities reached higher levels in the pressure shift processes, they did not cause viscous or frictional factors to have more influence over the process as compared with other factors. The contribution of the momentum brought by the temperature and pressure changes was found to be significant.

The convective field analysis was further used to determine other flow parameters of the system. Through the aid of 2D velocity information, shear rate, strain rate, vorticity and dissipation terms were calculated. As a result, different flow regions were able to be differentiated and subsequently better characterized. The interaction between solid and fluid phases and their effects on flow field have been emphasized once more. The effects of these factors on the sensory qualities of biological tissue was partly answered by comparing with the critical limits for a biological tissue.

Phase change processes are also one of the primary subjects in numerical simulation (e.g. Kowalczyk *et al.*, 2004; Voller *et al.*, 1989), which provides indispensable information about a process through enabling to use different process parameters and conditions. Although the moving boundary characteristic of the system posed a difficulty to simulate, current effort to

develop these techniques may render simulation of the system possible. Then, this thesis could serve as an important source of data for a simulation attempt.

High pressure treatment possesses a great potential for food production, biotechnology and even presents applications in medicine (pharmaceutical). In the area of food technology, products processed using high pressure have already found their place in food market. Specifically, phase change processes under high pressure promise to promote sensory and safety aspects of food products. Successful utilization of this technology in a practical setting in the food industry is contingent upon how well understood the behavior of the processes become. This represents an important contribution to a more precise understanding of the primary transfer mechanisms which are at the root of high pressure phase change processes. Possible directions for future research would be the in-situ analysis of high pressure processes using larger sample volumes as well as experimentation with different materials other than water. Another area for further investigation could be analyzing phase change processes in mixtures or in two phase systems. There has been some research concerning the effects of pressure on emulsion systems. In the future, this kind of research could provide new methods for emulsion processing in the food industry.

As previously mentioned, effect of pressure on protein structures is still an area under investigation (e.g. Huppertz *et al.*, 2002; Heremans and Smeller, 1998). Not only do the structure of proteins undergo change but as a product of this change, their functionality as well. Furthermore, these alterations can serve as a new tool in functional food production. High pressure technology can be utilized to design functional foods which are designed to provide a specific and beneficial physiological effect on health, performance or well-being extending beyond the provision of simple nutrients.

In the realm of biotechnology high pressure already serves as an important tool for controlling inactivation mechanisms, but it may also find application in increasing product yield and improved process effectiveness. For medical applications, the basic use of high pressure lies in conserving animal tissues at low temperatures. Moreover, important functional changes observed on cancer cells subjected to pressure treatment have recently been reported. High pressure offers not only possibilities for developing new processing techniques for the food industry and in biotechnology but also opens new areas of research into human health and disease prevention.

6 APPENDICES

APPENDIX A

Table A.1: Commercial products produces with High-Pressure Processing

<i>Product</i>	<i>Company</i>	<i>Since</i>
Orange juice	UltiFruit®, Pernord Richard Company, France	1995
Acidified avocado purée and salsa	Avomex Company, TX, USA	1997
Sliced ham (cured-cooked and raw-cooked)	Espuna Company, Spain	1998
Oysters, clams, mussels, scallops, shrimp, crabs and crab meat	Motivatit Sea Foods, Inc., Houma, LA, USA	1999
Citrus fruit juice, vegetable juice, beverage blends	Fresh Samantha, Inc. & Odwalla, USA	discontinued
Ruby red orange juice	Ortogel SRL, Italy	
apple, strawberry, and pineapple jams*	Pascal Foods, Japan	1992
rice cake, hypoallergic and single-portioned cooked rice		1995

* the first commercialized high pressure processed foods in the world

Table A.2: Thermodynamic properties of the phase transitions of water (Kalichevsky *et al.*, 1995). T is transition temperature, p is transition pressure, Δv is volume change and Δh is enthalpy change.

Phase transition	T (°C)	p (MPa)	Δv (cm ³ /g)	Δh (kJ/kg)
Liquid---ice I	-20	193.3	+0.1313	-241
	-15	156.0	+0.1218	-262
	-10	110.9	+0.1122	-285
	-5	59.6	+0.1016	-308
	0	0.1	+0.0900	-334
Ice I---Ice III	-30	211.5	-0.1919	+14.6
	-20	206.3	-0.1773	+23.4
Ice III---Ice V	-25	341.1	+0.0546	-3.64
	-20	345.5	+0.0547	-3.72
Liquid---ice III	-22	207.5	-0.0466	-213
	-20	246.2	-0.0371	-226
	-17	346.3	-0.0241	-257
Liquid---ice V	-20	308.0	-0.0828	-253
	-15	372.8	-0.0754	-265
	-10	442.4	-0.0679	-276
	-5	533.7	-0.0603	-285
	0	623.9	-0.0527	-293
Liquid---ice VI	-10	518.0	-0.0960	-264
	0	623.9	-0.0916	-295
	10	749.5	-0.0844	-311
	20	882.9	-0.0751	-320
	30	1038.9	-0.0663	-330

APPENDIX B

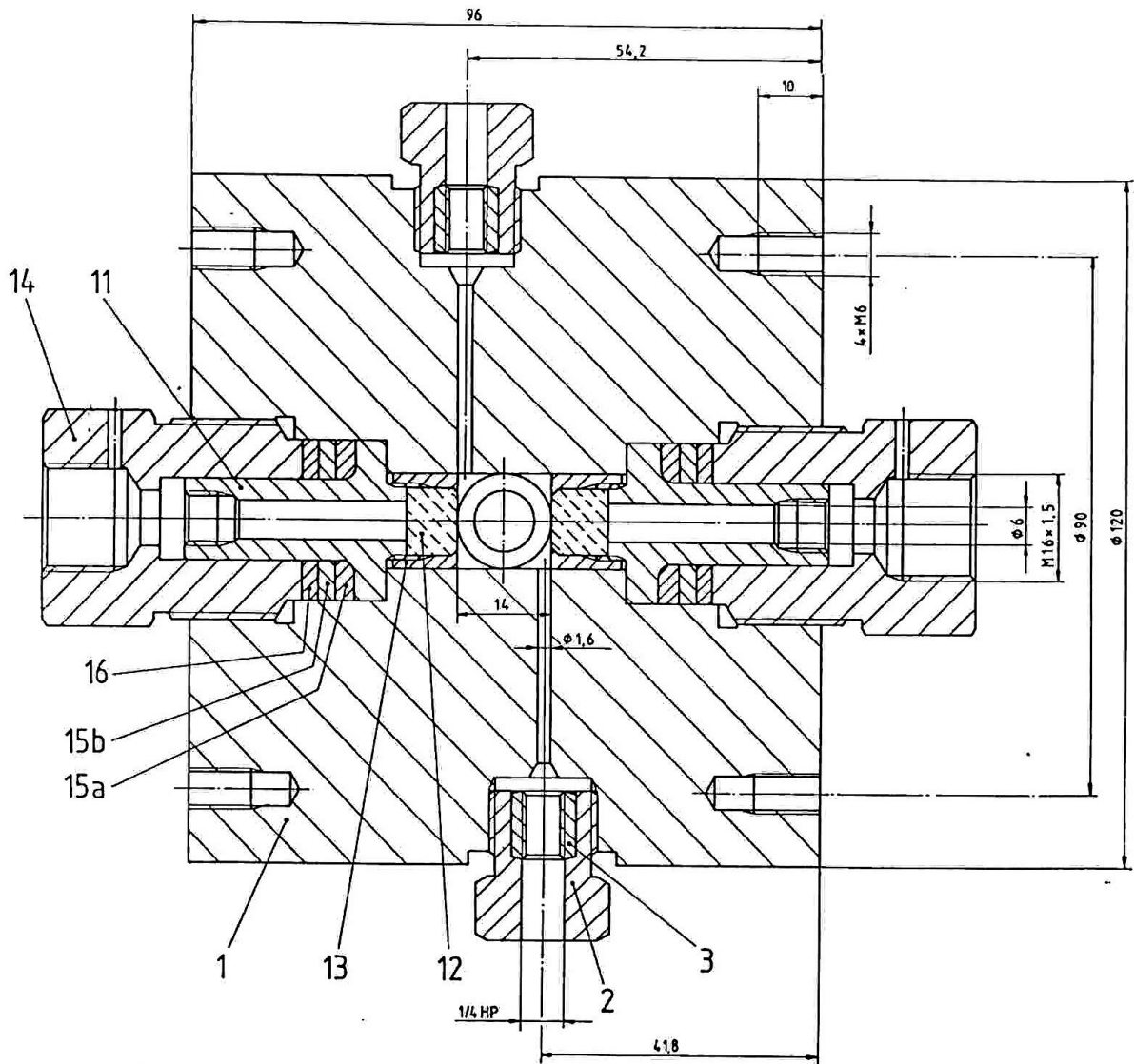


Figure A.1: Technical drawing of high pressure cell (SITEC Sieber Engineering AG)

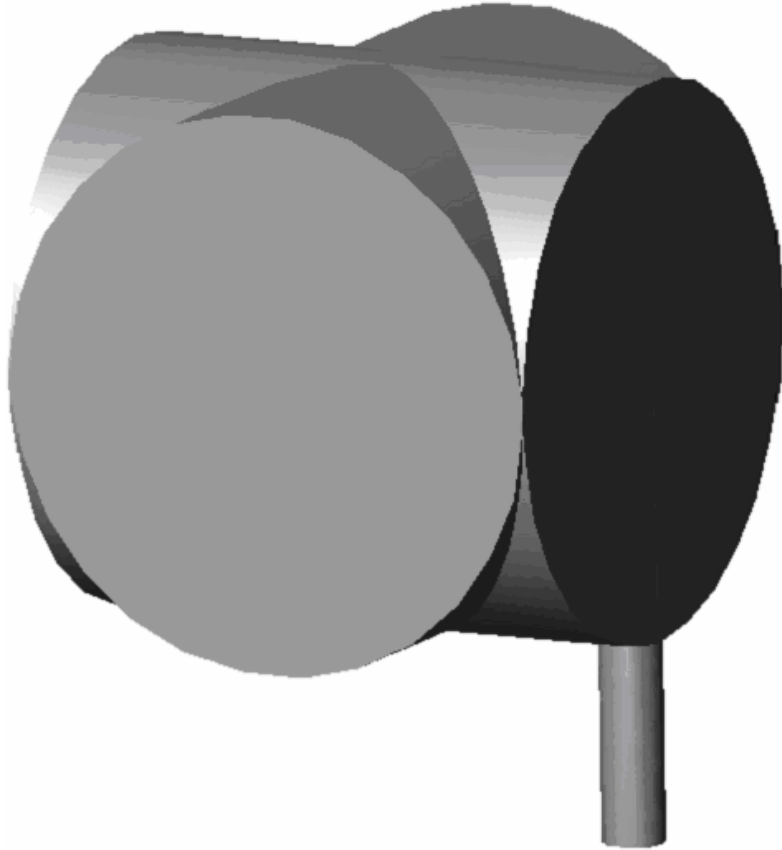


Figure A.2: 3D geometrical representation of the high pressure chamber (inside the cell)

APPENDIX C

Table A.4. Dimensionless variables used in non-dimensionalization.

Property	Dimensionless form
Density	$\rho^* = \frac{\rho}{\rho_0}$
Time	$t^* = \frac{t U_0}{L_0}$
Distance in x and y coordinates	$x^* = \frac{x}{L_0}, y^* = \frac{y}{L_0}$
x, y components and solid velocity	$U_{x,z,s}^* = \frac{U_{x,z,s}}{U_{x,z,s0}}$
Dynamic viscosity	$\mu^* = \frac{\mu}{\mu_0}$
Gravitational acceleration	$\vec{g}^* = \frac{\vec{g}}{g_0}$
Pressure for momentum	$p^* = \frac{p}{\rho_0 U_0^2}$
Pressure for energy	$p^* = \frac{p}{\rho_0 c_{p0} T_0}$
Temperature	$T^* = \frac{T}{T_0}$
Temperature (crystallization)	$\Theta^* = 1 - \frac{T_c}{T_0}$
Enthalpy	$h^* = \frac{h}{c_{p0} T_0}$
Thermal conductivity	$\lambda^* = \frac{\lambda}{\lambda_0}$
Liquid mass percentage	$f_1 = f_1^*$

Property	Dimensionless form
Crystallization enthalpy	$\tilde{H}^* = \frac{\tilde{H}}{L_f}$
Volume of solid	$V^* = \frac{V}{V_0}$
Mass of solid	$m_s^* = \frac{m_s}{m_{s0}}$
Surface area of solid	$A^* = \frac{A}{A_0}$

Table A.6. Calculation of Nusselt number.

	Pressure Assisted Thawing	Pressure Shift Thawing
P (MPa), T (°C)	138 , -13	145 , -9
\dot{m} (kg/s)	0.14×10^{-3}	0.45×10^{-3}
$q = \dot{m} \cdot L$ (J/m ² s)		40
$Nu = \frac{h.L}{\lambda}$	$Nu = \frac{0.676 Pr^{1/2}}{(0.861 + Pr)^{1/4}} \cdot (Gr/4)^{1/4}$	$St = \frac{Nu}{Re \cdot Pr}$, $St = \frac{q}{\rho \cdot c_p \cdot \Delta T \cdot U_0}$
Nu	2.3	3.9

APPENDIX D

All experiments are replicated and corresponding Temperature-Pressure (T-p) relations are analyzed to see if they have the same behaviour for all experiments. For this aim an equation is fitted to T-p curves. Then residuals between actual temperature values and the values obtained according to this equation are calculated. A Normal Distribution Test is applied to prove that residuals are normally distributed around zero. Quantile value (χ_i) of standard-normal distribution is determined by the relationship $\chi_i = \phi^{-1}\left(\frac{i-3/8}{n+1/4}\right)$. Hereby, ϕ^{-1} is the inverse cumulative of the normal distribution function and n is the sample size. Correlation (r) between residuals and ϕ^{-1} is calculated and compared with the critical correlation (r_{cr}). The hypothesis of normal distribution is proved when $r > r_{cr}$. In Table A.7 r and r_{cr} values can be seen at a significance level of $\alpha = 0.01$ and for different processes. The type of relation between temperature and pressure is also given in the table.

Table A.7. Normal Distribution Test results for residuals. Hypothesis: Residuals are normally distributed around zero ($\mu = 0$), TRUE/ FALSE

Process	r	$r_{cr} (\alpha=0.01)$
PST-ice I	0.978824	0.962702-TRUE
linear (lnT-p)	0.984146	0.962702-TRUE
	0.972125	0.956053-TRUE
	0.975030	0.960491-TRUE
	0.983988	0.975366-TRUE
	0.983038	0.976805-TRUE
	0.973352	0.972398-TRUE
	0.974977	0.971328-TRUE
	0.988571	0.978244-TRUE
	0.985372	0.976913-TRUE
PAT-ice I	0.976854	0.951854-TRUE
polynomial (3 rd order)	0.977551	0.966423-TRUE
(T-p)	0.980154	0.969524-TRUE
	0.978232	0.974115-TRUE
	0.974598	0.972498-TRUE
	0.978944	0.977416-TRUE
	0.981228	0.966423-TRUE

Process	r	r _{cr} ($\alpha=0.01$)
PAT-ice III	0.969425	0.963054-TRUE
polynomial(2 nd order)	0.970056	0.968412-TRUE
(lnT-p)	0.968514	0.962088-TRUE
	0.971284	0.970664-TRUE
PAT-ice V	0.988406	0.982614-TRUE
linear (lnT-p)	0.971674	0.962106-TRUE
	0.963641	0.952879-TRUE
	0.976613	0.968261-TRUE
PST-ice V	0.961795	0.956104-TRUE
linear (lnT-p)	0.976218	0.968261-TRUE
	0.961562	0.957442-TRUE
	0.974461	0.972103-TRUE

As it is mentioned in section 4.3, the velocity values for different experiments are compared considering maximum velocities. Table A.8 shows average maximum fluid velocities for the sequences given in Table A.7.

Table A.8. Average maximum fluid velocities for all sequences.

Process	Average Maximum Velocity(mm/s)	Standard deviation
PST-ice I	2.62	0.077
PAT-ice I	2.29	0.084
PSF-ice I	0.37	0.072
PAT-ice III	0.39	0.059
PAT-ice V	0.77	0.035
PST-ice V	1.64	0.072

7 REFERENCES

- Akino N, Kunugi T, Ueda M, Kurosawa A. (1989). A study on Thermo-Camera Using a Liquid Crystal. In: *ASEM Heat Transfer Measurements*, Shah, R.K.(ed.), 112, 115-122.
- Akyurt, M., Zaki, G., Habeebullah, B. 2002. Freezing phenomena in ice–water systems. *Energy Conversion and Management*, (43),1773-1789.
- Bauer, B.A., Hartmann, M., Sommer, K., Knorr, D. 2004. Optical in situ analysis of starch granules under high pressure with a high pressure cell. *Innovative Food Science & Emerging Technologies*, (5), 293-298.
- Bird, B.R., Stewart, W.E., Lightfoot, E.N. (1960). *Transport Phenomena*, John Wiley and Sons, Inc. Singapore.
- Brodkey, R.S., Hershey, C. (1988). *Transport Phenomena: A Unified Approach*, McGraw-Hill, Inc. Belfast.
- Buchheim, W., Frede, M., Wolf, M., Baldeegger, P. (1999). Solidification and melting of some edible fats and model lipid systems under pressure. In: *Advances in High Pressure Bioscience and Biotechnology*, Ludwig, H., ed., Springer Verlag, Heidelberg, 153-156.
- Butz, P., Tausher, B. (1997). High pressure treatment of fruit and vegetables: problems and limitations. In: *High Pressure Research in Biosciences and Biotechnology*, Ed. By K. Heremans, Belgium, 435-437.
- Butz, P., Tausher, B. (2002). Emerging Technologies: chemical aspects. *Food Research International*, (35), 279-284.
- Chaplin M. (2004). Internet site <http://www.lsbu.ac.uk/water/>
- Cheftel, J.C., Lévy, J., Dumay, E. (2000). Pressure-assisted Freezing and Thawing: Principles and potential applications. *Food Reviews International*, (16) 4, 453-483.

REFERENCES

- Chevalier, D., Le Bail, A., Chourot, J.M., Chantreau, P. (1999). High pressure thawing of fish (whiting): influence of the process parameters on drip losses. *Lebensmittel-Wissenschaft und Technologie*, (32), 25-31.
- Chevalier, D., Sequeira-Munoz, A., Le Bail, A., Simpson, B.K., Ghoul, M. (2000). *Lebensmittel-Wissenschaft und Technologie*, (33), 570-577.
- Chevalier, D., Sequeira-Munoz, A., LeBail, A., Simpson, B.K., Ghoul M. (2000b). Effect of Freezing Conditions and Storage on Ice Crystal and Drip Volume in Turbot (*Scophthalmus maximus*). Evaluation of Pressure Shift Freezing vs. Air-blast freezing. *Innovative Food Science and Emerging Technologies*, (1-3), 193-202.
- Chevalier, D., Le Bail, A., Ghoul, M. (2000). Freezing of ice crystals formed in a cylindrical food model: part II. Comparison between freezing at atmospheric pressure and pressure-shift freezing. *Journal of Food Engineering* (46), 287-293.
- CSIRO (Commonwealth Scientific and Industrial Research Organization) (2002). *Media Release*, Ref 2002/110, Jun 19.
- Delgado, A., Hartmann, C. (2002). Pressure Treatment of Food: Instantaneous but not Homogeneous Effect. In: *Advances in High Pressure Bioscience and Biotechnology II*. (Edited by R.Winter) *Proceedings of the 2nd Int. Conf. On High Pressure Bioscience and Biotechnology* (Dortmund), Springer, Heidelberg.
- Denys, S., Van Loey, A., De Cordt, S., Hendrickx, M., Tobback, P. (1997). High Pressure Research in the Bioscience and Biotechnology. In: *Modelling of High Pressure Assisted Freezing and Thawing*, (Edited by K. Heremans), Leuven University Press, 351-355.
- Denys, S., Van Loey, A., Hendrickx, M.E. (2000). Modelling Conductive Heat Transfer during High-Pressure Thawing Processes: Determination of Latent Heat as a Function of Pressure. *Biotechnology Progress*, (16), 447-455.
- Deuchi, T., Hayashi, R. (1992). High pressure treatments at sub-zero temperature: application to preservation, rapid freezing and rapid thawing of foods. In : *High Pressure and Biotechnology*, Balny C., Hayashi R., Hermans K., Masson P. (eds.), John Libbey and Co. Ltd., London, 353-355.

REFERENCES

- Evans, L.F. (1967). Selective Nucleation of the High-pressure Ices. *Journal of Applied Physics*, (38), 4930-4932.
- Först, P., Werner, F., Delgado, A. (2000). The viscosity of water at high pressures-especially at subzero degrees centigrade. *Rheol Acta*, (39), 566-573.
- Fuchigami M., Kato N., Teramoto A. (1998). High-pressure-freezing effects on textural quality of Chinese cabbage. *J. Food Sci.*, 63, 122-125.
- Gui, L. (1997). Ph.D. Thesis: *Methodische Untersuchungen zur Auswertung von Aufnahmen der digitalen Particle Image Velocimetry*, Universität GH Essen.
- Hartmann C., Delgado, A. (2002a). Numerical Simulation of Thermodynamic and Fluid-dynamic Processes During the High Pressure Treatment of Fluid Food Systems. *Innovative Food Science and Emerging Technologies*, (3), 11-18.
- Hartmann, C., Delgado, A. (2002b) Numerical simulation of convective and diffusive transport effects on a high-pressure-induced inactivation process. *Biotechnology and Bioengineering*, (79-1), 94-104.
- Hartmann C., Delgado, A. (2003). Numerical Simulation of the mechanics of a yeast cell under high hydrostatic pressure. *Journal of Biomechanics*, (37), 977-987.
- Hartmann C., Schuhholz, J., Kitsubun, P., Chapleau, N., Le Bail, A., Delgado, A. 2004. Experimental and numerical analysis of the thermofluidynamics in a high-pressure autoclave. *Innovative Food Science and Emerging Technologies*, (5), 399-411.
- Hayashi, R. (1997). High Pressure Bioscience and Biotechnology in Japan. *High Pressure Biosciences and Biotechnology*, K. Heremans (Ed), Leuven Uni Press, 1-4.
- Hayashi, R. (2002). High Pressure in Bioscience and Biotechnology: Pure Science Encompassed in Pursuit of Value. *Biochimica et Biophysica Acta* (1595), 397-399.
- Heinz, Volker (2005) Personal Communication.
- Heremans, K., Smeller, L. (1998). Protein structure and dynamics at high pressure. *Biochimica et Biophysica Acta - Protein Structure and Molecular Enzymology*, (1386), 353-370.

REFERENCES

- High Pressure Diamond Optics (2003). Internet Site: <http://www.hpdo.com/intro.html>
- Hollingsworth, D.K., Hay, J.L. (1998). Calibration of micro-encapsulated liquid crystals using hue angle and a dimensionless temperature. *Experimental Thermal and Fluid Science*, (18), 251-25.
- Huppertz, T., Kelly, A.L., Fox, P.F. (2002). Effects of high pressure on constituents and properties of milk. *International Dairy Journal* (12), 561–572.
- Jischa, M. 1982. „Konvektiver Impuls-, Wärme- und Stoffaustausch“, Vieweg Braunschweig/Wiesbaden.
- Kalichevsky, M.T., Knorr, D., Lillford, P.J. (1995). Potential Food Applications of high-pressure Effects on Ice-Water Transitions. *Trends in Food Science and Technology*, (6), 253-259.
- Reid, D. S. (1998). ISOPOW 6 - The properties of water in foods. London.
- Kanda, Y., Aoki, M. (1992). Development of pressure-shift freezing method: Part I, observation of ice crystals of frozen 'Tofu'. In: *High Pressure Bioscience and Food Science*, HAYASHI R. (ed.), San-Ei Shuppan Co., Kyoto, Japan, 24-26.
- Kapranov, S.V., Pehl, M., Hartmann, C., Baars, A., Delgado, A. 2003 On the Influence of High Pressure on Edible Oils. In: *Advances in High Pressure Bioscience and Biotechnology II*, Winter R., ed, Springer-Verlag, Berlin, 453-457.
- Knorr D., Schlueter O., Heinz V. (1998). Impact of high hydrostatic pressure on phase transitions of food. *Food Technology*, 52, 42-45.
- Knorr, D. (1996). Advantages, opportunities and challenges of high hydrostatic pressure application to food systems. In *High Pressure Bioscience and Biotechnology*, R. Hayashi and C. Balny, eds., Elsevier Science, Amsterdam.
- Knorr, D. (1999). Novel Approaches in Food-processing Technology. *Food Biotechnology*, (10), 485-491.

REFERENCES

- Kowalczyk W., Hartmann C., Delgado A. (2002). Modelling and Numerical Simulation of Pressure Induced Phase Changes of a Fluid Food System, Poster in: *High Pressure Bioscience and Biotechnology*, Dortmund.
- Kowalczyk W., Hartmann C., Delgado A. (2004). Modelling and numerical simulation of convection driven high pressure induced phase changes, *International Journal of Heat and Mass Transfer*, (47-5) 1079-1089.
- Kowalczyk W. (2004) Ph.D. Thesis: *Numerische Simulation thermofluidodynamischer Prozesse bei der Hochdruckbehandlung*, Technische Universität München
- Kowalewski, T.A., Cybulski, A., Rebow, M. (1998). Particle Image Velocimetry and Thermometry in Freezing Water. 8th *International Symposium on Flow Visualization*. Sorrento, Carlomagno, G.M. and Grant, I. (Edts), Edinburgh. 24.1-24.8.
- Krebbers, B., Koets, M., van den Wall, F., Matser, A.M., Moezelaar, R. (2002). Effects of high pressure processing on the quality of green beans. *Trends in High Pressure Bioscience and Biotechnology*. Edited by R.Hayashi, (19), 389-396.
- LeBail, A., Boillereaux, L., Davenel, A., Hayert, M., Lucas, T., Monteau, J.Y. (2003). Phase Transition in Foods : effect of pressure and methods to assess or control phase transition. *Innovative Food Science and Emerging Technologies*, (4), 15-24.
- LeBail, A., Chevalier, D., Mussa, D.M., Ghoul, M. (2002). High Pressure Freezing and Thawing of Foods : a review. *International Journal of Refrigeration*, (25), 504-513.
- Li, B., Sun, D.W. (2002). Novel Methods for Rapid Freezing and Thawing of Foods- A Review. *Journal of Food Engineering*, (54), 175-182.
- Lopez, D., Mendoza-Sanchez, P., Kongraksawech, T., Velazquez de la Cruz, G., Huerta-Ruelas, J., Torres, J.A. (2004). In-situ optical polarization measurements for food processes. In: *IFT Annual Meeting*, Las Vegas (99B-22).
- Luscher, C., Balasa, A., Fröhling, E., Ananta, E., and Knorr, D. 2004. Effect of High-Pressure Ice I-III Phase Transitions on Inactivation of *Listeria innocua* in Frozen Suspension. *Applied and Environmental Microbiology*, (70), 4021-4029.

REFERENCES

- Luscher, C., Schlüter, O., Knorr, D. 2005. High pressure-low temperature Processing of Foods: impact on cell membranes, texture, color and visual appearance of potato tissue. *Innovative Food Science and Emerging Technologies*. Article in Press.
- Martino, M.N., Otero, L., Sanz, P.D., Zaritzky, N.E. (1998). Size and Location of Ice Crystals in Pork Frozen by High-Pressure-Assisted Freezing as Compared to Classical Methods. *Meat Science*, (50-3), 303-313.
- Matser, M.A., Krebbers, B., Robert W., Bartels, P.V. (2004). Advantages of high pressure sterilization on quality of food. *Trends in Food Science and Technology*, (15), 79-85.
- Molina-Garcia, A.D., Otero, L., Martino, M.N., Zaritzky, N.E., Arabas, J., Szczepek, J., Sanz, P. (2004). Ice VI freezing of meat: supercooling and ultrastructural studies. *Meat Science*, (66), 709-718.
- Nozaki, T., Mochizuki, N., Kaji, N., Mori, Y.H. (1995). Application of liquid-crystal thermometry to drop temperature measurements. *Experiments in Fluids*, (18), 137-144.
- Otero, L., Sanz, P. (2000a). High Pressure Shift Freezing. Part 1. Amount of ice instantaneously formed in the process. *Biotechnology Progress*, (16), 1030-1036.
- Otero, L., Molina-Garcia, A.D., Sanz, P. (2000b). Thermal effects in Foods During Quasi-adiabatic Pressure Treatments. *Innovative Food Science and Emerging Technologies*, (1), 119-126.
- Otero, L., Molina-Garcia, A.D., Sanz, P. (2002). Some Interrelated Thermophysical Properties of Liquid Water and Ice I. A User-Friendly Modelling Review for Food High Pressure Processing. *Critical Reviews in Food Science and Nutrition*, (42), 339-352.
- Otero, L., Sanz, P. (2003). Modelling Heat Transfer in High Pressure Food Processing: A Review. *Innovative Food Science and Emerging Technologies*, (4), 121-134.
- Ozawa, M., Müller, U., Takamori, T., Kimura, I. (1992). Flow and temperature measurement of natural convection in a Hele-Shaw cell using a thermo-sensitive liquid crystal tracer. *Experiments in Fluids*, (12), 213-222.

REFERENCES

- Pehl, M., Werner, F., Delgado, A. (2000). First Visualization of temperature fields in liquids at high pressure using thermochromic liquid crystals, *Experiments in Fluids*, (29), 302-304.
- Pehl, M., Delgado, A. (1999). An in-situ technique to visualize temperature and velocity fields in liquid biotechnical substances at high pressure. In: *Advances in High Pressure Bioscience and Biotechnology*, Ludwig, H. (ed), Springer-Verlag, Heidelberg, 519-522.
- Pehl, M., Werner, F., Delgado, A. (2002). Experimental investigation on thermofluidodynamical processes in pressurized substances. In: *Trends in High Pressure Bioscience and Biotechnology*, Hayashi, R. (ed.), Elsevier Sci., 429-435.
- Pehl, M. (2004). PhD Thesis: *In-situ diagnose thermofluidodynamischer Vorgänge in komprimierten Flüssigkeiten*. Technische Universität München.
- Van der Pol, L., Tramper, J. (1998) Shear sensitivity of animal cells from a culture-medium perspective. *Trends in Biotechnology*, (16), 323-328.
- Pollmann, P., Wiege, B. (1978). Selective Light Reflection Measurements on binary Mixtures up to 3000 bar and 130°C. *Molecular Crystals and Liquid Crystals*, 150(b), 375-386.
- Precht, M., Kraft, R. (1993). *Biostatistik 2*, Oldenbourg.
- Raffel, M., Willert, C., Kompenhans, J. (1998). *Particle Image Velocimetry A Practical Guide*. Springer Verlag Berlin Heidelberg.
- Rahman, S. (1995). *Food Properties Handbook*, CRC Press Inc., Florida.
- Reid, D.S. (1998). *The Properties of Water in Foods*. Blackie Academic and Professional, London, 273-420.
- Rouillé, J., Le Bail, A., Ramaswamy, H.S., Leclerc, L. (2002). High Pressure Thawing of Fish and Shellfish. *Journal of Food Engineering*, (53), 83-88.
- Rubens, P., Snauwaert, J., Heremans, K., Stute, R. (1999). In situ observation of pressure-induced gelation of starches studied with FTIR in the diamond anvil cell. *Carbohydrate Polymers*, (39), 231-235.

REFERENCES

- San Martin, M.F., Barbosa Cánovas, G.V., Swanson, B.G. (2002). Food Processing by High Hydrostatic Pressure. *Critical Reviews in Food Science and Nutrition*, 42(6), 627-645.
- Schlüter, O., (2004) Ph.D. Thesis: *Impact of High Pressure -Low Temperature Processes on Cellular Materials Related to Foods*, VDI-Fortschritt-Berichte, Reihe 3, Nr. 802, VDI-Verlag, Düsseldorf.
- Schubring, R., Meyer, C., Schlüter, O., Boguslawski S., Knorr, D. (2003). Impact of high pressure assisted thawing on the quality of fillets from various fish species. *Innovative Food Science and Emerging Technologies*, (4), 257-267.
- Seybert, C.D., Evans, J.W. (2005). PIV Measurements of velocity of water in the presence of ice and comparison with calculated values. *International Journal of Heat and Mass Transfer*, (48), 67-73.
- Shi X., Datta, A.K., Mukherjee, S. (1999). Thermal Fracture in a Biomaterial during Rapid Freezing. *Journal of Thermal Stresses*, (22), 275-292.
- Spurk, J.H. (1997). *Fluid Mechanics*. Springer Verlag, Germany.
- Stasiek, J., Mikielewicz, D., Mikielewicz, J., Collins, M.W. (1997). A new method of heat transfer coefficient measurements by liquid crystal and digital processing. *Trans IChem E*, (75), Part A, 657-662.
- Stasiek, J., Tanda, G. (1999). Heat Transfer Measurements in Heat Exchangers by Liquid Crystal Thermography. *Atlas Mathematical Conference Abstracts*.
- Stichlmair, J. (1990) „Kennzahlen und Ähnlichkeitsgesetze im Ingenieurwesen“ Altos-Verlag Doris Stichlmair, Essen.
- Stipl, V.M., Delgado, A., Becker, T. (2004). Development of a method for the optical in-situ determination of pH value during high-pressure treatment of fluid food. *Innovative Food Science & Emerging Technologies*, (5), 285-292.
- Suzuki,A., (2003). Current development of high pressure processed foods in Japan. *IFT Annual Meeting*, Chicago, 34-7.

REFERENCES

- Ter Minassian, L., Pruzan, P. (1981). Thermodynamic properties of water under pressure upto 5 kbar and between 28 and 120 °C. Estimations in the supercooled region down to -40 °C. *Journal of Chemical Physics*, (75), 6, 3064-3072.
- Tewari, G., Jayas, D. S., Holley, R.A. (1999). High Pressure Processing of Foods: An Overview. *Science Des Aliments*, (19), 619-661
- Thiebaud, M., Dumay, E.M., Cheftel, J.C. (2002). Pressure-shift freezing of o/w emulsions. *Food hydrocolloids*, (16), 527-545.
- Tchijov, V., Baltazar Ayala, R., Cruz León, G., Nagornov, O. (2004). Thermodynamics of high-pressure ice polymorphs: ices III and V. *Journal of Physics and Chemistry of Solids*,(65)1277-1283.
- Torres, J.A., Velazquez, G. (2004). Commercial opportunities and research challenges in the high pressure processing of foods. *Journal of Food Engineering*. Article in Press.
- Urrutia Benet, G., Schlüter, O., Knorr, D. (2004). High pressure–low temperature processing. Suggested definitions and terminology. *Innovative Food Science & Emerging Technologies*, (5), 413-427.
- Voller, V.R, Brent, A.D., Prakash, C. (1989) The modelling of heat, mass and solute transport in solidification systems. *International Journal of Heat and Mass Transfer*, (32-9), 1719-1731.
- Wagner, W., Cooper, J.R., Dittmann, A., Kijima, J., Kretschmar, H.-J., Krause, A., Mareš, R., Oguchi, K., Sato, H., Stöcker, I., Šifner, O., Takaishi, Y., Tanishita, I., Trübenbach, J., Willkommen, T. (s2000). The IAPWS Industrial Formulation 1997 for the Thermodynamic Properties of Water and Steam, *ASME J. Eng. Gas Turbines and Power*, (122), 150-182.
- Wereley, S.T., Gui, L. (2003). A correlation-based central difference image correction (CDIC) method and application in a four-roll-mill flow PIV measurement. *Experiments in Fluids* (34), 42-51.

REFERENCES

- Zhu, S., Ramaswamy, H.R., Le Bail, A. (2005). Ice-crystal formation on gelatin gel during pressure shift versus conventional freezing. *Journal of Food Engineering*, (66), 69-76.
- Zhu, S., Ramaswamy, H.R., Simpson, B.K. (2004). Effect of high pressure versus conventional thawing on color, drip loss and texture of Atlantic salmon frozen by different methods. *Lebensmittel Wiss und Technol.*, (37), 291-299.

ÖZLEM ÖZMUTLU

PERSONAL INFORMATION

- Date & Place of Birth: 10.03.1978, Ankara - Turkey
- Marital status: Single
- Nationality : Turkish

EDUCATION

2002- today	Technical University of Munich (TUM), Germany Chair of Fluid Mechanics & Process Automation, Ph.D. <i>Visualization of Temperature and Velocity Fields During Phase Change of Water under High Hydrostatic Pressure</i>
1999-2001	Middle East Technical University (METU), Ankara - Turkey Food Engineering Department, Master of Science <i>Optimization of Microwave Baked Bread Formulation</i>
1994-1999	METU, Ankara - Turkey Food Engineering Department, Bachelor of Science
1991-1994	Ankara High School, Ankara - Turkey

WORK EXPERIENCE

Jan 2002- today	Research Assistant, TUM Chair of Fluid Mechanics & Process Automation
Sept 2000-Jan 2002	Research Assistant, Food Engineering Department at METU
Jan-Aug 2000	Food Engineer, Erler Catering, Ankara – Turkey
Sept 1998	Student Apprentice, Pinar Meat, Yasar JSC, Izmir - Turkey
Sept 1997	Student Apprentice, Kavaklidere Winery , Ankara - Turkey

ADDITIONAL PUBLICATIONS, POSTERS AND PROCEEDINGS

- Özmanlı, Ö., Şümnü, G., Şahin, S. “Assesment of proofing of bread dough in the microwave oven” *Eur. Food Res. Technol. (Z. Lebensm. Unters. Forsch. A)*, **212**, 487-490 (2001).
- Özmanlı, Ö., Şümnü, G., Şahin, S. “Effects of different formulations on the quality of microwave baked bread” *Eur. Food Res. Technol. (Z. Lebensm. Unters. Forsch. A)*, **213**, 38-42 (2001).
- Şümnü, G., Özmanlı, Ö., Sahin, S. “Effects of microwave proofing on quality of microwave baked breads”, *Proceedings of 3rd International Conference on Predictive Modelling of Foods*, Leuven-Belgium, 301-302, 2000.
- Sahin, S., Özmanlı, Ö., Şümnü, G. “Optimization of microwave baking of bread”, Leuven-Belgium, *Proceedings of 3rd International Conference on Predictive Modelling of Foods*, 329-330, 2000.
- Özmanlı, Ö., Şümnü G., Şahin S., “Effects of microwave proofing with different gluten containing flours on quality of microwave baked breads”, *Institute of Food Technologists Annual Meeting Book of Abstracts*, New Orleans- Lousiana, pp. 127, 2001.